Collective Motion in Active Nematic Liquid Crystals



Rian Hughes

Oriel College
Rudolf Peierls Centre for Theoretical Physics
University of Oxford

This thesis is submitted for the degree of
Doctor of Philosophy
at the University of Oxford

Hilary Term 2021

Abstract

Active matter is based on understanding the physical mechanisms that give rise to large scale flows in aggregates of self-propelling particles. If the particles have a head-tail, or nematic, symmetry, then their structure resembles that of a passive nematic liquid crystal. However, unlike passive liquid crystals, the active injection of energy into the system by the particles' self-propulsive motion results in collective motion, which gives rise to a class of fluids known as active nematic fluids. Experimental examples of such fluids include cytoskeleton biopolymers, bacterial suspensions, and cell monolayers. The topic of this thesis is to understand the physical mechanisms that result in, and how to control the oftentimes turbulent, collective motion of active nematic fluids.

First, continuum simulations are used to investigate how confinement can tame the motion of an active nematic fluid in a closed channel, and then compared to results from experiments. By regulating the width of the channel, which screens the active flows, we find a novel flow state and recover a variety of flow states. The characteristic wavelength is found to be dependent on the channel width but independent of the activity.

Secondly, we examined how active nematic droplets can migrate towards a chemical source that regulates the activity. The active nematic droplet is found to direct flows towards its interface, which when coupled to the symmetry breaking in the chemical field, results in a net migration towards the chemical source. We find that while small and large droplets migrate with the same root-mean-square velocity, the larger droplets are more direct in their migratory motion.

Finally, we apply the theory of active nematics at the cellular level by modelling a cluster of distinct cells using a multi-phase field approach. We drive the motion within the cluster using nematic forces that orient towards the direction of least cell-cell contact, as motivated by contact-inhibition-of-locomotion. Cell clusters are found to display a rich variety of dynamics, ranging from jammed and fluid-like motion in confluence, to wound healing and migration in open space.

Acknowledgements

First and foremost, I would like to thank my supervisor, Prof. Julia Yeomans, not only for kindly welcoming me into her research group but also for providing valuable guidance throughout my DPhil. I thoroughly appreciate you giving me enough freedom to pursue my own research interests, while also providing structure when the need arose.

I would also like to thank all my colleagues who provided me with an endless series of encouragement and fruitful discourse. Kristian Thijssen, I appreciate all the engaging discussions we had throughout our DPhils. This gratitude also extends out to all my other colleagues, in particular, Amin Doostmohammadi, Romain Mueller, Luuk Metselaar, Jerome Hardouin, Guanming Zhang, Saeed Mahdisoltani, Tunrayo Adeleke-Larodo, Mehrana Raeisian Nejad, Liam Ruske, James Graham, Andrew Orr, Muriel van der Laan, and Saraswat Bhattacharyya.

Of course, my time in Oxford would not have been the same without the friends I made along the way. Guillaume Thekkedath and Hongmin Gao, the formals at Oriel College and the seemingly endless bike rides were some of the most memorable. To all my friends at LubISS, I have many fond memories of the time spent with you. I hope we organise another LubISS meeting as soon as possible.

Finally, this thesis would not have been possible without the support of my family. Mum and Dad, I'm thoroughly grateful for all the sacrifices you've made, and the opportunities you've given, to allow me to be where I am today. This thesis is dedicated to both of you. To Aisling and Meabh, who remind me of the important things in life. Sean and Ciaran, your mentorship has been invaluable to me, and I could not have asked for better brothers. I really owe both of you.

Publications

Authored Pulications contributing to this thesis:

- J. Hardoüin*, R. Hughes*, A. Doostmohammadi, J. Laurent, T. Lopez-Leon, J. M. Yeomans, J. Ignés-Mullol, and F. Sagués, "Reconfigurable flows and defect landscape of confined active nematics," Comm. Phys. 2 no. 1, (2019) 121.

- R. Hughes and J. M. Yeomans, "Collective chemotaxis of active nematic droplets," Phys. Rev. E 102 (2020) 020601.

- Rian Hughes and Julia M Yeomans "Collective Motion in Active Nematic Droplets" *In preparation*

* Denotes co-author

Contents

1 Introduction **1**

2 Passive Nematic Liquid Crystals **7**

2.1 Passive Nematic Liquid Crystals 7

2.2 The Nematic Order Parameter and **Q**-Tensor 8

2.3 Passive Nematic Free Energy 9

2.4 Toplogical Defects 12

2.5 Beris-Edwards Formulation 14

2.6 Navier-Stokes Equations 15

3 Active Nematic Liquid Crystals **17**

3.1 Active Stress 19

3.2 Hydrodynamic Instabilities in Active Nematic Liquid Crystals 20

3.3 Topological Defects in Active Nematic Liquid Crystals 22

3.4 Active Turbulence 25

3.5 Intrinsic Free Energy 26

3.6 Active Anchoring 27

3.7 Controlling Active Nematic Flows 29

4 Reconfigurable flows and defect landscape of confined active nematics **33**

4.1 Computational Setup 34

4.2 Experimental setup 36

4.3 Flow States 36

4.4 Defect-free shear flow disrupted by instabilities 40

4.5 The dancing state: a one-dimensional line of flow vortices 44

4.6 Conclusion 45

5 Collective Chemotaxis of Active Nematic Droplets **49**
5.1 Introduction 49
5.2 Model 50
5.3 Trajectories of Chemotactic Clusters 54
5.4 Results 55
5.5 Conclusion 58

6 Multi-Phase Field Model **61**
6.1 Eukaryotic cell dynamics 61
6.2 Models of collective cell motion 66
6.3 Multi-phase field model 67

7 Collective Motion in Active Nematic Droplets **73**
7.1 Model 74
7.2 Confluent monolayers 76
7.3 Free Clusters 78
7.4 Wound healing 80
7.5 Active force inhibition 81
7.6 Conclusion 83

8 Conclusion and outlook **85**
8.1 Summary of conclusions 85
8.2 Outlook 87

Appendices **89**

A Implementation of the Models **91**
A.1 The Lattice Boltzmann Method 91
A.2 Finite Difference Method 93

Bibliography **104**

List of Figures

1.1 Schematic of microtubule-kinesin motion 4

2.1 Thermotropic nematic liquid crystal bulk free energy and nematic instabilities 10
2.2 Schlieren textures 12
2.3 Schematic of topological defects. 13

3.1 Examples of biological active nematic fluids. 18
3.2 Active nematic rod self-propulsion 20
3.3 Hydrodynamic instabilities of active nematic liquid crystals 21
3.4 Flow field around active nematic topological defects 23
3.5 Schematic of topological defect creation and annhilation 24
3.6 Snapshot of active turbulence 26
3.7 Mechanisms to control active nematic fluids. 30

4.1 Experimental setup of microtubule-kinesin suspension 37
4.2 Snapshots of the director field in a confined active nematic, for both simulations and experiments 38
4.3 Ratio of the active length scale and channel width as a function of the channel width 39
4.4 Flow patterns in simulations and experiments of an active nematic fluid confined to a channel 42
4.5 Kymograph of shear-instability state 43
4.6 Defect-defect spacing as a function of channel width 43
4.7 Defect nucleation at the channel walls 46

5.1 Snapshots of active nematic droplet migrating towards a chemical source 53
5.2 Trajectories of active nematic droplets undergoing collective chemotaxis . 54

5.3 Active anchoring in an active nematic droplet undergoing colletive chemotaxis . . . 56
5.4 Root-mean-square velocity and chemotactic index as a function of activity and droplet size . . . 57

6.1 Lamellipodium and schematic of cell treadmilling . . . 62
6.2 Schematic of contact-inhibition-of-locomotion, and measurements of traction forces, in cell monolayers . . . 63
6.3 Physical models of cell monolayers . . . 65
6.4 Schematic and results from multi-phase field model . . . 71

7.1 Snapshot of the active forces, measurement of the average elongation, rearrangement rate, velocity distribution and velocity-elongation direction of motion in active nematic droplet monolayers . . . 77
7.2 Morphological structures, the radius of gyration, force bias, and a snapshot of active forces along the interface of active nematic droplets . . . 79
7.3 Wound healing in active nematic droplet clusters . . . 80
7.4 Morphological structures as a function of activity and active force weighting in contractile active nematic droplet clusters . . . 82
7.5 Radius of gyration, wound healing, and rearrangement rate as a function of activity for different values of active force weighting. . . . 83

A.1 Schematic of a D2Q9 latice grid and the Lattice-Boltzmann streaming step 93

Chapter 1

Introduction

Understanding the motion of matter has been of particular interest to people around the world for generations, whether it be the trajectory of stars or apples falling from trees. Historically, physicists have made a lot of progress in understanding the motion of inanimate matter, but predicting the motion of animate matter has remained much more elusive. However, one simply needs to observe a flock of birds, or a swarm of fish, to grasp that their collective motion has an element of predictability. This is particularly remarkable considering the constituent components can seemingly have a will of their own. From the eye of a physicist however, flocks of birds and swarms of bacteria simply look like a collection of self-propelling particles (SPPs). The aim of active matter, a subfield of soft condensed matter physics, is to uncover the universal physical mechanisms that underlie the collective motion of large collections of self-propelling particles.

The Viscek model [1, 2] is one the earliest and most seminal works in the field of active matter. It is a particle-based model that captures the flocking motion of a cluster of SPPs, where each particle moves in the direction of a pre-defined vector known as the polarisation. The polarisation angle of a given particle is taken to be the average of all polarisation angles within some fixed distance of the particle. Some noise is also added to the polarisation angle to make the process stochastic. At low densities, the particle motion is noisy and chaotic, while at higher densities the particles flock together. The Viscek model was later used by Toner and Tu to create a continuum level theory of a collection of polar SPPs [3–5], which gave rise to the study of active fluids.

Inertia dominates at the macroscopic level of the Toner and Tu model, and so this model is not suited to describe the motion of microscopic organisms, where viscous forces dominate. Despite living at low Reynolds number, large collections of microscopic organisms can exert enough force on their environment to generate large scale flows. A seminal paper by Simha and Ramaswamy [6] made significant progress in creating a hydrodynamic theory to describe such flows. Their approach is to model a collection of particles that exert either polar forces, meaning they exert a single force in the direction

$\mathbf{p}$, or apolar forces, meaning they exert forces with equal magnitude in the directions $\mathbf{p}$ and $-\mathbf{p}$. This head-tail symmetry of the apolar particles is also known as a nematic symmetry. Coarse-graining the particle forces allows one to define a stress tensor known as the active stress. This stress term has a nematic symmetry at first order, and the class of fluids that exhibit active stresses are known as active nematic fluids. The work presented in this thesis is focused on understanding the dynamics of biological fluids using the hydrodynamic theory of active nematic fluids.

Collections of passive nematic particles that can flow like a fluid, yet have long-range order in their nematic orientation are known as passive nematic liquid crystals. A useful way to think about active nematic fluids is that they are passive nematic liquid crystals, except the constituent particles inject energy into the system. Thus one can use the tools of passive liquid crystal theory to understand the dynamics of active nematic fluids. Two particularly useful concepts from passive nematic liquid crystal theory are the director field, which describes the average orientation of the particles at each point in space, and the nematic order parameter, which describes how well aligned the particles are on average at each point in space. If the orientation of the particles is isotropic, then the nematic order parameter goes to zero and the liquid crystal is said to be in an isotropic state. However, if the particles are well aligned then the nematic order parameter is non-zero and the system is said to be in a nematic state.

The flows generated by the active stress result in hydrodynamic instabilities of the director field. This is because gradients in the director field will generate a flow via the active stress. These flows reorient and generate further gradients in the director field. This process can give rise to turbulent-like flows, exhibiting jets and vortices. This state is known as active turbulence. It is distinct from inertial turbulence because it exists at low Reynolds number. The flow field of bacterial suspensions [7, 8, 12] and cell monolayers [9–11] exhibit jets and vortices resembling that of active turbulence.

A key characteristic of active turbulence is the existence of point-like regions, known as topological defects, where the director field becomes ill-defined, and the nematic order parameter goes to zero. An important aspect of these defects is that they have a topological charge associated with them, which is simply the winding number of the director field around them. The topological charge of a nematic fluid is conserved, and takes on values equal to half-integer multiples, thanks to the nematic symmetry of the particles. Defects in active nematic liquid crystals are created from the nematic instabilities generated by the active stress. A defect can be destroyed by combining it

with a defect of the same magnitude but opposite charge.

Remarkably, topological defects have not only been found in biological systems but also appear to play important roles in their dynamics. For example, in cell monolayers, defects are sites of cell apoptosis and extrusion [10], they influence the structure of surfaces in bacterial monolayers [12], and are sites of layer formation in bacterial colonies [13]. One particularly fascinating example relates to the morphology of small freshwater organisms known as Hydra [14, 15]. The long axis of these rod-like creatures is determined by topological defects, which are formed in the supracellular actin fibres of its ectoderm (its 'skin').

Topological defects are also important for the theoretical study of active nematic fluids since their mean separation defines the characteristic lengthscale of the system, known as the active lengthscale. If the particles inject more energy into the system, flows become more chaotic, resulting in more nematic instabilities, which in turn generate more topological defects. This results in a decrease in the mean distance between defects, and so the active lengthscale. Conversely, increasing the energetic cost of deformations results in the instabilities spreading out, and so an increase in the distance between deformations, and so the active lengthscale. The active lengthscale is proportional to the (square root) of the elastic energy coefficient and the active stress coefficient.

Remarkably, certain experimental setups are able to precisely vary both the energy injection of the particles and the energetic cost of elastic deformations. Experimental setups that have played an important role in the study of active nematic fluids are suspensions of cytoskeleton protein filaments and their associated molecular motors. Two popular choices of filament-motor suspensions are actin-myosin [16, 17] and microtubule-kinesin [18, 19, 122] suspensions. The molecular motors connect to two filaments and cause them to shear past one another, as depicted in Fig. 1.1. This motion generates significant flows at the continuum level which results in the formation of vortices and jets, resembling those of active turbulence. Moreover, a clear population of topological defects can be observed in these suspensions. These active fluids have nice properties that make them desirable to compare against theoretical models. For example, the strength of the active stress can be regulated by controlling the concentration of Adenosine triphosphate (ATP) [19], and the elastic energy can be increased by increasing the concentration of filaments [17]. This allows the experimentalist to vary the active lengthscale in the suspension.

The active lengthscale is not the only length scale of interest in experiments however,

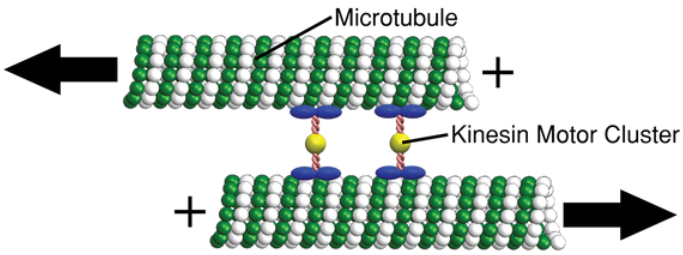


Figure 1.1: Schematic of molecular motors (kinesin) shearing a pair of microtubules past each other, in the direction of their positive (barbed) end. Image taken from Stephen J. Decamps personal website.

if the suspensions are bounded the confinement length scale can also influence the dynamics. For example, in simulations, reducing the active lengthscale from above the confinement lengthscale to the confinement lengthscale results in the system moving from a state of active turbulence to a dancing-disclination state [20], characterised by two populations of defects moving past one another in sinusoidal patterns. In chapter 4 we show that the confinement length scale is the characteristic length scale of bounded systems, which is markedly different than unconfined systems which are governed by the active length scale. We also find that the active fluid enters a range of distinct states as the confinement length scale is varied.

A physical theory attempting to describe the motion of biological systems should account for any biological mechanisms unique to the system of interest. One crucial mechanism that cells use to navigate their environment is known as chemotaxis. This is the ability for cells to migrate along a chemical gradient and plays vital roles in embryogenesis and cancer metastasis. The biological importance of this mechanism is reflected in its existence across multiple taxonomic genera, including Prokaryotic [21] and Eukaryotic [22–26] organisms. Surprisingly, large collections of cells can migrate along chemical gradients even when individual cells migrate in the opposite direction [22], or do not undergo chemotaxis at all [27]. This suggests that single-cell chemotaxis is distinct from what has been termed collective chemotaxis. Understanding how collective chemotaxis can arise within an active nematic framework forms the basis of the work discussed in Chapter 5.

The hydrodynamic theory of active nematic liquid crystals has been successful in describing the continuum level flows of filament-motor protein suspensions, colonies of bacteria, and cell monolayers. However, this theory coarse-grains away a lot of physical

details at the cellular level, for example, cell-cell adhesion and repulsion in cell monolayers. The strength of modelling these systems at the cellular level is that they can explicitly include intercellular interactions. For example, a multi-phase field approach uses a collection of distinct phases to model a cell cluster, where each phase represents a unique cell. One can then place interactions between the phases, such as adhesion and repulsion, to investigate the importance of their role in a range of dynamics. The motion of the individual cells and the entire cluster is usually driven by placing a polarisation force on the cells [28, 120], although recent work [29, 30] has started to investigate the dynamics when nematic forces are included. The work discussed in Chapter 7 investigates how active nematic forces can give rise to large scale morphological changes in a cluster of active nematic droplets.

This thesis is outlined as follows. Chapters 2 and 3 provide the relevant background material needed to understand passive and active nematic liquid crystals, respectively. Chapter 4 presents the work done on understanding how confinement influences the collective flows and characteristic length scale of an active nematic fluid. Chapter 5 examines modelling collective chemotaxis within an active nematic framework. Chapter 6 explains the multi-phase field model, and certain biological mechanisms used to motivate model choices used in this thesis. Chapter 7 discusses how large scale morphological changes in a cell cluster can arise from within an active nematic multi-phase field model. Chapter 8 closes the thesis with a summary of the result and provides directions for future research. Details on models that were solved numerically are given in appendix A.

Chapter 2

Passive Nematic Liquid Crystals

Passive liquid crystal theory plays an important role in the hydrodynamic theory of active nematic liquid crystals. This is because to first order, the stress generated by the self-propelling particles has a head-tail, or nematic, symmetry. This gives rise to a nematic field, whose dynamics can be accounted for via the Beris-Edwards equation. The flow field is described by the Navier-Stokes equations, with additional stresses to account for the nematic properties of the particles. In this section, we introduce the properties of passive and active liquid crystals, along with their equations of motion.

2.1 Passive Nematic Liquid Crystals

Liquid crystals are phases of matter which can exhibit long-range orientational order but can also move like a liquid. There are many different classes of liquid crystals each characterised by their inherent physical symmetries, but the type of interest here are nematic liquid crystals, and are typically collections of rod-like particles.

Nematic particles can be well aligned on average, in which case they are said to be in a nematic state. If they are not well-aligned then they are said to be in an isotropic state. The ordering is described by a nematic order parameter S, which ranges from $S = 1$ for a perfectly aligned nematic state, to $S = 0$ for an isotropic state.

The orientation of the nematic field described using a two-tensor $\mathbf{Q}$, given by

$$\mathbf{Q} = \frac{3}{2} S(\mathbf{nn} - \frac{1}{3}).$$

The vector field $\mathbf{n}$ defines the orientation of the nematic field. Note that $\mathbf{Q}$ is symmetric under the transformation $\mathbf{n} \to -\mathbf{n}$ as required by the nematic symmetry of the particles. This $\mathbf{Q}$ tensor completely defines the nematic field at a given time.

2.2 The Nematic Order Parameter and Q-Tensor

To derive the **Q**-tensor, first let $\mathbf{m}$ be the unit vector that defines the orientation of a given nematic particle, and $f(\mathbf{m})$ be the distribution of an ensemble of such particle orientations. The moments of this distribution function indicate both the orientation and how well aligned the particles are on average. The first moment of f is zero due to the nematic symmetry of the particles. The first non-zero moment of f is given by the second-rank tensor $\mathcal{M} = \int_{\mathbb{S}^2} f(\mathbf{m})\mathbf{m} \otimes \mathbf{m} \mathrm{d}\Omega$, which has components

$$\mathbf{M}_{\alpha\beta} = \int_{\mathbb{S}^2} f(\mathbf{m}) m_\alpha m_\beta \mathrm{d}\Omega \tag{2.1}$$

where $\mathrm{d}\Omega$ is a solid angle, and the integral is over the two-sphere $\mathbb{S}^2$ surrounding the particle ensemble. The **Q**-tensor is defined as the traceless part of **M**, and in three-dimensions is given by

$$\mathbf{Q} = \mathbf{M} - \frac{1}{3}\mathbf{I}. \tag{2.2}$$

It will become clear why working with the traceless version of **M** is preferable later when we discuss the nematic order parameter S.

The **Q**-tensor can be simplified by working with its diagonalised form, which is given by the sum of its eigenvalues λ_i times the tensor product of its eigenvectors $\mathbf{n}_i$,

$$\mathbf{Q} = \lambda_1 \mathbf{n}_1 \otimes \mathbf{n}_1 + \lambda_2 \mathbf{n}_2 \otimes \mathbf{n}_2 + \lambda_3 \mathbf{n}_3 \otimes \mathbf{n}_3. \tag{2.3}$$

where $\mathbf{n}_i$ are in the standard basis. Given that nematic particles are uniaxial (i.e. they are extended in one direction and have equal width in the two perpendicular directions), we require $\lambda_1 = \lambda_2$. Combining this with the tracelessness of **Q** gives $\lambda_3 = -2\lambda_1$. This property can then be used with $\mathbf{n}_1 \otimes \mathbf{n}_1 + \mathbf{n}_2 \otimes \mathbf{n}_2 + \mathbf{n}_3 \otimes \mathbf{n}_3 = \mathbf{I}$ to write

$$\mathbf{Q} = S(\mathbf{n} \otimes \mathbf{n} - \frac{1}{3}\mathbf{I}) \tag{2.4}$$

where $\mathbf{n} = \mathbf{n}_3$ and $S = \frac{3}{2}\lambda_3$. Note that $\mathbf{n}_3$ is the elongation axis of the nematic particles and so $\mathbf{n}$ describes the orientation of the nematic field.

To see how the coefficient S corresponds to how well aligned the particles are, take the dot product of $\mathbf{n}$ on both sides of **Q** in eqn. 2.2 and eqn. 2.4, and combine to get

$$S = \frac{3}{2}[\langle(\mathbf{m} \cdot \mathbf{n})^2\rangle - \frac{1}{3}]. \tag{2.5}$$

where the average is defined as $\langle(\mathbf{m}\cdot\mathbf{n})^2\rangle = \int f(\mathbf{m})(\mathbf{m}\cdot\mathbf{n})^2 \mathrm{dA}$. For simplicity assume that the particles are aligned such that $\mathbf{n} = (0, 0, 1)$. Then write $\mathbf{m}$ in terms of its polar angles (θ, ϕ), so that $\mathbf{m} = (\sin(\theta)\cos(\phi), \sin(\theta)\sin(\phi), \cos(\theta))$. This allows one to write $\langle(\mathbf{m}\cdot\mathbf{n})^2\rangle = \langle\cos^2(\theta)\rangle$, which can be substituted into eqn 2.5 to give

$$S = \frac{3}{2}\langle\cos^2(\theta) - \frac{1}{3}\rangle = \frac{3}{2}\int f(\theta)(\cos^2(\theta) - \frac{1}{3})\mathrm{d}\Omega. \tag{2.6}$$

To get an intuitive feel for how this operates as a nematic order parameter, suppose that the distribution was sharply peaked around $\theta = \pi$ (equivalently $\theta = 0$). In this case, $S = 1$ corresponds to the perfectly aligned nematic state. Now suppose that the particles are orientated isotropically on average so that the distribution is uniform. Then $S = 0$ which corresponds to the isotropic state. This summarises how S acts as an order parameter that characterises how well aligned the particles are.

At a given time the $\mathbf{Q}$-tensor completely characterises the nematic field of the particles. The nematic orientation of the particles is determined by $\mathbf{n}$ while the degree of alignment is given by S. The evolution of the nematic field is governed by the free energy, which is discussed in more detail in the next section.

2.3 Passive Nematic Free Energy

A nematic liquid crystal will tend towards the equilibrium state which minimises its free energy. For example, the equilibrium state of a thermotropic nematic liquid crystal above its critical temperature is an isotropic state, and a nematic state below the critical temperature. Lyotropic nematic liquid crystals are defined by the concentration dependence of their nematic order S. At high concentrations, they exist in a nematic state, while at low concentrations they are in an isotropic state. Deformations in the nematic field are also energetically costly, and so an equilibrium state will have as few gradients in the nematic field as possible. The details of this free energy form the basis of this and the next section.

The equilibrium state at the coarse-grained level is governed by a free energy which is constructed using Ginzburg-Landau theory [31]. This phenomenological approach involves expanding the free energy in terms of $\mathbf{Q}$. This expansion involves terms which are functions of $\mathbf{Q}$, grouped together into the bulk-free energy $\mathcal{F}_{bulk}$, and functions of

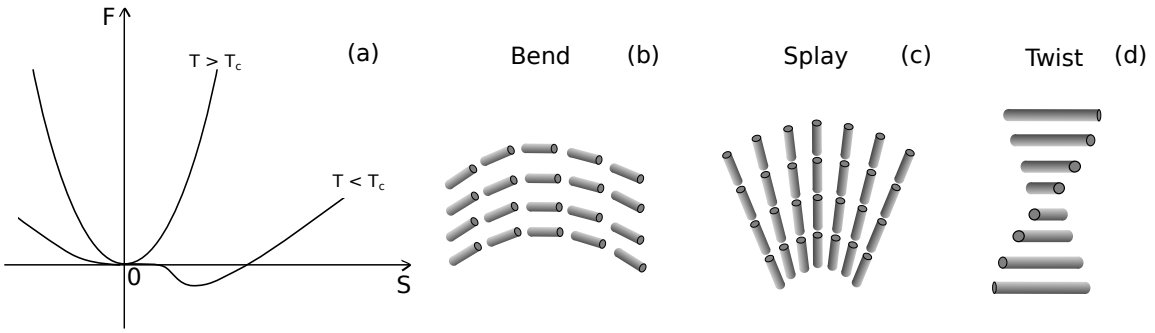


Figure 2.1: (a) Schematic of the bulk free energy $\mathcal{F}_{bulk}$ as a function of nematic order parameter S, for temperatures T above and below the critical temperature T_C. (b) - (d) Schematic of a bend, splay, and twist instability respectively.

gradients in $\mathbf{Q}$, grouped together into the gradient, or elastic, free energy $\mathcal{F}_{grad}$. This defines the total (Landau-de Gennes) free energy as $\mathcal{F} = \mathcal{F}_{bulk} + \mathcal{F}_{grad}$. Since we will keep only the first few terms in the expansion, this approach is only valid for small values of S. The isotropic-nematic transition is only weakly first-order [32], although this approach works surprisingly well in the nematic phase [33].

The bulk free energy $\mathcal{F}_{bulk}$ is given by an expansion of scalar function $g(\mathbf{Q})$. However, because we require these functions to be invariant under rotations of $\mathbf{Q}$, and $\mathbf{Q}$ is traceless, then g must be a function of $tr(\mathbf{Q}^k)$, for k greater than or equal to two. Further using the Cayley-Hamilton theorem one can show that $tr(\mathbf{Q}^k)$ is given by some polynomial function of $tr(\mathbf{Q}^2)$ and $tr(\mathbf{Q}^3)$. The bulk free energy can then be written as [31]

$$\mathcal{F}_{bulk} = \frac{1}{2}A(Q_{\alpha,\beta}Q_{\alpha,\beta}) - \frac{1}{3}B(Q_{\alpha,\beta}Q_{\beta,\gamma}Q_{\gamma,\alpha}) + \frac{1}{4}C(Q_{\alpha,\beta}Q_{\alpha,\beta})^2 + \mathcal{O}(\mathbf{Q}^5). \tag{2.7}$$

Note that the zeroth-order constant term is neglected since it simply amounts to a shift in the free energy. The first-order term is zero since $\mathbf{Q}$ is traceless, and the fourth-order term is necessary so that the magnitude of $\mathbf{Q}$ does not increase uncontrollably, which also requires C to be positive. It is worth noting that in two dimensions, the third-order term vanishes due to symmetry [31], in which case the isotropic-nematic transition is continuous [34]. One is free to include higher-order terms, although the goal is to capture the main features of interest using a theory that is as simple as possible.

For example, thermotropic nematic liquid crystals are defined by their temperature dependence. Above some critical temperature T_C the system exists in an isotropic state

(i.e. $S = 0$), whereas below this temperature a nematic state ($S \neq 0$) persists. This requires the free energy to be temperature-dependent, which is incorporated into the model by making the coefficients functions of temperature. A simple approach is to make $A = A_0(T - T_C)$ and both B and C constants [31]. It is then possible to see that the free energy changes such that above T_C the global minimum is centred at $S = 0$, and below T_C the minimum shifts such that the system becomes unstable to nematic ordering. This is depicted in Fig. 2.1 (a).

The gradient / elastic free energy incorporates the energy penalty due to deformations in the orientation of $\mathbf{n}$ across space. In three-dimensions, the elastic deformations can take the form of bend, splay, and twist deformations as shown in Fig 2.1 (b)-(d) respectively [31]. It is worth noting that the twist deformation requires three dimensions to form. In three-dimensions, the elastic deformations are described by the Frank elastic free energy

$$\mathcal{F}_{Frank} = \frac{K_{Splay}}{2}(\nabla \cdot \mathbf{n})^2 + \frac{K_{Twist}}{2}[\mathbf{n} \cdot (\nabla \times \mathbf{n})]^2 + \frac{K_{Bend}}{2}[\mathbf{n} \times (\nabla \times \mathbf{n})]^2 \tag{2.8}$$

where the coefficients K_{Splay}, K_{Twist} and K_{Bend} are known as the splay, twist and bend Frank elastic constants [31]. It is also possible to derive a Landau-de Gennes elastic free energy $\mathcal{F}_{grad-LdG}$ using functions of $\nabla\mathbf{Q}$ and $\mathbf{Q}$,

$$\mathcal{F}_{grad-LdG} = \frac{L_1}{2}(\partial_k Q_{ij})(\partial_k Q_{ij}) + \frac{L_2}{2}(\partial_j Q_{ij})(\partial_k Q_{ik}) + \frac{L_3}{2}Q_{ij}(\partial_i Q_{kl})(\partial_j Q_{kl}). \tag{2.9}$$

The Frank elastic free energy constants can be mapped to the Landau-de Gennes elastic free energy constants by [35]

$$\begin{aligned} L_1 &= \frac{1}{9S^2}(-K_{Splay} + 2K_{Twist} + K_{Bend}), \\ L_2 &= \frac{4}{9S^2}(K_{Splay} - K_{Twist}), \\ L_3 &= \frac{2}{9S^3}(-K_{Splay} + K_{Bend}). \end{aligned}$$

In practice [36] the "one-elastic-constant" is used, whereby $K_{Splay} = K_{Twist} = K_{Bend}$, which results in $L_2 = L_3 = 0$, meaning the free energy due to elastic deformations is captured by a single term

$$\mathcal{F}_{\nabla Q} = K(\nabla\mathbf{Q})^2, \tag{2.10}$$

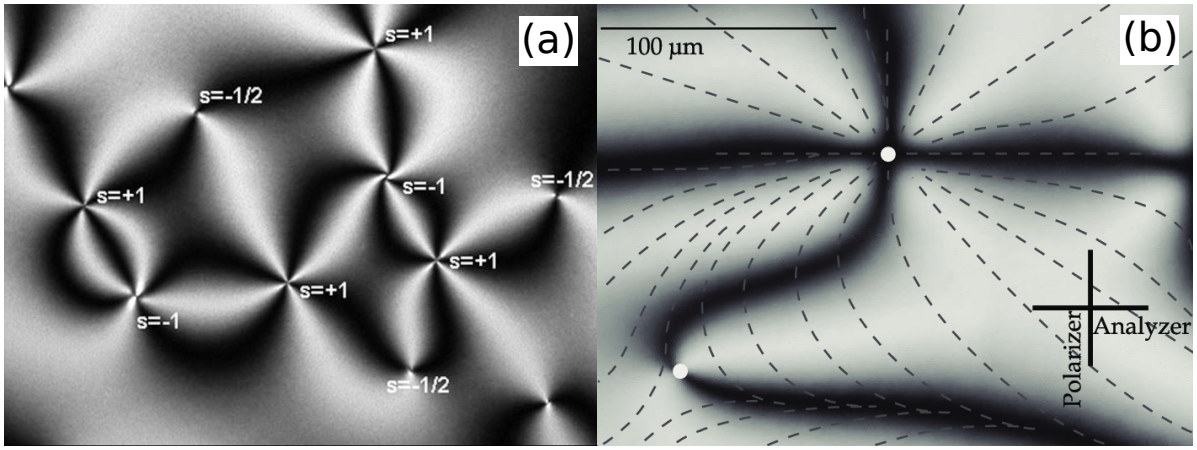


Figure 2.2: (a) Schlieren texture with topological defect charge. Image taken from Bohdan Senyuk's personal website. (b) Schlieren texture with nematic field overlayed [38].

where $K = \frac{L_1}{2}$.

It is also useful to be able to fix the orientation of a nematic field in a given region, for example along a boundary. This can be done by using the anchoring free energy $\mathcal{F}_{anchoring}$,

$$\mathcal{F}_{anchoring} = \frac{1}{2}\mathcal{W}Tr(\mathbf{Q} - \mathbf{Q}_D)^2 \tag{2.11}$$

where $\mathbf{Q}_D$ is the specific $\mathbf{Q}$-tensor we want the system to relax to [37]. The anchoring is described as planar if the nematic field is made to align parallel to a surface, and homeotropic if it is made to align perpendicular to the surface.

2.4 Toplogical Defects

Passive nematic liquid crystals can exhibit localised regions where the nematic field has no well-defined orientation. These regions can be observed by passing polarised light through a nematic liquid crystal wedged between two crossed polarizers. The light which passes through the polarizers will either be blocked or transmitted depending on the orientation of the nematic field. This process gives rise to beautiful patterns known as Schlieren textures, as shown in Fig 2.2 (a). From these patterns, one can deduce the nematic field orientation, an example of which is given in Fig 2.2 (b). The dark regions in the textures are called brushes. The regions where multiple brushes meet mark locations where the nematic field orientation becomes ill-defined. These regions

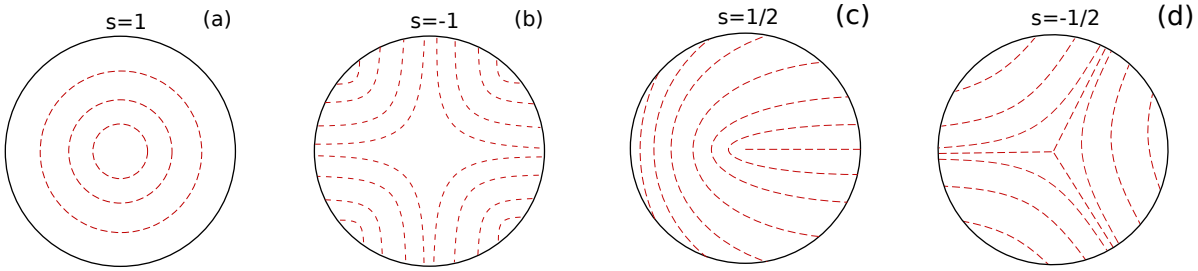


Figure 2.3: Nematic field with topological defects of charge (a) s=1, (b) s=-1, (c) s=1/2, and (d) s=-1/2.

are of particular interest in both passive and active nematic liquid crystals and are called topological defects. They are the only regions in which the nematic field becomes ill-defined in two-dimensions, and since this thesis deals with two-dimensional active liquid crystals, the discussion on topological defects will be restricted to two-dimensions.

The charge of a topological defect is defined as the winding number around a closed loop surrounding the defect. This is calculated as

$$s = \frac{1}{2\pi} \oint_C \mathrm{d}\theta \tag{2.12}$$

where C is a closed-loop surrounding the defect location, and θ is the angle of the director field $\mathbf{n}$ along C. The winding number s measures the number of rotations that the director field goes through when following the closed loop around the defect. Since the nematic field has a head-tail symmetry, half-integer winding numbers are possible. The sign of the winding number simply indicates the direction of rotation, for example, positive values mean θ rotates clockwise, while negative values mean it rotates anti-clockwise when following the closed path C. A schematic of both half-integer and full integer defects is given in Fig. 2.3. These defects can also be seen in the Schlieren textures of Fig. 2.2 where half-integer defects are located where two brushes (dark regions) meet, while full integer defects are located where four brushes meet.

It should also be noted that defects of topological charge greater than $\pm\frac{1}{2}$ are rarely seen since the energetic cost of a defect increases with the magnitude of its topological charge. As a result, ± 1 defects will decompose into two $\pm\frac{1}{2}$ defects, which then move apart due to elastic forces. However, if one could force two defects together, a new defect would be created with a topological charge equal to the sum of the two constituent defects. Bringing together a $+\frac{1}{2}$ and $-\frac{1}{2}$ defect pair results in annihilation, and a (locally) deformation free defect field. Conversely, it is possible to create a $+\frac{1}{2}$ and $-\frac{1}{2}$ defect

pair from a defect-free nematic field. In two dimensions, defects must be created in pairs since the topological charge of a system is conserved [31].

The Frank elastic free energy at the location of topological defects will tend towards infinity due to the gradients in $\mathbf{n}$. This can be remedied by noting that the defect core is not nematic, but isotropic, meaning that S (and therefore $\mathbf{Q}$) tends to zero. Using the tensorial description of the elastic free energy $\mathcal{F}_{elastic}$ in eqn. 2.9 allows one to incorporate this and so to remedy the issue.

2.5 Beris-Edwards Formulation

Now we consider the time evolution dynamics of the nematic field. Early work on determining the partial differential equation governing the dynamics of the nematic field was performed by Ericksen, Leslie and Parodi [39–43]. Their approach had a particular focus on coupling the director field $\mathbf{n}$ to the $\mathbf{u}$. While influential, the downside of this work is that it assumes the nematic order parameter S is constant and so can not account for topological defects. Subsequently, Beris, Edwards and Gremla [44, 45] developed a theory to describe the nematic field in terms of the $\mathbf{Q}$-tensor, that allows one to account for changes in S. This thesis uses the Beris, Edwards and Gremla formulation and this section discusses the equation of motion for the $\mathbf{Q}$-tensor.

In the Beris-Edwards formulation, the $\mathbf{Q}$-tensor evolves according to

$$(\partial_t + u_k\partial_k)Q_{ij} = S_{ij} + \Gamma_Q H_{ij} \tag{2.13}$$

where Γ_Q is the rotational diffusivity constant for the molecular field $\mathbf{H}$.

The molecular field $\mathbf{H}$ causes the nematic field to relax to its equilibrium state, on a timescale given by Γ_Q^{-1}, and is given by

$$H_{ij} = -\frac{\delta\mathcal{F}}{\delta Q_{ij}} + \frac{1}{2}\frac{\delta\mathcal{F}}{\delta Q_{kk}}\delta_{ij} \tag{2.14}$$

where tracelessness results from the inclusion of the second term.

The co-rotational term $\mathbf{S}$ accounts for how the nematic order tensor $\mathbf{Q}$ responds to gradients in the flow. It is given by

$$S_{ij} = \xi E_{ij} - (\Omega_{ik}Q_{kj} - Q_{ik}\Omega_{kj}) \tag{2.15}$$

where $E_{ij} = \frac{1}{2}(\partial_i u_j + \partial_j u_i)$ and $\Omega_{ij} = \frac{1}{2}(\partial_i u_j - \partial_j u_i)$. The tumbling parameter ξ [46] plays a particularly important role in active nematics, which are discussed in chapter 3. It indicates whether the nematic particles will align to, or continuously reorient in, a shear flow. In the Ericksen-Leslie-Parodi framework it is given by $\hat{\xi} = \frac{3S}{S+2}\xi$ in 2D [47]. Above the threshold $|\hat{\xi}| > 1$ the nematic particles are in the flow-aligning regime, whereby particles align at an angle to the flow. The particular angle at which the nematic particles align with the flow is knwon as the Leslie-angle θ_L, which can be determined through the relation $\hat{\xi} = 1/\sin(2\theta_L)$. Below the threshold $|\hat{\xi}| < 1$ the particles are in the flow-tumbling regime, whereby particles continuously rotate in the flow.

2.6 Navier-Stokes Equations

The flow field $\mathbf{u}$ evolves according to the Navier-Stokes equations, given by

$$(\partial_t + u \cdot \nabla)\rho = 0 \tag{2.16}$$

$$\rho(\partial_t u_i + (u \cdot \nabla)u_i) = -\partial_i P + \partial_j \Sigma_{ij} \tag{2.17}$$

where ρ is the density, P is the pressure, and the stress components Σ_{ij} are given by

$$\Sigma_{ij} = 2\eta E_{ij} - P\delta_{ij} - 2\xi H_{ij} + Q_{ik}H_{kj} - H_{ik}Q_{kj} - \partial_i Q_{kl}\frac{\delta \mathcal{F}}{\delta(\partial_j Q_{kl})} \tag{2.18}$$

where η is the viscosity [47].

Equations 2.16 and 2.17 conserve mass and momentum in the fluid respectively. The stress terms in eqn. 2.18 incorporate how the nematic field generates and alters the flows. The first two terms describe the isotropic viscous stress and pressure respectively. The elastic stress is given by the $-2\eta H_{ij} + Q_{ik}H_{kj} - H_{ik}Q_{kj}$ term, and accounts for the fluid stresses that arise due to any movement of the liquid crystal. The contribution from the $\partial_i Q_{kl}\frac{\delta \mathcal{F}}{\delta(\partial_j Q_{kl})}$ term accounts for how the fluid should respond due to gradients in $\mathbf{Q}$.

Chapter 3

Active Nematic Liquid Crystals

Active liquid crystals consist of particles that exert forces on their environment, which in turn generate flows responsible for a vast range of fascinating dynamics. One important property, and indicator, of active nematic dynamics, is the existence of topological defects which are continuously generated and annihilated. Some examples which are modelled as active nematics include exoskeleton biopolymers, bacterial colonies and cell monolayers. A snapshot of a suspension of microtubules and molecular motors (kinesin) is shown in Fig. 3.1 (a), with a clear population of defects. The confinement in this particular system is of particular interest as it forms an important part of the work discussed in Chapter 4. Dense colonies of *serratia marcescens* bacteria also exhibit such defects, as shown in Fig. 3.1 (b)-(d). These are rod-shaped bacteria that use flagella to swim. Impressively, both the flow field and the nematic orientation field of these bacterial clusters can be determined across time, allowing for comparisons between experiments and theory. Another interesting experimental system that exhibits contractile active nematic properties are dense monolayers of mouse fibroblast cells. A plus and minus half defect can be seen in Fig. 3.1 (e) and (f) respectively. At the coarse-grained level the forces that the particles generate give rise to a stress term called the active stress. The theory of active nematic liquid crystals builds on its passive counterpart by including this active stress into the Navier-Stokes equations.

In this chapter, a derivation of the active stress that distinguishes active and passive nematic liquid theory is given. How this active stress gives rise to nematic instabilities, and in particular how it results in the continuous generation and annihilation of topological defects is discussed, along with the dynamics and interactions of defects. Finally, the chapter is closed with a discussion of the intrinsic free energy, active anchoring, and some different methods one can use to control active nematic fluids.

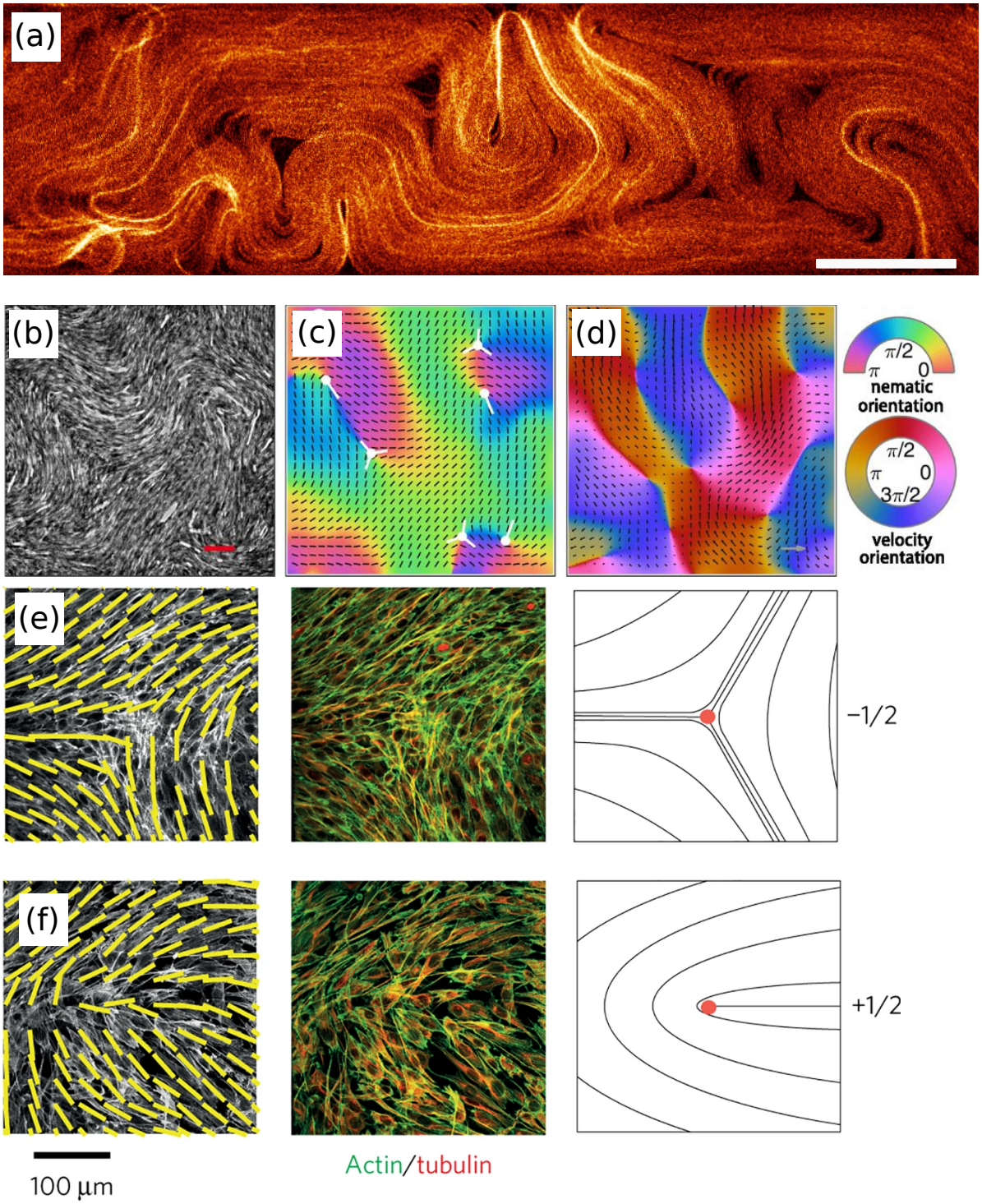


Figure 3.1: (a) Snaphot of a microtuble-kinesin suspension with scale bar = 100μm [48]. (b) A snapshot of a monolayer of *serratia marcescens* bacteria with scale bar = 30μm, with the corresponding nematic and velocity fields given in (c) and (d) respectively [8]. (e)-(f) Example of the $-\frac{1}{2}$ and $+\frac{1}{2}$ topological defects that arise in the nematic field of a mouse fibroblast cell monolayer [9].

3.1 Active Stress

The distinction between passive and active nematohydrodynamics arises from the self-propulsion of the constituent particles, and therefore the active stress drives a lot of the interesting dynamics of active nematics. The derivation of this stress was originally outlined by Simha and Ramsay in 2002 [6], and is summarised here.

A collection of rod-shaped active nematic particles, labeled by the index α, are located at positions $\mathbf{r}_\alpha(t)$, and have an axis given by $\mathbf{m}_\alpha(t)$ at a given time t. The rods ends are positioned at $\mathbf{r}_\alpha + a\mathbf{m}_\alpha$ and $\mathbf{r}_\alpha - a^{'}\mathbf{m}_\alpha$. A schematic of this system is given in Fig. 3.2 (a), which shows a rod shaped particle with center of mass indicated by the black circle, located a distance a and $a^{'}$ from the two ends respectively. The rods exert forces of strength f in equal and opposite directions. This amounts to an individual rod exerting a force f along $\mathbf{r}_\alpha + a\mathbf{m}_\alpha$, and $\mathbf{r}_\alpha - a^{'}\mathbf{m}_\alpha$. Note that if $a = a^{'}$, then the stokeslet flow at the center of the rod is zero and so individual particles become apolar. However, if $a \neq a^{'}$ then the flows around the center-of-mass are asymmetric and the particle becomes polar.

Summing the force dipoles of each rod results in a force-density

$$-\nabla \cdot \sigma^{act} = f \sum_\alpha \mathbf{m}_\alpha(t)\{\delta([\mathbf{r} - \mathbf{r}_\alpha - a\mathbf{m}_\alpha(t)]) - \delta([\mathbf{r} - \mathbf{r}_\alpha + a^{'}\mathbf{m}_\alpha(t)])\}. \tag{3.1}$$

Expanding the delta functions about $\mathbf{r} - \mathbf{r}_\alpha$ gives

$$\nabla \cdot \sigma_i^{act} = \frac{a + a^{'}}{2} f \nabla_j \sum_\alpha m_{\alpha,i} m_{\alpha,j} \delta(\mathbf{r} - \mathbf{r}_\alpha) + \mathcal{O}(\nabla^2). \tag{3.2}$$

This then leads to the definition of the active stress

$$\sigma_{ij}^{act}(\mathbf{r}, t) = \frac{a + a^{'}}{2} f c(\mathbf{r}, t)(m_i m_j - \frac{1}{3}\delta_{ij}) + \mathcal{O}(\nabla) \tag{3.3}$$

where $c(\mathbf{r}, t)$ is the concentration of the particles. Note that to first-order, the active stress is the same for both polar and apolar particles. Higher-order terms are neglected in practice. For homogeneous active nematics the concentration is constant, which allows one to redefine the prefactors in eqn. 3.3 as a single constant known as the activity, $\zeta = \frac{a+a^{'}}{2} f c$.

Following the same procedure, as outlined in section 2.1, one can rewrite eqn. 3.3 in terms of the **Q**-tensor,

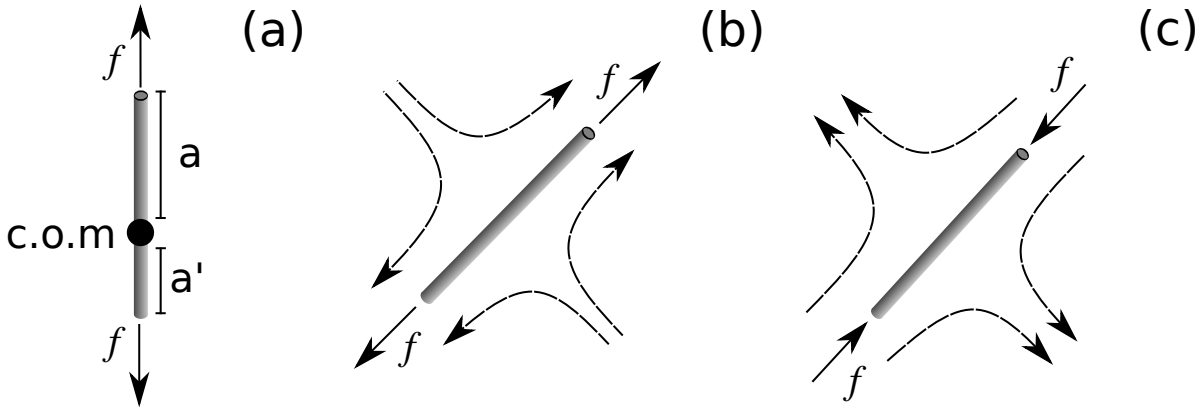


Figure 3.2: (a) Schematic of a rod-like particle with centre-of-mass given by the black dot, at a distance a and $a^{'}$ away from the two ends. The rod exerts a force f at the two ends, along the length of the rod. (b)-(c) Schematic of the flow fields (dashed black lines) that result from extensile and contractile forces respectively.

$$\sigma_{ij}^{act} = \zeta Q_{ij}. \tag{3.4}$$

The sign of the activity ζ plays an important role in active nematic fluids. If it is positive, then the forces are outwards along the direction of the director $\mathbf{n}$. The conservation of mass then requires that the fluid is sucked in from the sides of the rod. However, if the sign of the activity is negative, then the nematic particle pulls the fluid in along the nematic orientation $\mathbf{n}$, and pushes out along sides. This can be seen in the schematic Fig 3.2 (b) and (c) for extensile and contractile rods respectively.

3.2 Hydrodynamic Instabilities in Active Nematic Liquid Crystals

The activity of the particles gives rise to instabilities in the nematic field. To see why this is the case, consider a state initialised such that the director field is well-aligned up to some noise. In such a case, the elastic forces will try and smooth out any deformation in the director field. In contrast, the active stress will generate flows from any gradients in the nematic field. These flows reorient the $\mathbf{Q}$-tensor and so generate further deformations in the nematic field. The balancing between active and elastic forces results in instabilities of a given wavelength [49].

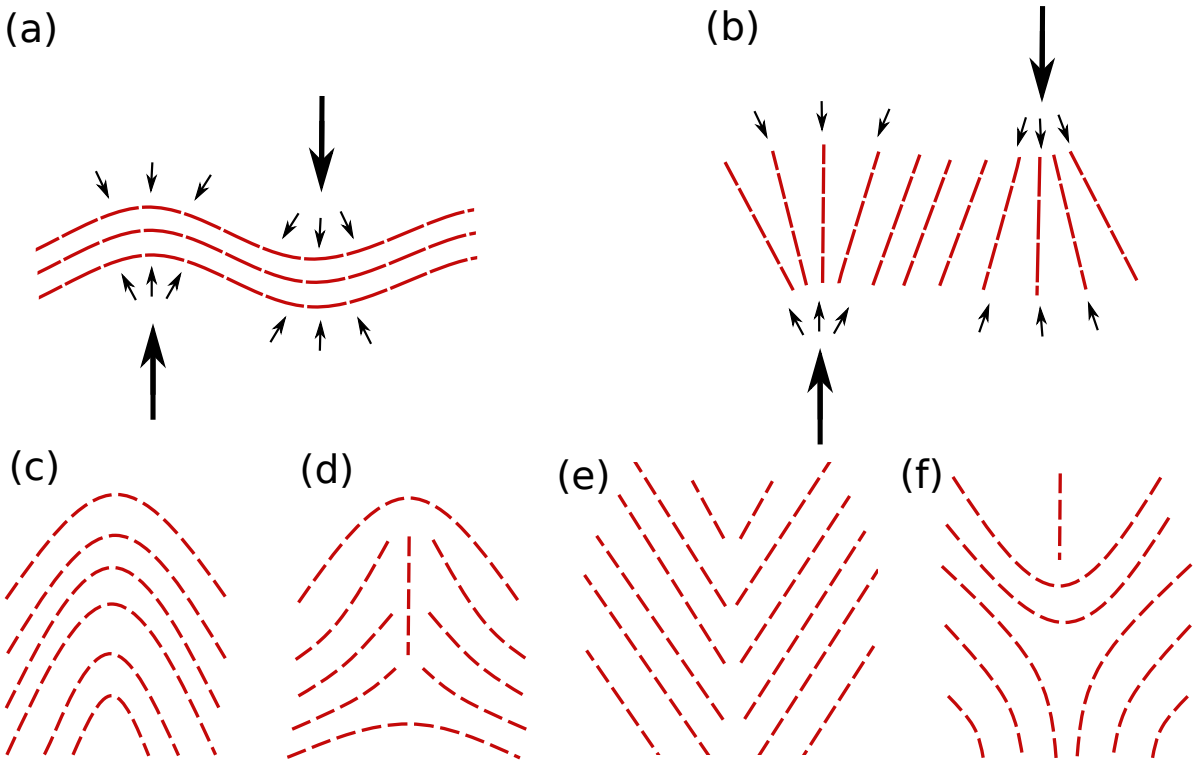


Figure 3.3: (a)-(b) Depictions of a bend and splay instability respectively, with the local flow fields given by small black arrows near the locations of the bend instability, and the resulting global shear flow given by the large black arrows. (c)-(d) Schematic of the creation of a $\pm\frac{1}{2}$ defect pair from a bend instability. (e)-(f) Creation of a $\pm\frac{1}{2}$ defect pair from a splay instability.

The type of nematic deformation depends on the sign of the activity. Extensile and contractile active nematics are unstable to different types of nematic deformation. Namely, extensile active nematics are unstable to bend instabilities, whereas contractile active nematics are unstable to splay deformations [50]. An intuition for this can be gained by looking at the flow fields around these instabilities. A schematic of a bend and splay deformation is given in Fig. 3.3 (a) and (b) respectively. These deformations are elastically unfavourable, but if the flows generated by the particles are strong enough the deformations will grow. To see why this is the case, consider the flow field around the bend instability in an extensile active nematic, as shown in Fig. 3.3 (a). The flow field is more concentrated on the concave side of the bend, than on the concave side, as indicated by the black arrows. This results in a shear flow which will act to deform the nematic field such that the deformation grows. For contractile active nematics which

are unstable to splay deformations, the force dipoles direct the flow inwards along the nematic orientation of the particles. This generates stronger flows on one side of the splay instability that the other, as indicated by the black arrows in Fig. 3.3 (b). Like in the extensile bend case, this results in a shear flow which acts to reorient the nematic particles such that the instability grows.

Bend and splay deformations are locations of large elastic energy. This is energetically costly and can result in the formation of $\pm\frac{1}{2}$ defect pairs in active nematics, which results in a lower elastic energy cost. This process is shown in Fig. 3.3 (c)-(d) for an extensile active nematic, and Fig. 3.3 (e)-(f) for a contractile active nematic. This is the only process in which topological defects are created in two-dimensional active nematics. These active defects behave differently from their passive counterparts, particularly because they generate flow-fields as we show in the next section.

3.3 Topological Defects in Active Nematic Liquid Crystals

Topological defects in active nematic liquid crystals behave markedly different to their passive counterparts. This is because the deformations in the nematic field around defect cores give rise to significant flows. The asymmetry of the flows generated by a $+\frac{1}{2}$ defect cause it to self-propel, while the symmetric flows generated by a $-\frac{1}{2}$ defect do not allow it to self-propel. Furthermore, they result in hydrodynamic interactions between neighbouring defects. Understanding these self-generated flow fields is important for understanding the dynamics of active nematics in general, and provides the motivation for this section.

The flow field around defects are well-defined, as outlined by [51]. To see this we first note that individual point defects can be described using an over damped equation of motion,

$$\beta(\partial_t \mathbf{r} - \mathbf{u}) = F \tag{3.5}$$

where β is a friction coefficient, $\mathbf{r}$ is the defect position, $\mathbf{u}$ is the local flow at the location of the defect core, and F is the net force acting on the defect, such as an elastic force.

If the dynamics of the flow are much faster than the dynamics of the director field,

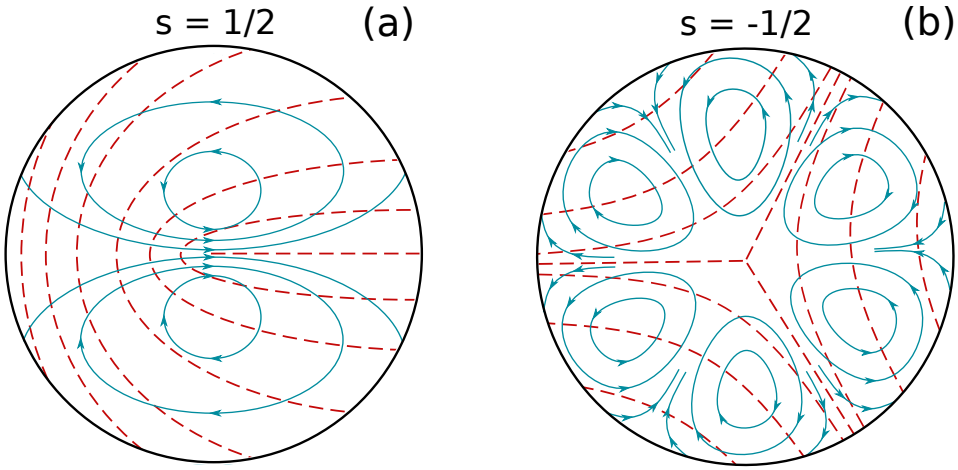


Figure 3.4: (a) and (b) depict the flow field (solid blue lines) and the director field (dashed red lines) around a $+\frac{1}{2}$ and $-\frac{1}{2}$ defect respectively.

the force F in eqn. 3.5 can be neglected such that $\mathbf{u}$ obeys the Stokes equations,

$$\eta\nabla^2\mathbf{u} - \nabla p + \mathbf{f} = 0, \tag{3.6}$$

$$\nabla \cdot \mathbf{u} = 0, \tag{3.7}$$

where η is the viscosity, $\mathbf{f} = \nabla \cdot \sigma^{\text{act}}$ accounts for the active forces, which are balanced by the viscous dissipation $\eta\nabla^2\mathbf{u}$ and pressure gradients ∇p. The solution for $\mathbf{u}$ is then given by,

$$u_i(\mathbf{r}) = \int \mathrm{d}A' G_{ij}(\mathbf{r} - \mathbf{r}')f_j(\mathbf{r}'), \tag{3.8}$$

where G_{ij} is the two-dimensional Oseen tensor. Taking $\mathbf{n} = (\cos(s\phi), \sin(s\phi))$ with $s = \pm\frac{1}{2}$ allows us to obtain the active body force as

$$f^{\text{act}} = \nabla \cdot \sigma^{\text{act}} = \frac{\zeta}{2r}\begin{cases} \hat{\mathbf{x}} & s = +\frac{1}{2}, \\ -\cos(2\phi)\hat{\mathbf{x}} + \sin(2\phi)\hat{\mathbf{y}} & s = -\frac{1}{2}, \end{cases} \tag{3.9}$$

for $\pm\frac{1}{2}$ defects, where we have chosen the symmetry axis to be $\hat{\mathbf{x}}$, and the nematic ordering $S = 1$ outside the core for simplicity. Substituting this force into the solution for the Stokes equations (eqn. 3.8) then yields the velocities,

$$\mathbf{v}_+(r,\phi) = \frac{\zeta}{12\eta}\{3(R-r) + r\cos(2\phi)\hat{\mathbf{x}} + r\sin(2\phi)\hat{\mathbf{y}}\}, \tag{3.10}$$

$$\mathbf{v}_-(r,\phi) = \frac{\zeta r}{12\eta R}\{(\frac{3}{4}r - R)\cos(2\phi) - \frac{R}{5}\cos(4\phi)]\hat{\mathbf{x}} + [(\frac{3}{4}r - R)\sin(2\phi)] + \frac{R}{5}\sin(4\phi)]\hat{\mathbf{y}}\}, \tag{3.11}$$

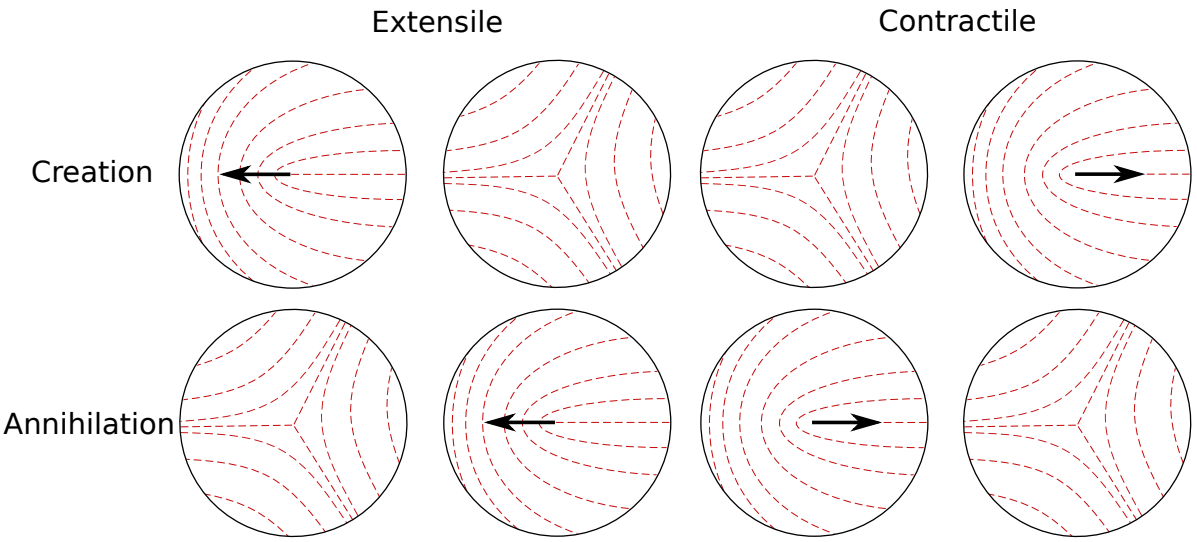


Figure 3.5: Schematic of defect-defect motion in extensile and contractile nematics. Creation events are given in the top row, and annihilation events in the bottom row. The first two columns are for extensile nematics, and the last two columns for contractile nematics.

for $+\frac{1}{2}$ and $-\frac{1}{2}$ defects respectively. The size of the system is given by R. A schematic of these flows are shown in Fig. 3.4 (a) and (b), where the dashed red lines indicate the nematic orientation and the solid blue lines indicate the flow field. Equation 3.10 indicates that the $+\frac{1}{2}$ defects are self-advected by the flows they generate via the active stress, since $\mathbf{v}_+(0,\phi) = \frac{\zeta R}{3\eta}$. However, eqn. 3.11 shows that -$\frac{1}{2}$ defects are not self-advected by their flows, since $\mathbf{v}_-(0,\phi) = 0$. This propulsive nature, or lack thereof, makes sense from looking at the polar symmetry in the flow fields in Fig. 3.4 (a) for $+\frac{1}{2}$ defects, and three-fold symmetry in Fig. 3.4 (b) for $-\frac{1}{2}$ defects.

The self-propulsion of $+\frac{1}{2}$ defects influences the creation and annihilation of defects pairs. It is worth noting that elastic forces act to annihilate defect pairs, making creation events in passive nematic liquid crystals difficult. In contrast, the self-propulsion of $+\frac{1}{2}$ defects in active nematic liquid crystals allows the defect pair to separate, given the $+\frac{1}{2}$ defects motion is orientated away from the $-\frac{1}{2}$ defect. This process is shown in the top row of Fig. 3.4, for extensile and contractile active nematics. Note that the $+\frac{1}{2}$ defects in contractile active nematics move in the opposite direction of those in extensile active nematics. This can be seen by changing the sign of ζ for the defect velocity in eqn.

3.10. However, the self-propulsion of $+\frac{1}{2}$ defects can exacerbate annihilation if they are directed towards $-\frac{1}{2}$ defects, as shown in the bottom row of Fig. 3.4.

3.4 Active Turbulence

The flow fields generated by the active particles result in bend and splay instabilities of the nematic field which result in the generation of topological defects. These defects also generate flow fields, leading to more deformations in the nematic field, which creates new defects. The collision of $\pm\frac{1}{2}$ defect pairs results in their annihilation. Overall, this process results in a steady-state population of defects along with jets and vortices in the flow field. When this state arises, it is termed active turbulence [52]. A snapshot is shown in Fig. 3.6, with the nematic field is depicted by the black dashes, the $+\frac{1}{2}$ defects by black discs, and the $-\frac{1}{2}$ defects by white diamonds. The colourmap in Fig. 3.6 (a) shows the nematic order parameter S, while the colourmap in Fig. 3.6 (b) shows the corresponding vorticity field.

The mean distance between defects defines the "active lengthscale" [53], and can be estimated as

$$l_{act} = \sqrt{\frac{K}{\zeta}} \tag{3.12}$$

where K is the Frank elastic constant and ζ is the activity. From this definition, it is clear that increasing the strength of the force dipoles results in a smaller length scale, meaning defects are closer on average. This is equivalent to a larger steady-state population of defects, which makes sense because more energy is being injected into the system at the particle level. Conversely, increasing the energetic cost of elastic deformations results in a larger active lengthscale. This also makes sense since the bend and splay deformations spread out and so the mean defect-defect distance will decrease, lowering the average number of defects in the bulk.

It is worth noting that there are important differences between inertial turbulence and active turbulence. Firstly, the Reynolds number in active turbulence is very small, while it is large for inertial turbulence. Despite the low Reynolds numbers the flows in active turbulence exhibit jets and vortices, resembling that of inertial turbulence. Secondly, the energy injection occurs at the particle level for active nematic fluids, whereas

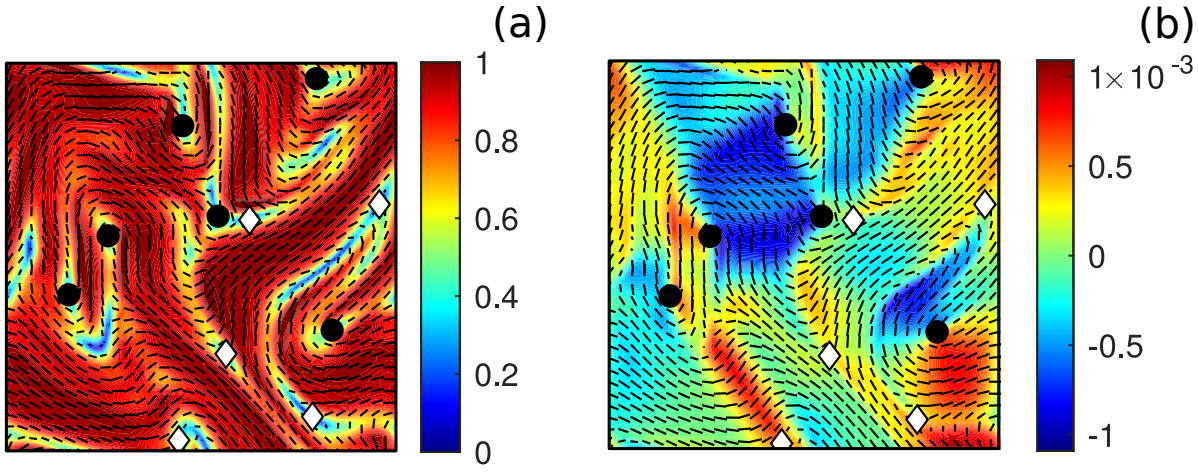


Figure 3.6: Snapshot of active turbulence. (a) The nematic field is given by the black dashes, the $+\frac{1}{2}$ defects by black discs, and $-\frac{1}{2}$ defects by white diamonds. The underlying colourmap depicts the nematic order parameter S. (b) Similar to panel (a) except the underlying colourmap shows the vorticity.

the energy is injected at length scales much larger than that of the particles in inertial turbulence.

3.5 Intrinsic Free Energy

At the start of this chapter, a collection of experimental systems with clear active nematic behaviour was introduced. In the model presented so far, one requires the existence of a Landau-de Gennes bulk free energy to impose nematic order below some critical temperature. However, if the activity is turned off we expect most experimental systems to be in the isotropic phase. Interestingly, previous research [54] has shown that the activity itself can give rise to nematic ordering through an 'intrinsic free energy' which is similar in form to the Landau-de Gennes bulk free energy.

To see how this arises, we neglect the backflow generated by the elastic stresses, which is valid as they are measured to be an order of magnitude lower than the active stresses. Including the active stress (eqn. 3.4) in eqn. 2.18, and balancing the viscous and active stresses gives

$$2\eta E_{ij} = \zeta \phi Q_{ij}. \tag{3.13}$$

Substituting this into the three-dimensional Beris-Edwards equation and simplifying gives,

$$(\partial_t + u_k\partial_k)Q_{ij} - \Omega_{ik}Q_{kj} + Q_{ik}\Omega_{kj} = \Gamma_Q H_{ij}^{(eff.)}, \tag{3.14}$$

where $\mathbf{H}^{(eff.)}$ is an effective molecular field modified by the active flows. The corresponding effective free energy is

$$\mathcal{F}_{eff} = \mathcal{F}_{bulk} + \mathcal{F}_{grad} + \frac{\lambda\zeta\phi}{\eta\Gamma_Q}(\frac{1}{6}tr(Q^2) - \frac{1}{3}tr(Q^3) + \frac{1}{4}tr(Q^4)) \tag{3.15}$$

where $\mathcal{F}_{bulk}$ and $\mathcal{F}_{grad}$ are the Landau-de Gennes bulk and elastic-free energy respectively. The rest of the terms in eqn. 3.15 have the same form as the Landau-de Gennes bulk free energy and arise purely due to the active stress. The result of this is that activity induces nematic ordering.

It is also worth noting that the intrinsic free energy only gives rise to nematic order for particular configurations of the alignment parameter λ and activity ζ, since the sign of the coefficients in $\mathcal{F}_{eff}$ depend on the sign of $\lambda\zeta$. So for extensile systems with $\zeta > 0$, only positive values of the alignment parameter will give rise to nematic order, while contractile systems with $\zeta < 0$ will only have nematic order for negative values of the alignment parameter.

3.6 Active Anchoring

The activity not only influences the ordering of the nematic field in the bulk, but also along interfaces. A particularly nice example of this can be seen in growing colonies of *Escherichia coli* [12] where the bacteria align parallel to the interface. Naively, one might expect that, in the absence of an applied anchoring free energy like that in eqn. 2.11, the nematic field will have no preferred angle at the interface. However, in simulations of isotropic-nematic phase-separated active nematics, this is not found to be the case. There is a clear effective alignment of the nematic field at the boundary between a nematic region and an isotropic region. This arises because of the active flows and is termed active anchoring [55].

To see the origin of the active anchoring, note that defining the unit normal vector to the interface as $\mathbf{m}$, gives the active stress density $\nabla(\zeta\mathbf{Q})$ as

$$F^{act} = \zeta|\nabla S|(2(\mathbf{m}\cdot\mathbf{n})\mathbf{n} - \mathbf{m}) - 2S\zeta(\mathbf{n}(\nabla\cdot\mathbf{n}) + (\mathbf{n}\cdot\nabla)\mathbf{n}). \tag{3.16}$$

The first term is proportional to gradients in the nematic order, while the second term accounts for gradients in the director field. This latter term may be neglected if the distortions are small, which we assume to be the case here. Using this assumption, the active forces perpendicular and parallel to the nematic field are

$$F_{\perp}^{act} = \zeta|\nabla S|(2(\mathbf{m}\cdot\mathbf{n})^2 - 1), \tag{3.17}$$

$$F_{\parallel}^{act} = \zeta|\nabla S|(\mathbf{m}\cdot\mathbf{n})(\mathbf{l}\cdot\mathbf{n}), \tag{3.18}$$

where $\mathbf{l}$ is the unit vector tangent to the surface. Each of these two terms contributes to active anchoring.

The first term $F_{\perp}^{act}$ describes the force perpendicular to the surface. If the nematic field is parallel to the surface then $F_{\perp}^{act} = -\zeta|\nabla S|$ while if it is normal to the surface $F_{\perp}^{act} = \zeta|\nabla S|$. For extensile nematics, this will cause a force pushing the surface inwards if the nematic field is parallel to the surface, and outward if it is normal to the surface. For contractile nematics, this sign of the force changes, so the surface gets pushed outwards if the nematic field is parallel to the surface, while it gets pushed in if its perpendicular to the surface. If the surface is free to move, then this causes extensile surfaces to elongate regions where the nematic field is parallel to the surface, while contractile nematics will elongate regions where the nematic field is perpendicular to the surface.

The second term $F_{\parallel}^{act}$ also plays a role an important role in active anchoring. Note that it is zero whenever the director orients parallel or perpendicular to the surface, since in either case $\mathbf{m}\cdot\mathbf{n}$ or $\mathbf{m}\cdot\mathbf{l}$ is zero. However, when the director field aligns at any other angle to the surface, a non-zero active force $F_{\parallel}^{act}$ results in flows along the interface. In the flow tumbling regime these flows will then reorient the nematic field. For extensile nematics, this will cause the nematic field to align parallel to the surface, while contractile nematics will align perpendicular to the surface.

Overall, the active anchoring causes extensile active nematics to align parallel to the interface and contractile active nematics to align perpendicular to the interface. Experimentally it has been observed that bacteria align parallel to the interface in growing colonies [12] leading to suggestions that their division is a source of extensile stress. In migrating colonies of chemotactic cells [22, 27], the elongation axis of the cells at the interface align perpendicular to the interface suggesting that they exhibit contractile forces.

3.7 Controlling Active Nematic Flows

The chaotic nature of active nematic fluids can be tamed through different mechanisms such as substrate friction, anisotropic viscosity, and confinement [36]. Each of these methods screens the hydrodynamic flows at a specific length scale.

Introducing a friction term $-\beta\mathbf{u}$ into the momentum equation, causes the flows to become screened on a lengthscale $L_{fric} \sim \sqrt{\zeta/\rho\beta}$. When $L_{fric} \sim l_{act}$, the active turbulence self-organises into a regular lattice of vortices [56]. The vortex lattice can be seen in Fig. 3.7 (a), which shows the fluid velocity coloured by the magnitude of the vorticity. This state is also characterised by a topological defect lattice, which can be seen in Fig. 3.7 (b), which shows the director field with $+\frac{1}{2}$ and $-\frac{1}{2}$ defects highlighted by the red and yellow markers respectively. It is also worth noting that the increase in friction slows down the speed at which defects move, leading to an increase in the size of their population since there are fewer annihilation events. Although at very high friction, the dissipation of energy balances the injection of energy, and the number of defects drops to zero.

Anisotropic viscosity can be used to order active turbulent flows along a given direction. One mechanism to do this involves mixing a smectic liquid crystal into a microtubule-kinesin suspension [19]. When a magnetic field is exerted on the liquid crystal, the particles organise into a "bookshelf" type pattern, as shown in the top panel of Fig. 3.7 (c), where the orange rods depict passive liquid crystal particles and H is the direction of the magnetic field. In this state, the underlying passive liquid crystal flows like a liquid along the planes but responds like a solid in the orthogonal direction. As a result, the active nematic feels an interfacial viscosity that is much larger along the magnetic field, than perpendicular to it, causing the active fluid to organise into lanes of uniform width as shown in the middle panel of Fig. 3.7 (c), which is even more prominent when their position is averaged across time, as shown in the bottom panel of Fig. 3.7 (c). The topological defects align and move in anti-parallel directions in adjacent lanes. The velocity inside each lane is laminar, and anti-parallel to its neighbouring lanes, as shown in Fig. 3.7 (d). The passive liquid crystal enters a nematic state above a critical temperature, in which case the active fluid exhibits active turbulence. Thus, this system allows for strong control over the active nematic flows.

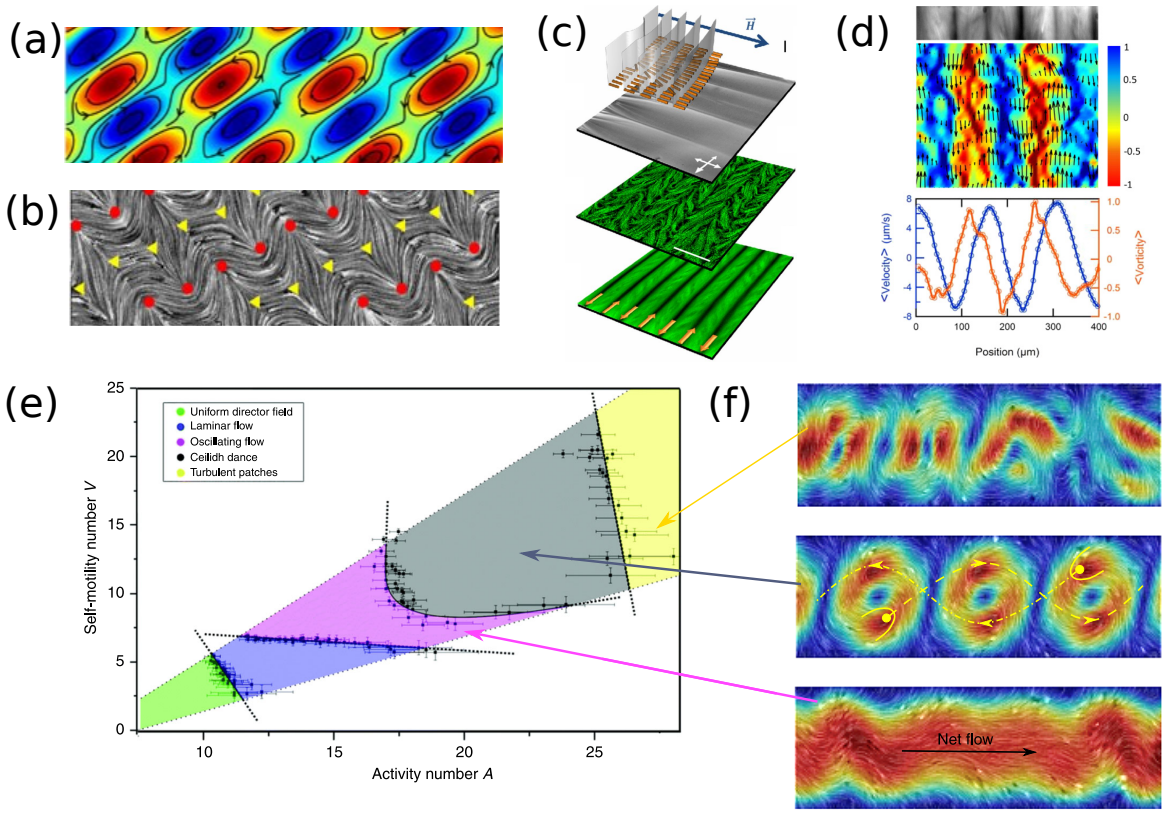


Figure 3.7: (a) Velocity field coloured by the magnitude of the vorticity, (b) director fields with $+\frac{1}{2}$ and $-\frac{1}{2}$ defects denoted by red circles and yellow triangles, adapted from [56]. (c) Top: polarizing optical micrograph, and configuration of the underlying molecular planes in the SmA phase of the passive liquid crystal. Middle: fluorescence confocal micrograph revealing the correlation between the aligned active nematic and the anisotropic SmA phase. Bottom: Time average of the dynamic pattern. The arrows depict the antiparallel flow directions along the lanes of defect cores (Scale bars: 100 μm.). (d) Active flow along self-organized lanes. Top-panel: time-averaged fluorescence micrograph of the micro-tubule suspension. Middle-panel: velocity field (vectors) with the normalised vorticity as the colourmap. Bottom-panel: Downstream average of velocity and vorticity across the horizontal position. (c) and (d) were adapted from [19]. (e) Regions of stability of different flow states as a function of the activity number $A = w/l_{act}$, and the $+\frac{1}{2}$ defect self-motility V (i.e. the $+\frac{1}{2}$ defect velocity relative to the background velocity). (f) Streamlines coloured by the normalised magnitude of the velocity. (e) and (f) were adapted from [36].

Physical confinement has also been found to screen flows. Placing bacterial suspensions and cell layers in confinement has resulted in a rich range of behaviour, for example, spiral vortices [57, 58], synchronised vortex lattices [59], unidirectional flows [60–62], shear flows [46] and freezing [9, 63]. Similarly, confining active mixtures of microtubules and motor proteins to circular domains [64–66], in vesicles [18] or droplets [67, 68] and to more complex geometries such as tori [69, 70], have also been studied to probe the effects of interfacial viscosity, curvature and 3D confinement.

In tandem, simulations have provided insight into how confinement influences the flows in active nematic systems. For example, simulations of two-dimensional active nematics confined in a channel with periodic boundary conditions demonstrate a wide range of states as the channel width is varied [20]. The width of the channel, w, acts as the screening length scale in these systems. The ratio of w and l_{act} defines a dimensionless parameter known as the activity number $A = \frac{w}{l_{act}}$, which can be used to identify which state the system is in according to the phase diagram in Fig. 3.7 (e). The self-motility number V, is the ratio of the $+\frac{1}{2}$ defect velocity (given by eqn. 3.10) and the characteristic velocity of the active nematic fluid [49]. For large activity numbers, where the active lengthscale is much smaller than the channel width, the system exhibits active turbulent patches, as shown in Fig. 3.10 (f) top panel. However, if the channel width is about the size of the active lengthscale, then the flows organise into a one-dimensional lattice of vortices, as shown in Fig. 3.10 (f) middle panel. This state, known as the dancing disclination state, is also characterised by the existence of two populations of topological defects which move in opposite directions, along sinusoidal trajectories. If the active lengthscale is increased above the channel width, then the flows oscillate and then become laminar. Further increases in the active lengthscale result in the flows no longer being generated, with a uniform director field, as shown in Fig. 3.10 (f) bottom panel. This system shows that confinement can be used to control the self-generating flows of active nematic fluids.

In the next chapter, we investigate how the dynamics of an active fluid can be controlled in a closed channel. In particular, we will explore the emergence of a new length scale, distinct from the active length scale that regulates the dynamics of unconfined systems. We also find a novel flow state, and compare the results from simulations to experiments.

Chapter 4

Reconfigurable flows and defect landscape of confined active nematics

In this chapter, we investigate the physics of active nematic liquid crystals in confinement. Unconfined dynamics are mostly governed by the interplay between elastic forces that align the constituent particles, and active stresses that destabilize the nematic field, with constant nucleation of topological defects and chaotic flows, as outlined in Chapter 3. The average distance between defects, also called the active length scale, depends on the competition between the elastic and active stresses and is independent of geometry. I performed simulations of active nematic liquid crystals, to show that the intrinsic active length scale loses its relevance under strong lateral confinement, in a closed channel. Instead, the close interplay between the velocity field and the defect dynamics highlights the emergence of a new length scale that does not depend on the activity but merely on geometrical parameters.

Further, we find a rich range of dynamical behaviours, depending on the channel width. More specifically, we uncover a defect-free regime of shear flow in narrow channels. In this regime, the defects are created and annihilated on the channel walls rather than in the bulk, and acquire a strong orientational order in narrow channels. Their nucleation is governed by an instability whose wavelength is effectively screened by the channel width.

By increasing the channel width, the defect lifetime increases, developing a spatio-temporal organization that corresponds to the predicted state of dancing vortical flows [20]. Increasing the channel width further resulted in full disorganization into the active turbulence regime, as is typical of the unconfined active nematic.

These results are recovered in experiments of microtubule/kinesin suspensions, an

experimental model active nematic system. They were performed at the University of Barcelona by Jérôme Hardoüin. This work has been published in Nature Communications Physics [48].

4.1 Computational Setup

We model a two-dimensional active nematic fluid, confined to a closed channel. The fields that describe the system are the total density ρ, the velocity $\boldsymbol{u}$, and the nematic tensor $\mathbf{Q} = S(\mathbf{nn} - \mathbf{I}/2)$, that describes both the orientation ($\mathbf{n}$) and the magnitude (S) of alignment of the nematogens. The $\mathbf{Q}$-tensor evolves according to the Beris-Edwards equation (eqn. 2.13). The total density ρ satisfies the continuity equation (eqn. 2.16) and the velocity $\mathbf{u}$ evolves according to the Navier-Stokes equation (eqn. 2.17), with stress tensor given in eqn. 2.18.

The free energy includes two terms. The first is an elastic-free energy density $\mathcal{F}_{\nabla Q} = \frac{1}{2}K(\boldsymbol{\nabla}\mathbf{Q})^2$ (eqn. 2.10), which penalises any deformations in the orientation field of the nematogens and where we assume a single elastic constant K. We note that the free energy functional does not include any Landau-de Gennes bulk free energy terms: all the ordering in the simulations arises from the activity [54]. This is motivated by the fact that there is no equilibrium nematic order in the experimental system without ATP (i.e. in the absence of active driving). The second contribution to the free energy is a surface anchoring, $\frac{1}{2}\mathcal{W}\mathrm{Tr}(\mathbf{Q} - \mathbf{Q}_D)^2$ (eqn. 2.11).

To correspond to the experiments $\mathbf{Q}_D$ is chosen so that the director prefers to align parallel to the boundary walls. The strength of anchoring at the boundaries, $\mathcal{W}$, is set to values corresponding to weak anchoring so that the nematogens can re-orientate at the walls to allow defects to form there. The corners have $\mathbf{Q}_D$ such that the director field aligns at an angle of 45 degrees to the length of the channel, on the front-right and back-left corners, and at an angle of 135 degrees on the front-left and back-right corners. In the experiments, the microtubules slide over the walls and therefore free-slip boundary condition was imposed on the velocity field.

The magnitude of the anchoring was made "weak" enough so that the nematic field prefers to align parallel to the boundary, but not too "strong" so that the active nematic instabilities could not form along the wall. This latter point is important for the $-\frac{1}{2}$ defects to form at the wall. A natural dimensionless parameter to quantify the relative

Parameter	**Symbol**	**Value**
Alignment parameter	$\hat{\xi}$	0.9
Anchoring srength	$\mathcal{W}$	0.002
Total density	ρ	40
Rotational diffusivity	Γ_Q	0.4
Elastic constant	K	0.015
Viscosity	η	1/6
Channel length	L	1800
Channel width	w	30 - 160
Activity	ζ	0.0072 - 0.01

Table 4.1: Parameters used in the simulations. The specific values for ζ are 0.0072, 0.0075, 0.0082, 0.0092 and 0.01. All values are in LB units.

strength of the anchoring to the active stress is $\frac{\mathcal{W}}{\zeta}$. Weak anchoring can then be defined as the values of ζ and $\mathcal{W}$, such that $0 < \frac{\mathcal{W}}{\zeta} < 1$. This range allows for instabilities to form at regions of large active nematic stress (for example near a defect), while keeping the nematic field parallel to the boundary at regions of negligible active stress (for example, in regions where the nematic field is well aligned, or $S \approx 1$). If $1 < \frac{\mathcal{W}}{\zeta}$, it becomes too energetically costly for the nematic field to not align parallel to the boundary. All simulations were performed on a $1800 \times w$ rectangular grid, where w varied from 30 to 160 lattice sites.

The parameters used in the simulations are given in Table 4.1. Initially, we chose parameters in a range that has previously been successful in reproducing the dynamics of experiments in microtubule bundles [71, 72], and then further refined the parameters via a search in phase space. All simulations were run for up to 300,000 simulation time steps. Some simulations were performed up to 1,000,000 time steps to further test the stability of the simulations. The initial velocity field was set to zero everywhere in the domain. The orientation of the director field was initialised at an angle of either 0, 35 or 90 degrees to the length of the channel, up to some noise.

In the simulations, the instability wavelength of the director field λ_i was calculated as follows. At any given channel width and time-step, the distance between each +1/2 defect and its nearest neighbour was calculated. The mean of this quantity was then taken, to give the mean defect-defect distance at a fixed time. Then an average over time

was taken to give λ_i for a single simulation. This process was repeated for three different simulations with different initial conditions. The initial conditions were distinguished by the initialisation angle of the director field, which was selected to be 0, 45 and 90 degrees to the length of the channel. The mean value of these λ_i's was then taken as the measurement for λ_i. The standard deviation of these values was used to get the error bars.

4.2 Experimental setup

The simulations were compared to experiments performed by Jerome Hardouin at the University of Barcelona. The experimental system was composed of self-propelling elongated units formed by bundled microtubules powered by Adenosine Triphosphate (ATP)-consuming kinesin [122], previously discussed in chapter 1. The addition of the depleting agent polyethylene glycol (PEG) concentrated microtubules into bundles, hundreds of microns long. Within each bundle, the kinesin motors bridged neighbouring microtubules and walked towards their positive ends leading to internal sliding of filaments of opposite polarity.

The active nematic was prepared using an open-cell design [73], in which 2μL of the active aqueous microtubule-mixture was placed inside a custom-made pool of 5mm diameter and was covered with 60μL of 100cS silicon oil. Within 30 minutes, an active nematic layer extended over the whole surface of the pool. Driven by the motors, the microtubule bundles at the interface continuously extended and buckled. This gave rise to the dynamical steady state of active turbulence.

The layer of active nematic was confined in rectangular enclosures by means of micro-printed polymer grids of 100μm thickness that were placed in contact with the oil/aqueous interface, see Fig. 4.1. The active nematic remained in contact with the active bulk solution underneath, thus ensuring activity and material parameters were equal in all channels.

4.3 Flow States

The main computational control parameters of our system are channel width, w, and the activity ζ. The activity is determined by the concentration of ATP in experiments. In this section, we describe how both the defect landscape and flow patterns evolve

as w is increased based on simulations (Fig. 4.2 a-c) and experiments (Fig. 4.2 d-f). We identify two well defined regimes: a shear flow regime, observed for $w < 40$ lattice sites ($w < 80$ μm), which is transiently defect-free (Fig. 4.2a, Fig. 4.2d), and the dancing defects regime, for $w > 45$ lattice-sites ($w > 90$ μm) (Fig. 4.2b, Fig. 4.2e). The transition between these two regimes is not sharp. For values of w in the range $40 - 45$ lattice sites ($80 - 90$ μm), the direction of the shear is not uniform along the channel, but rather composed of patchy domains where shear flow spontaneously arises with a random direction, and is then quickly disrupted by instabilities. Finally, the unconfined active nematics is obtained for $w > 90$ lattice sites ($w > 120$ μm) (Fig. 4.2c and Fig. 4.2f). In the simulations, an additional, collapsing state, was found for $w < 30$ lattice-sites.

We find that the relevant parameter setting the dynamic state in the system is λ/w, where λ is the mean defect separation (Fig. 4.3). The latter is defined as $\lambda = (Lw/N)^{1/2}$, where L is the length of a given channel, w its width, and N the number of defects aver-

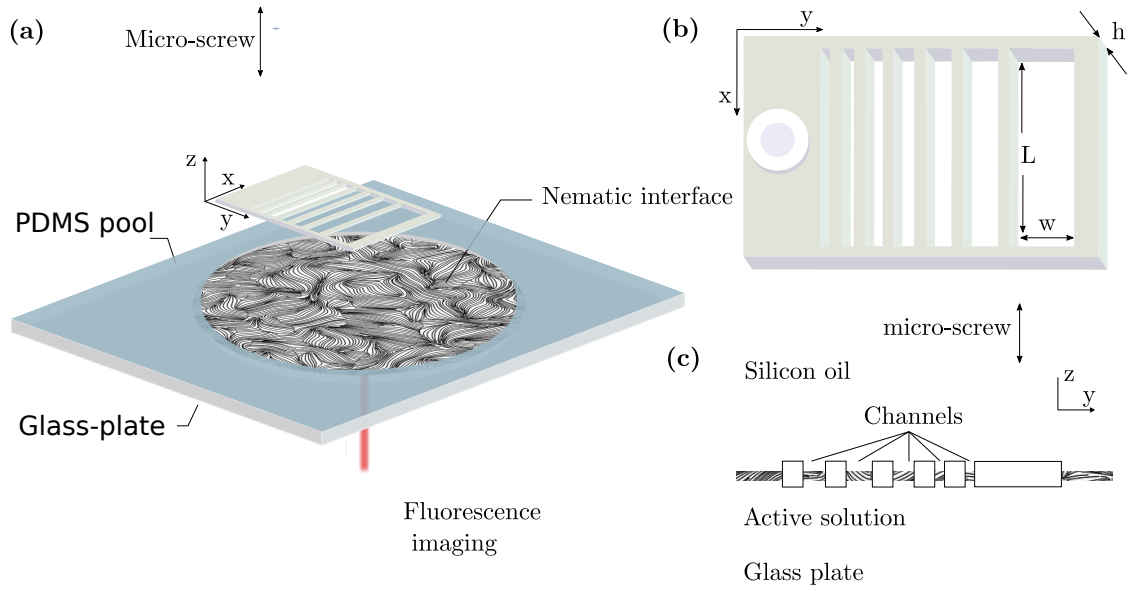


Figure 4.1: Experimental setup. (a) A polymer grid with rectangular openings is placed, by means of a micropositioner, in the custom-made elastomer pool that contains the aqueous active fluid and the passive oil. (b) Top view with a sketch of the grid including the relevant spatial dimensions. (c) The grid is placed in contact with the oil/water interface. In contact with the grid, the active nematic layer forms only inside the grid openings.

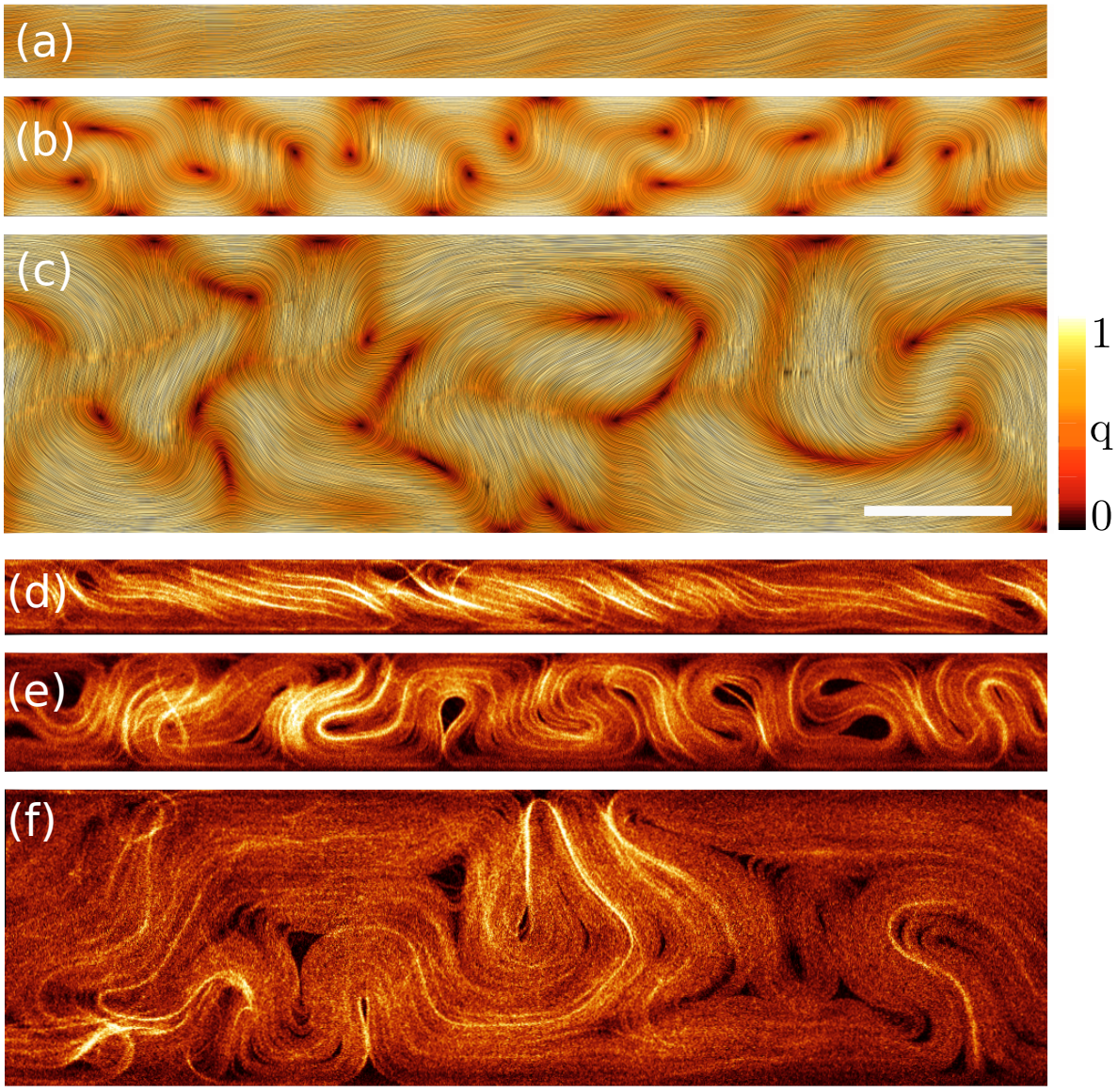


Figure 4.2: **Flow States.** (a-c) Simulations of the confined active nematic liquid crystal. Streaking patterns follow the director field tangents. They are produced using a Line Integral Convolution of the director field [74] with Paraview software. The colour map corresponds to the computed nematic order parameter, q. (a-c) Confocal fluorescence micrographs of the experiments active nematic interface confined in channels of different widths. *Scale bar:* 100μm. Panels a and d correspond to strong confinement, where the filaments are organized into an unstable alignment regime. Panels b and e illustrate the effects of moderate confinement, forcing a new dynamical regime of the defects. Panels c and f correspond to the active turbulence regime.

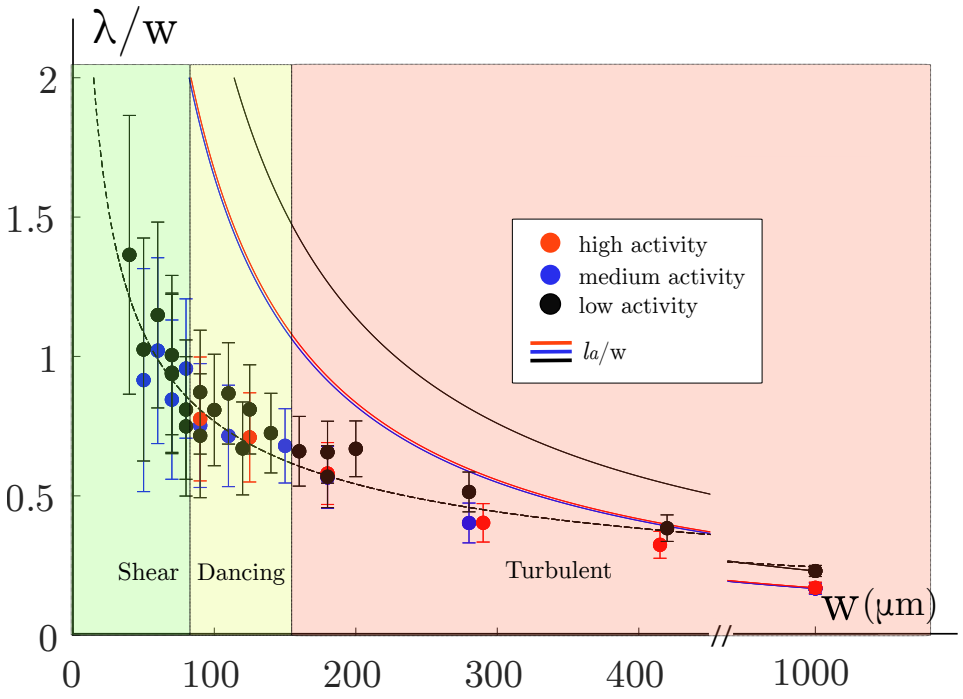


Figure 4.3: **Defect Spacing.** Mean defect spacing, λ, rescaled by the channel width, w, as a function of w. Different colours correspond to different activities. The error bars correspond to the standard deviation for measurements at 10 random times for each experiment. The dotted line corresponds to a fit with $w^{-1/2}$. The continuous lines correspond to $\lambda/w = l_a/w$ for each experiment, with l_a being the active length scale corresponding to the value of λ in the unconfined case.

aged in time. For unconfined active nematics, this length scale coincides with the active length scale $l_a = \sqrt{K/\zeta}$, which determines the vortex size distribution and corresponds to the mean defect separation [64, 75, 99]. However, we find that, in confined active nematics, λ is no longer equal to l_a. Instead, it significantly decreases with the channel width.

In the following, the flow dynamics and the defect landscape are analyzed, combining experiments and simulations, for the simple shear (Fig 4.4a), flow switching (Fig 4.4b), and defect dancing (Fig 4.4c) regimes.

4.4 Defect-free shear flow disrupted by instabilities

The shear flow regime is a defect-free state that appears for $\lambda/w > 1$ (Fig. 4.3), computationally realized here for $w < 40$ lattice-sites ($w < 80$ μm). The active nematic is primarily aligned parallel to the walls over distances that can persist along the whole channel as shown in Fig 4.4 (a). A global shear deformation is observed, with flows along the channel. The maximum velocities are measured at the walls, with opposite signs, and the velocity perpendicular to the walls is negligible. The shear rate, characterised by the slope of the velocity profile, is approximately constant over a relatively large range of channel widths. This is as expected because the activity, and hence the energy input per unit area, which must be balanced by the viscous dissipation due to the shear, is the same for all channels.

This aligned, defect-free configuration shares visual similarities with the banding patterns that emerge in simulations of dry systems of self-propelled particles with nematic alignment [76, 77]. A fundamental difference with our system, which is continuous rather than composed of discrete particles, is the fact that, in our case, nematic order is intrinsic, and flow alignment is the result of hydrodynamic and elastic interactions with the boundaries. In contrast, in the mentioned dry systems, nematic order is restricted to bands that arise from giant density fluctuations allowed by the compressible nature of the particle ensembles.

As argued in [6, 19, 50, 78], extensile active nematics, such as the one that we use here, are intrinsically unstable to bend deformations in aligned conformations. As a consequence, the sheared state eventually leads to local bend instabilities as shown in Fig. 4.4 (b). As a result, the velocity field repeatedly switches between two different states: longitudinal shear flow and a transversal instability regime. The dynamics of the switching behaviour and the coexistence of the shear and the instability states can be best illustrated in a space-time diagram of the averaged velocity components in the channel, as shown in Fig. 4.5 (a-b). In the shear state, the velocity perpendicular to the boundaries and averaged across the channel width, $\langle V_y(x)\rangle_y$, vanishes, while the velocity component parallel to the channel walls and averaged along the channel length, $\langle V_x(y)\rangle_x$, is maximum at the walls. Once bend instabilities are triggered, defect pairs form and $+1/2$ defects propagate across the channel and dismantle the shear state, which leads to the emergence of non-zero values of $\langle V_y(x)\rangle_y$ with a well-defined length scale along the channel. The defects eventually reach the opposing wall and annihilate,

such that the shear state is reestablished. As is apparent from Fig. 4.5 (a-b), over time the active system alternates between the two regimes. Simulations allowed us to test channel widths well below the experimental capabilities, allowing us to explore the $\lambda \gg w$ regime. For these conditions, we observed stable shear flow, as any pairs of defects that were generated at the channel walls immediately self-annihilated.

The instability takes the form of a sinusoidal deformation of the aligned nematic field, with a well-defined length-scale along the channel. As the perturbation progresses, defects are rapidly nucleated from the walls, at regularly-spaced positions coinciding with the maxima of the sinusoidal perturbation. We measured the wavelength of the instability and found that it scales with the channel width (Fig. 4.6a-c). This is strong evidence that the hydrodynamics is screened, and that the channel width is important in controlling the flows.

Upon their nucleation at the boundaries, the orientation of the $+1/2$ defects is strongly anisotropic (see Fig. 4.7(a)). They preferentially align perpendicular to the walls and, due to their active self-propulsion [79, 80, 122], they move away from the walls into the bulk. On the contrary, because of their three-fold symmetric configuration, $-1/2$ defects have no self-propulsion and remain in the vicinity of the walls [20]. Eventually, the $+1/2$ defects reach the opposite wall and annihilate with negative defects residing close to it. In this way, the defect-free phase is periodically restored. Remarkably, even though no chirality is observed in the sheared state, as we repeat the simulations and experiments, the handedness of the shear flow initially selected is preserved through successive instability cycles. This memory can be explained by observing that the instability is triggered locally and that it is entrained by the neighbouring sheared regions.

In a recent paper, Opathalage et al [66] have reported similar defect nucleation at the boundaries for a microtubule/kinesin mixture in circular confinement with no-slip boundary conditions and planar anchoring. They attribute the rate of defect formation to a combination of the build-up of microtubule density at the boundary increasing local active stresses and a change in the azimuthal force as circular flows wind the microtubules around the confining disk. In the simulations, the density of the microtubules is constant, and in the experiments variation of microtubule density across the channel is small (except in defect cores) and the instability period is controlled by the time taken to realign the microtubules parallel to the walls after each instability. This realignment period not only decreases significantly for increasing channel width, but also for increasing activity.

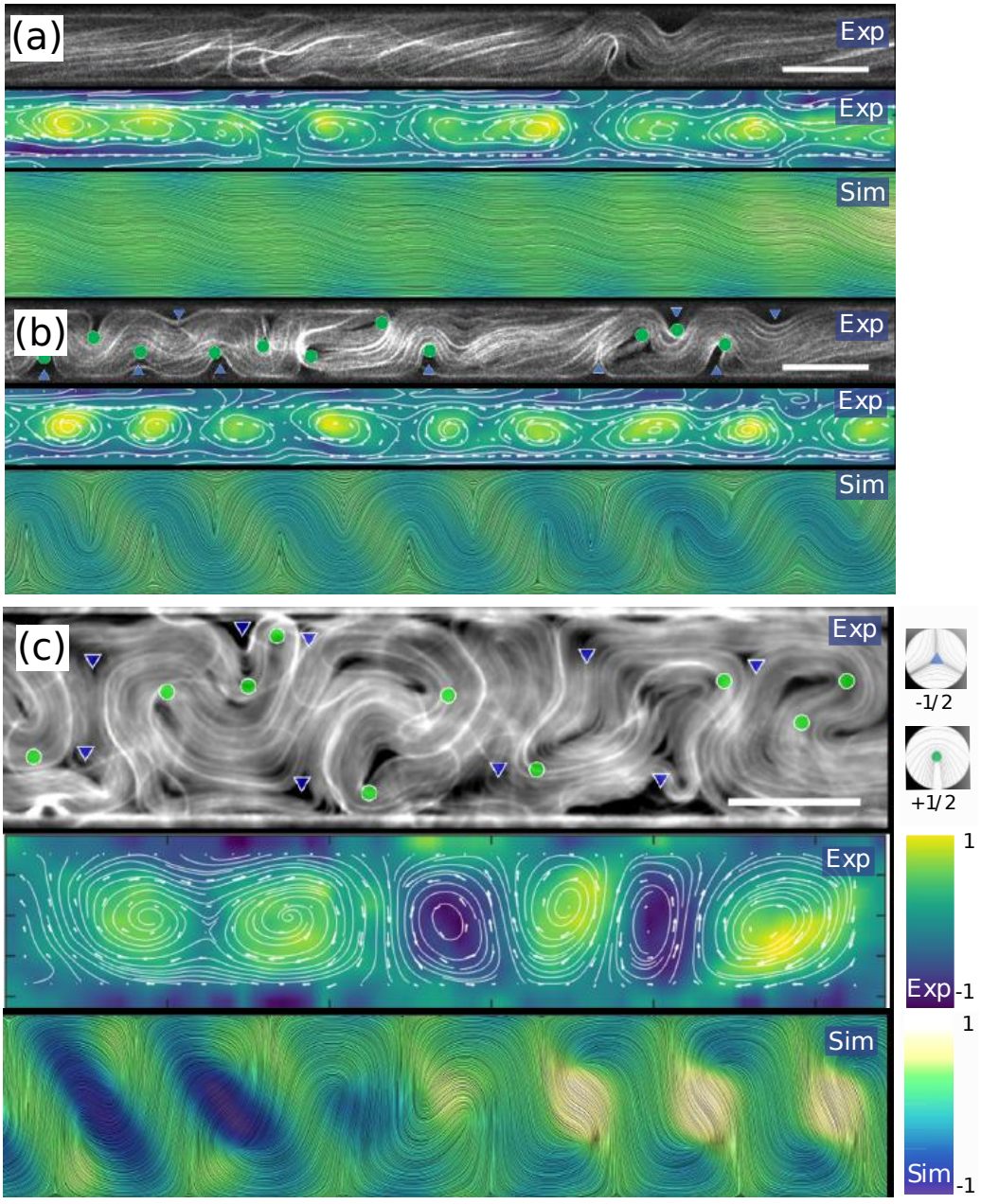


Figure 4.4: **Flow patterns.** (a-c) Each panel is composed of (top) a snapshot of a typical confocal fluorescence image of the active nematic, with defect locations overlaid, (centre) experimental Particle Image Velocimetry measurement of the flow patterns, coloured by the normalized vorticity, with velocity streamlines overlaid and (bottom) numerical simulations coloured by the normalized vorticity. Lines in the simulations correspond to the director field. (a) Shear flow state, $\lambda/w \sim 1$, in the shear phase. (b) Shear flow state, $\lambda/w \sim 1$, in the instability phase. (c) Dancing state, $\lambda/w \sim 0.7$. *Scale bars:* 50 μm.

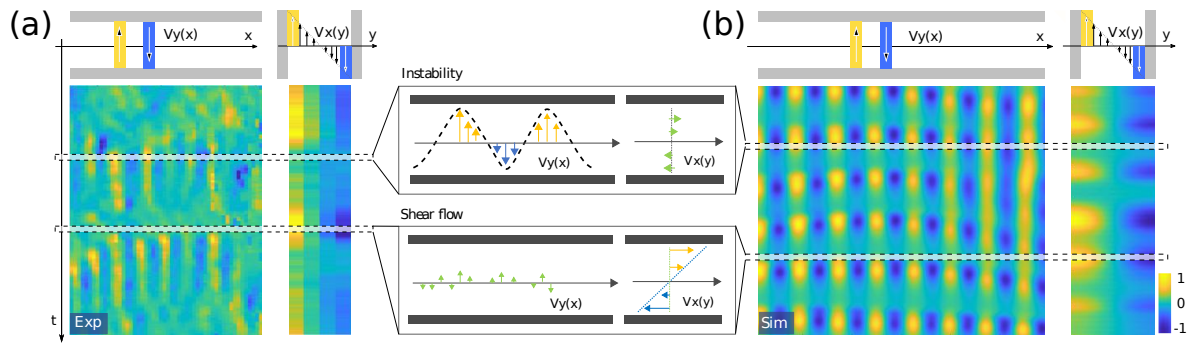


Figure 4.5: **Periodic instabilities in the shear state.** (a-b) Experimental kymographs for V_x averaged along the channel and V_y averaged across the channel are shown in (a) while the corresponding simulations appear in (b). The colour encodes the normalized velocity components. One instance of stable shear flow regime and one instance of transversal instability are sketched.

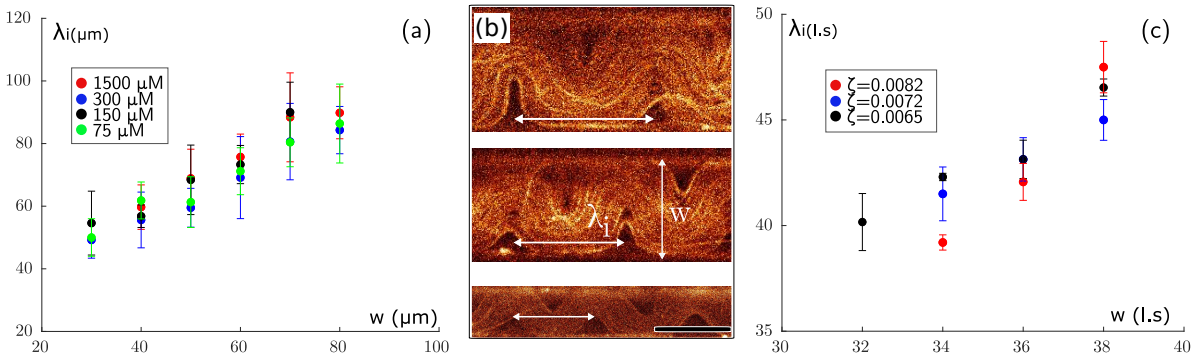


Figure 4.6: **Instability wavelength**. (a) Measurement of the instability wavelength λ_i *vs* w for different values of activity, controlled by the adenosine triphosphate concentration, whose values are displayed in the legend. (b) Fluorescent micrographs displaying the measurement of the instability wavelength λ_i at the onset of defect nucleation in the shear state for three different channels widths w. λ_i is taken as the distance between two neighbouring negative defects along a given wall, as indicated. *Scale bar:* 50μm. (c) λ_i *vs* w in simulations, for different values of activity as indicated. The unit of the axes is the number of lattice sites (l.s). In (a), error bars correspond to the standard deviation of the measurements for about 10 independent instability onsets per channel. In (c) error bars correspond to the standard deviation of the measurements.

4.5 The dancing state: a one-dimensional line of flow vortices

Increasing the channel width to values between 45 and 90 lattice-sites ($90\mu m$ and $120\mu m$), one-dimensional arrays of vortices are observed as shown in Fig. 4.4 (c). A close look at the defect distribution reveals that the transition to the flow state with organised vorticity arrays corresponds to the point when the channel can accommodate more than one defect in its cross-section, *i.e.*, $\lambda/w < 1$ (Fig. 4.3). One could expect that this criterion is reached when the channel width becomes comparable to the active length-scale. However as shown in Fig. 4.3, l_a/w is still much larger than 1 in the range of the dancing state, *i.e.*, $\lambda \ll l_a$. Furthermore, contrary to the l_a/w curves, λ/w does not seem to depend on activity, supporting the idea that λ is indeed a pure geometrical feature. Dynamically, the system behaves as if two distinct populations of positive defects are travelling along the channel in opposite directions, passing around each other in a sinusoidal-like motion. A similar state had been predicted by simulations and was referred to as the dancing state [20]. The dancing state observed in the experiments is quite fragile, and vortex lattices are always transient and localised in space, contrary to the published simulations. Defects may annihilate with their negative counterparts, or even switch their direction of motion, thus perturbing the flow pattern.

The difference between the spatial organisation of oppositely charged defects in the confined active nematic is manifest in their arrangement across the width of the channel (Fig. 4.7 (b)). The distribution of the $+1/2$ defects has a single peak at the centre of the channel (Fig. 4.7 (b), green). On the other hand, the $-1/2$ defect distribution has two peaks, one at each of the boundary walls (Fig. 4.7(b), blue) and the profiles do not rescale with the channel width (Fig. 4.7 (c)). Instead, the wall-peak distance is approximately constant at a separation ~ 3 lattice-sites ($\sim 18\mu$m) from the wall. In comparison with the experiments, the -1/2 defects in simulations were more strongly localised near the walls, and the $+1/2$ defects tended to lie towards the centre of the channel. This can be attributed to $-1/2$ defects having no self-propulsion and thus interacting elastically with the channel walls [81]. The distance of the $-1/2$ defect from the walls is therefore expected to be controlled by the intrinsic anchoring penetration length of the nematic $l_{\mathrm{n}} = K/\mathcal{W}$, which is set by the competition between the orientational elastic constant K and the strength of the anchoring at the wall $\mathcal{W}$, and is independent of the channel

width and activity of the particles. As expected, for wider channels, $w > 90$ lattice-sites ($w > 120\mu$m), the distribution of the $+1/2$ defects becomes more uniform as active turbulence is established.

Simulations have also allowed us to pinpoint the necessary boundary conditions at the channel walls to trigger defect nucleation. We find that such a localised defect formation at the walls is obtained only for free-slip boundary conditions for the velocity, and weak planar anchoring boundary conditions for the nematic director field. This is because the free-slip velocity, together with the parallel anchoring of the director, allows for strong tangential active flows, and hence strong tangential nematic order, to develop along the boundaries. This results in bend instabilities that grow perpendicular to the walls with the weak strength of the anchoring allowing the director to deviate from a planar configuration at the positions where the bend instability is developed. Previous simulations that assumed no-slip velocity and strong alignment conditions on the confinement did not observe defect nucleation at the boundaries [20, 82], and showed insensitivity of the active nematic patterns to the boundary conditions [82]. This is because the strong anchoring used in these works prevented defects from forming at the walls.

It is, however, interesting to note that a recent computational study, based on a kinetic approach, has reported a special case of defect nucleation at the boundaries of an active nematic confined within a circular geometry with no-slip velocity boundary condition and free anchoring [83]. However, in that work the wall-bound defect nucleation was observed only for confining disks of small sizes and had a very different dynamics than that reported here: the $+1$ defect imposed by the circular geometry was first dissociated into two $+1/2$ defects and then, for sufficiently small confinement one of the $+1/2$ defects kept moving into and out of the boundary. This is in contrast to our results that show regularly-spaced defect pair nucleation sites at the boundaries for a range of channel widths. Moreover, we find that the corresponding defect spacing is governed by an instability wavelength that is no longer given by the conventional active length scale.

4.6 Conclusion

We have presented continuum simulations, supported by experimental results, investigating the flow and defect configurations of an active nematic confined to rectangular channels of varying width. The simulations have identified a new dynamical state, where

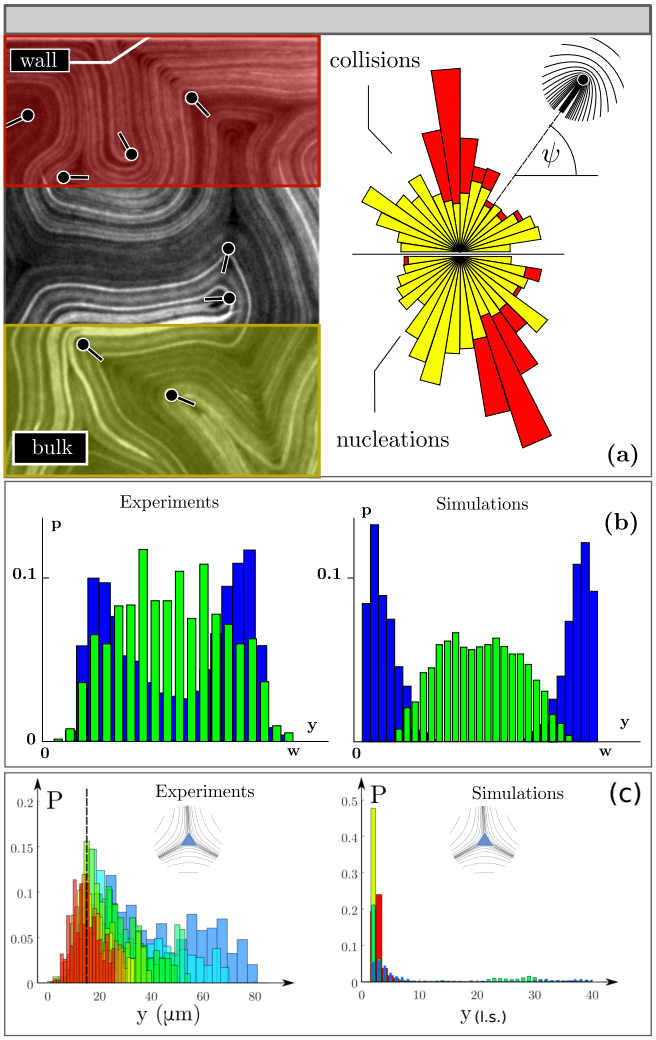


Figure 4.7: **Defect nucleation.** (a) Statistical distribution of positive defect orientations. The angle ψ corresponds to the orientation of the defect with respect to the wall. $\psi = \pi/2$ (resp. $\psi = 3\pi/2$) corresponds to a defect perpendicularly colliding with (resp. moving away from) the wall. The red distribution is the result of defects close to the wall, while the yellow distribution refers to bulk defects. (b) Experimental (left) and simulated (right) probability distributions of defect position across a channel. Green (blue) distribution refers to positive (negative) defects. (c) Distributions of negative defects positions for multiple values of channel width in experiments and simulations respectively. The peak of the distribution is at the same distance, estimated around 15μm for experiments and ~ 3 lattice-sites for simulations.

well-defined shear flow alternates in a regular way with bursts of instability characterised by $+1/2$ topological defects moving across the channel. We have also shown that, for wider channels, it is possible to identify the dancing state [20], although in experiments the particular boundary conditions considered made it less stable.

Our work highlights the importance of topological defects in controlling the confined flows. Because of the weak planar anchoring and the shear flow, pairs of $\pm 1/2$ defects form at the walls of the channel. The $+1/2$ defects are self-propelled and move away from the walls whereas the $-1/2$ defects remain close to the boundaries. The distance to the boundaries is set by the anchoring penetration length. In bulk active nematics the defect spacing is set by the active length scale and, although there is some evidence of long-range ordering [84–86], defect motion is primarily chaotic. In confinement, however, the defect spacing and the wavelength of the instability are set by the channel width and the defect trajectories are more structured.

Together, simulations and experiments demonstrate surprisingly rich topological defect dynamics in active nematics under channel confinement and sensitive dependence on both channel width and boundary conditions. Therefore, confinement provides a way of controlling active turbulence and defect trajectories, a pre-requisite for using active systems in microfluidic devices.

Chapter 5

Collective Chemotaxis of Active Nematic Droplets

In this chapter, we present the work done on modelling collective chemotaxis within an active nematic framework. We model a cell cluster as a biphasic active nematic droplet, by coupling the active nematic continuum equations to a Cahn-Hillard model. The chemical field, which diffuses from a source and is consumed by the cluster, regulates the activity of the droplet. We show that cell clusters move up a chemical gradient, and argue that the mechanism driving the chemotactic response is the activity-driven alignment of cells on the cluster boundary. We also show that the model reproduces experimental results. By doing this we demonstrate and explain how a physical mechanism that results in collective chemotaxis, arises from within an active nematic framework. This work has been published in Physical Review E [87].

5.1 Introduction

Chemotaxis denotes the movement of a single motile cell in the direction of an increasing or decreasing chemical gradient. It is one of the main mechanisms that provide cells with a sense of direction in a complex environment. There is now considerable evidence that aggregates of cells can also chemotax, a phenomenon termed collective chemotaxis [23, 27, 88–90]. For example, lymphoid, endothelial, glial and neural crest cells have all been shown to move collectively along chemical concentration gradients [22, 24, 26, 91]. Collective chemotaxis plays a key role in the navigation of cell clusters in e.g. embryogenesis and cancer metastasis [27, 92]. Surprisingly, the behaviour of chemotaxing clusters can be distinct from single-cell chemotaxis. Experiments have demonstrated that clusters of cells can chemotax as a collective, regardless of whether the constituent cells are capable [22, 26] or incapable [27] of responding to a chemical gradient.

Moreover, there is strong evidence for the importance of cell-cell junctions [27, 89].

This suggests that cluster chemotaxis is an emergent phenomenon, and agent-based numerical models have been used to suggest generic mechanisms. Examples include flocking models, particle-based models which couple chemokine gradients to contact inhibition of locomotion, and models which account for chemical signalling between cells [25, 93–95].

Motivated by previous models which interpret the dynamics of cell colonies in terms of the properties of active nematics [96, 123], we model collective chemotaxis as a biphasic active nematic liquid crystal. We then couple the active nematic phase to a chemical field that regulates the activity. The next section outlines the details of this model.

5.2 Model

To model collective chemotaxis we use a continuum approach, as outlined in chapter 3, and describe the cell colony as a two-dimensional active nematic [10]. The governing hydrodynamic equations couple four variables; $\mathbf{Q}$ and $\mathbf{u}$ which describe the local nematic order and velocity of the cells, the cell concentration, ϕ, which allows the position of the colony to be tracked, and C, the concentration of the chemical field. To describe the dynamics of ϕ we first outline the theory we use to model biphasic liquid crystals.

In this thesis, we take the approach of modelling a biphasic liquid crystal as a collection of two immiscible fluids, one being an isotropic fluid and the other a nematic liquid crystal. We define the relative concentration of the two fluids as a field ϕ. This field is implemented via the free energy term

$$\mathcal{F}_{sep.} = \frac{A_\phi}{2}(\phi)^2(1-\phi)^2 \tag{5.1}$$

where the parameter A_ϕ is positive. This free energy is minimised when ϕ phase separates into regions where $\phi = 0$ or $\phi = 1$. To ensure a smooth transition of ϕ between the two phases, we implement an interfacial free energy

$$\mathcal{F}_{\nabla\phi} = \frac{K_\phi}{2}(\nabla\phi)^2 \tag{5.2}$$

where K_ϕ is a positive coefficient. This free energy penalises gradients in the ϕ-field, and represents the surface tension that stabilises the interface between the two phases. Together, the free energy terms in eqn 5.1 and eqn 5.2 cause the ϕ-field to completely phase separate into two phases set apart by a smooth interface.

One of the fluids is made nematic by coupling ϕ to the nematic order parameter S. This is motivated by the concentration dependence of S in lyotropic liquid crystals, which exhibit a nematic phase at high concentrations and an isotropic phase at low concentrations. Given that $S = \frac{1}{2}tr(\mathbf{Q}^2)$ this is implemented by an additional free energy term

$$\mathcal{F}_{\phi S} = \frac{B}{2}(\phi - S)^2 \tag{5.3}$$

where B_ϕ is a positive coefficient. Hence, regions where $\phi = 1$ are nematic, and $\phi = 0$ isotropic. Together, these three free energy terms distinguish the region occupied by the active nematic ($\phi = 1$) and the surrounding isotropic fluid ($\phi = 0$), and are separated by a smooth interface.

This concentration field ϕ evolves according to the Cahn-Hillard equation [97]

$$(\partial_t + u \cdot \nabla)\phi = \Gamma_\phi \nabla^2 \mu \tag{5.4}$$

where Γ_ϕ is a mobility and μ is a chemical potential given by

$$\mu = \frac{\partial \mathcal{F}}{\partial \phi} - \partial_i(\frac{\partial \mathcal{F}}{\partial(\partial_i \phi)}). \tag{5.5}$$

In principle, the mobility can depend on ϕ (for example in miscible fluids $\Gamma_\phi = \Gamma_0\phi(1-\phi)$, for some constant Γ_0) but since this thesis deals with immiscible phase-separated fluids we take Γ_ϕ to be a constant [98]. The Laplacian of the chemical potential conserves the values of ϕ. This is important because we require the amount of liquid crystal in our system to remain constant due to mass conservation.

The total free energy of this system is given by,

$$\mathcal{F} = A_\phi \left(\phi\right)^2 \left(1 - \phi\right)^2 + K_\phi \left(\nabla\phi\right)^2 + B(\phi - S^2)^2 + K \left(\nabla \mathbf{Q}\right)^2. \tag{5.6}$$

which is the sum of the $\mathcal{F}_{sep.}$ (eqn. 5.1), $\mathcal{F}_{\nabla\phi}$ (eqn. 5.2), $\mathcal{F}_{\phi S}$ (eqn. 5.3), terms discussed above, and the $\mathcal{F}_{\nabla Q}$ (eqn. 2.10) term discussed in section 2.3.

The dynamics of the $\mathbf{Q}$-tensor is governed by the Beris-Edwards equation (eqn. 2.13) presented in section 2.5. We assume that both phases can be modelled as incompressible fluids of density ρ. The fluid velocity $\mathbf{u}$ obeys the Navier-Stokes eqn. 2.16 and eqn. 2.17. The stress tensor is the same as eqn. 2.18, except there is an additional capillary stress

Π^{cap} to account for the boundary between the two regions of ϕ, and a different active stress Π^{act} than the one given in eqn. 3.4. The capillary stress is given by,

$$\mathbf{\Pi}^{cap} = (\mathcal{F} - \mu\phi)\mathbf{I} - \nabla\phi(\frac{\delta\mathcal{F}}{\delta\nabla\phi}) \tag{5.7}$$

and the first term accounts for the capillary pressure, while the second term accounts for gradients in the concentration field ϕ. Initially, we assume that the cells and surrounding fluid phase have the same viscosity, although we do confirm that changing the viscosity of the isotropic fluid only acts to slow the cluster and does not change the underlying dynamics.

The active stress is coupled to the chemical concentration C through a simple linear weighting,

$$\mathbf{\Pi}^{active} = -\zeta C\phi\mathbf{Q}, \tag{5.8}$$

which is non-zero only within the cell colony. To couple the chemoattractant to the colony dynamics we assume that the active stress is proportional to the local concentration of the chemical field, C. In what follows we shall refer to ζ, which is constant in space and time, as the activity and $\zeta C\phi S$, which varies within the colony and in time, as the active stress.

Lastly, we write down a convection-diffusion equation for C:

$$\partial_t C + \boldsymbol{\nabla}\cdot(\boldsymbol{u}C) = \Gamma_C\boldsymbol{\nabla}^2 C - \alpha_C C\Theta(\phi - 0.6), \tag{5.9}$$

where Γ_C is the diffusion coefficient of the chemical field. The final term in eqn. 5.9 describes depletion of the chemical at a rate controlled by α_C. $\Theta(x)$ is a step function, equal to zero for $x \leq 0$ and unity for $x > 0$ which ensures that depletion is restricted to within the cell layer. This equation is solved using the same finite-difference method as discussed in the appendix section A.2.

The equations were solved on a lattice of size 260 in the x-direction by 300 in the y-direction (Fig. 5.1). A circular cluster of cells with $\phi = 1$ was initialised near the centre of the simulation box. The components of $\mathbf{Q}$ were initialised randomly and $\mathbf{u}$ was set to zero. Neumann boundary conditions were chosen for the ϕ-field and $\mathbf{Q}$ tensor, and free-slip boundary conditions were selected for the velocity field. However, these are unimportant because the fluid at the walls is isotropic and passive and any velocities near the walls are insignificant. The chemical concentration field C was set to zero

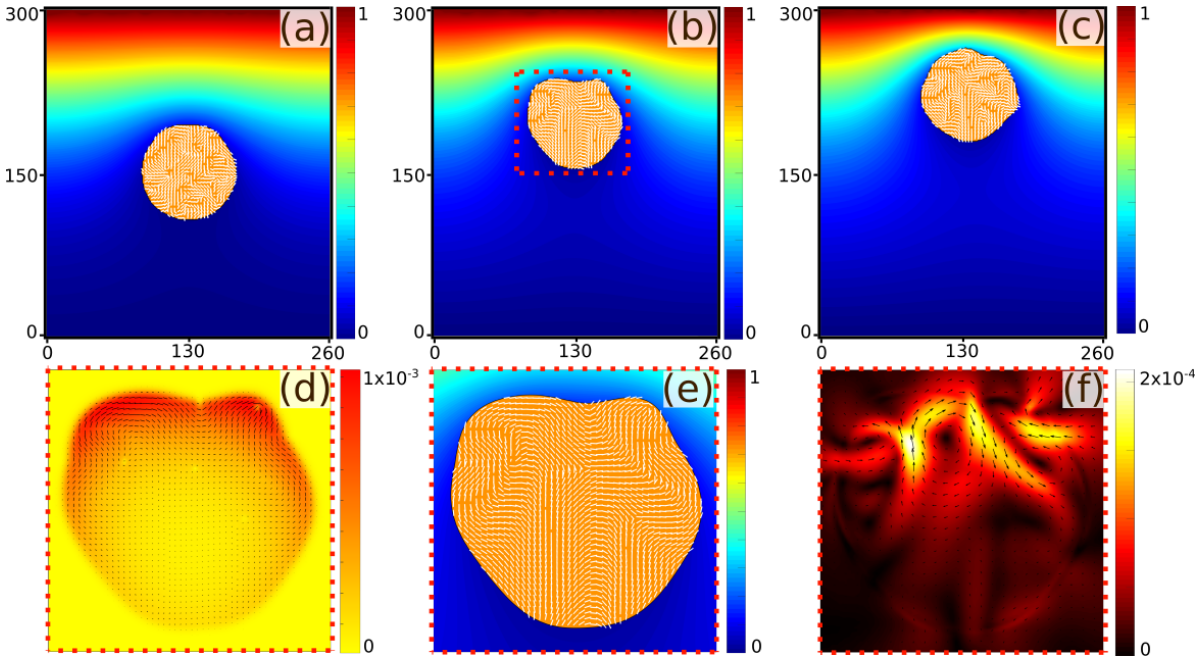


Figure 5.1: Snapshots of the active colony at time-steps (a) 250,000 (b) 1,000,000 (c) 2,000,000. The colony is depicted in orange, with the corresponding director field **n** shown by the white dashes. The underlying colourmap represents the chemical concentration. (d)-(f) Magnified view of the section of the box outlined by red dashes in (b): (d) Coefficient of the active stress $\zeta C\phi S$. (e) Director field **n** inside the colony. (f) Magnitude of the velocity field, with the flow direction shown by the black arrows.

everywhere except along $y = 300$ where it was set to 1. It was allowed to diffuse out of the box at $y = 1$, for all x by setting the value of the field at the wall nodes such that the gradients at a wall node and its nearest neighbour were equal. Reflection boundary conditions were used for C at $x = 0$ and $x = 260$. The simulations were run for an initial 150,000 time steps after which the initialisation dynamics had relaxed, the colony had radius r, and the chemical field was in dynamic equilibrium. Data for the active colony was then collected for 2,000,000 timesteps.

The parameters used are $\Gamma_Q = 0.3$, $\Gamma_\phi = 0.2$, $\Gamma_C = 0.15$, $A_\phi = 0.1$, $B = 0.001$, $K_\phi = 0.1$, $K = 0.0005$, $\alpha_C = 0.001$, $\lambda = 0.3$, $\rho = 40$, $\eta = \frac{1}{6}$. The control parameters in the simulations are the cluster radius r which takes values from 27 to 71 lattice sites and the activity ζ which varies from -0.02 to 0.02.

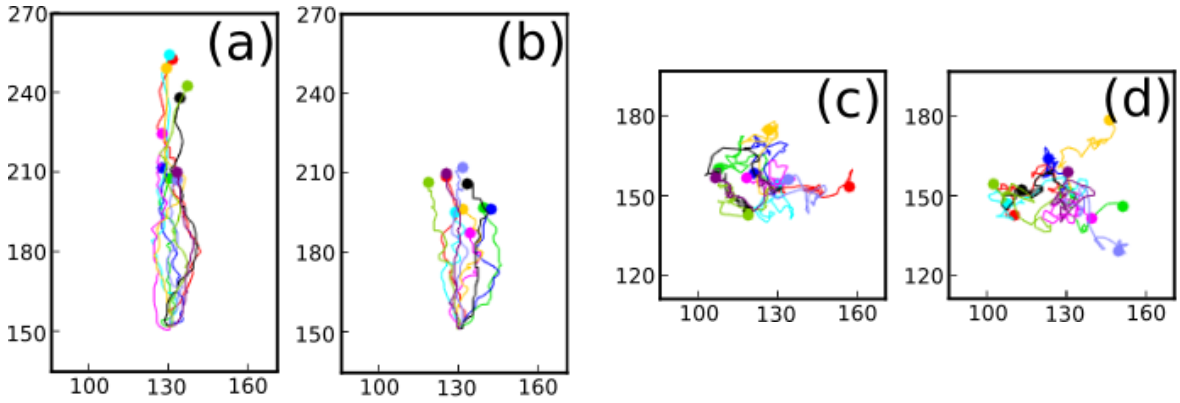


Figure 5.2: Trajectories of the cluster centre-of-mass, for (a) $\zeta = 0.008$ (b) $\zeta = -0.008$ in a chemical field gradient. (c) $\zeta = 0.001$ (d) $\zeta = -0.001$ in a static homogenous chemical field. The values of ζ are adjusted in (c), (d) compared to (a), (b) to allow for the higher concentration of chemoattractant in the latter case.

5.3 Trajectories of Chemotactic Clusters

The dynamics of a cluster with radius $r = 45$ and $\zeta = 0.008$ is illustrated in Fig. 5.1. Panels (a), (b) and (c) correspond to snapshots at times 250,000, 1,000,000 and 2,000,000 respectively, with the underlying colourmap showing the chemical concentration field. The cell colony is clearly moving in the direction of increasing concentration. Figs. 5.1(d)–(f) enlarge the area outlined in red in panel (b). The active stress, $\zeta C\phi S$, is plotted in Fig. 5.1(d) indicating that it is only significant at the top of the cluster, differing by an order of magnitude between the top and bottom because of the adsorption of the chemoattractant by the cells. The director field $\mathbf{n}$ can be seen more clearly in subfigure (e). Finally, a snapshot of the magnitude and direction of the flow field is presented in Fig. 5.1(f). Note that the net motion towards the chemical source persists despite the apparent chaotic nature of the flows.

The trajectories of the centre-of-mass of the colony, for 10 different initial conditions, are compared in Fig. 5.2(a) (Fig. 5.2(b)) for an extensile (contractile) active nematic, with $\zeta = 0.008$ ($\zeta = -0.008$). In all cases there is a net motion of the cells towards the chemical source, demonstrating that the colony is chemotactic for both extensile and contractile activity. For comparison we compare trajectories for the case where the chemical concentration is constant across the colony for extensile (Fig. 5.2(c)) and contractile (Fig. 5.2(d)) driving. Here the colony does not move in any preferred direction.

To quantify the efficiency of chemotaxis it is customary to use the chemotactic index, defined as the ratio of the displacement of the cluster centre-of-mass in the direction of the chemical source, y, to the total length of its trajectory. This varies from 0 for random motion to 1 for directed motion towards the chemical source. The chemotactic indices averaged over the trajectories in each frame of Fig. 5.2 are 0.84, 0.78, 0.0 and 0.03 for Figs. 5.2(a), (b), (c) and (d) respectively.

While the extensile and contractile colonies have similar chemotactic indexes, it is apparent from Fig. 5.2 that the extensile systems tend to move further than the contractile ones. The average rms velocity of the cluster centre-of-mass was 0.46×10^{-4} for the extensile active clusters compared to 0.37×10^{-4} for the contractile clusters (simulation units). This is a consequence of extensile active nematics generating stronger flows than contractile ones for the same value of the activity [99].

At this point, it is clear that the active colonies exhibit chemotaxis, but it is not obvious why this is the case. Next, we explain the physics underpinning this behaviour.

5.4 Results

The director field of an extensile active nematic preferentially aligns tangentially to the boundary of a colony, whereas that of a contractile system tends to align radially [55]. This effect, which has been termed active anchoring, as outlined in section 3.6, holds in the absence of any thermodynamic interface anchoring. Indeed radial cell polarization has been reported at the boundaries of cell colonies undergoing chemotaxis, suggesting that these systems can be described as contractile active nematics [22, 26, 27].

As described in section 3.6, the mechanism for active anchoring can be explained by considering the force density that arises from the active stress, $\nabla(-\zeta C\phi\mathbf{Q})$. It is important to note, however, that the force density in this work is different than that presented in [55], and results in additional contributions to the forces along the interface. Denoting the unit normal to the surface by $\mathbf{m}$, the force density is

$$\mathbf{F}^{active} = \zeta\{\sigma((\mathbf{m}\cdot\mathbf{n})\mathbf{n} - \frac{1}{2}\mathbf{m}) - SC\phi(\mathbf{n}(\nabla\cdot\mathbf{n}) + (\mathbf{n}\cdot\nabla)\mathbf{n})\} \tag{5.10}$$

where $\sigma = |\nabla S|\phi C + S|\nabla\phi|C - S\phi|\nabla C|$. Defining $\mathbf{l}$ as the unit-vector perpendicular to $\mathbf{m}$, the first term on the r.h.s. of eqn. 5.10, which dominates at the interface, leads to a force density acting along the colony surface $F_{||}^{active} = \zeta\sigma(\mathbf{m}\cdot\mathbf{n})(\mathbf{l}\cdot\mathbf{n})$. This force is zero only when the director $\mathbf{n}$ is normal or parallel to the surface. Otherwise it induces flows

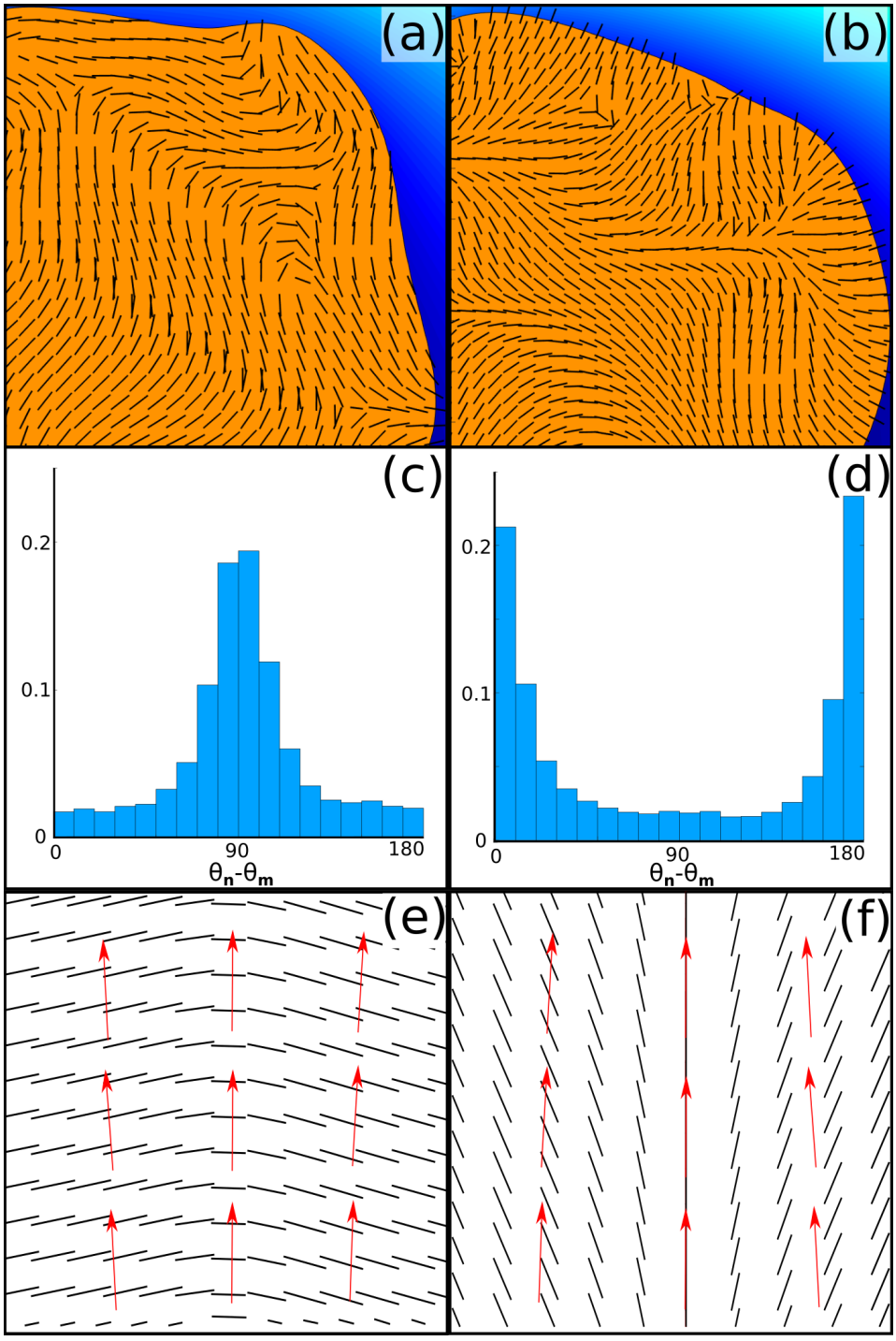


Figure 5.3: Active alignment of the director at the surface of an active cluster: (a) extensile activity which results in parallel alignment, (b) contractile activity leading to normal alignment. Time-averaged, normalised histogram of the angle between the director and the surface normal, $\theta_n - \theta_m$ for (c) extensile activity, $\zeta = 0.008$, (d) contractile activity, $\zeta = -0.008$. Schematic illustration of the flow field (red arrows) resulting from (e) a bend distortion in the director field of an extensile active nematic, (f) a splay distortion in the director field of a contractile active nematic.

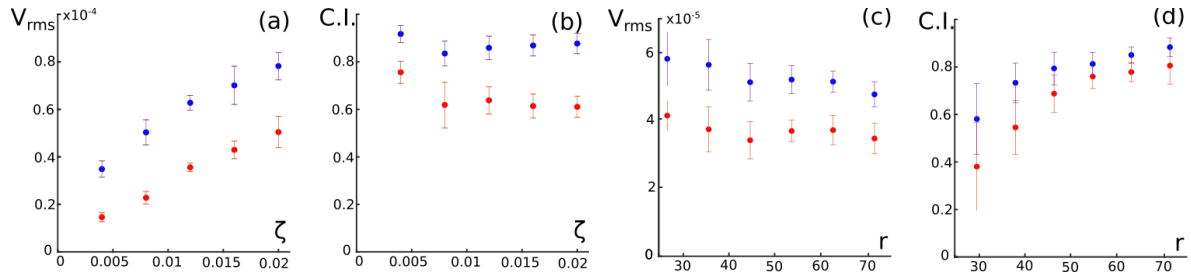


Figure 5.4: (a) Root mean square velocity V_{rms} of the cluster centre-of-mass as a function of activity, ζ. (b) Chemotactic index, C.I., as a function of ζ. (c) V_{rms} as a function of cluster radius r. (d) C.I. as a function of r. Blue (red) symbols denote extensile (contractile) activity.

which realign $\mathbf{n}$ tangentially or radially for extensile or contractile clusters respectively [55].

Fig. 5.3(a)-(d) illustrates the active anchoring. Panel (a) is a snapshot showing that the director field of an extensile cluster tends to lie parallel to the surface. Panel (b) contrasts a contractile system where the director prefers to lie normal to the surface. To quantify the active anchoring Fig. 5.3(c) and (d) shows the corresponding normalised, time-averaged histogram of the angle between $\mathbf{n}$ and $\mathbf{m}$.

The surface anchoring propagates into the bulk because of elastic forces. This means that the distortions near the interface are preferentially bend-like in extensile systems and splay-like in contractile ones. In both cases this results in outwards radial flow (Fig. 5.3(e) and (f)). Since the concentration of the chemoattractant is higher, and hence the active stress larger, in the part of the colony closest to the chemical source, the outward flows will be stronger there giving the imbalance that moves the colony up the chemical gradient. (These flows dominate those which arise from the σ-term in eqn. 5.10, which are directed inwards and so would act to make the cluster chemorepulsive.)

We next discuss the quantitative results. Fig. 5.4(a) plots the rms velocity V_{rms} of the centre of mass of a cluster of radius $r = 60$ against the activity for both contractile and extensile clusters. The cluster position is measured at intervals of 5×10^4 timesteps, and each data point is the result of averaging over ten independent simulations. Fig. 5.4(b) shows that the chemotactic index is approximately independent of the activity, and close to unity, indicating that the flows are well-aligned by the active anchoring.

Given we take a continuum approach our model is relevant to large, well-connected

clusters. Experiments using malignant lymphocyte cells [22] have shown that sufficiently large clusters chemotax with a velocity independent of their area in agreement with the dependence found here. However, the experimental situation is far from clear. In [22] chemotaxis is seen only above a threshold size of 20 cells and in [27] neural crest cells are shown to chemotax even if they only have transient contact with their neighbours.

The chemotactic index, however, increases with cluster size but levels off as the cluster radius increases (Fig. 5.4(d)). This is because the flows in the smaller clusters show larger fluctuations. In particular, the smallest clusters undergo obvious periods of rotation. This rotational motion can be explained by noting the tendency of the activity to drive flow vortices at a length scale commensurate with the size of these clusters [20, 48]. Similar behaviour has been observed for small clusters of lymphoid cells [22] allowing a mapping between simulation and physical parameters. In the experiments clusters with radius $\approx 30\mu m$ undergo periods of rotation for about 60 seconds. In the simulations, the corresponding values are 40 lattice units and 10^5 time steps. This maps the simulation value $V_{rms} \approx 10^{-4}$ in lattice units on to $V_{rms} \approx 10^{-1}\mu m\, min^{-1}$ in physical units which is in agreement with typical chemotactic velocities measured in experiments [22, 27, 91].

5.5 Conclusion

Several mechanisms that can lead to collective chemotaxis have been proposed in the literature. These include chemical or mechanical interactions between cells initiated by a chemical gradient [90, 94], a coupling between contact inhibition of locomotion and a chemoattractant [25], and the existence of leader cells at the cluster rim that have a strong chemotactic response [22]. Here we show that interpreting a cell cluster as an active nematic leads naturally to collective chemotaxis. Active stresses give a net alignment of cells on the cluster surface, and the alignment propagates into the bulk resulting in stresses which drive flows directed outwards. If the strength of the activity depends on the local chemoattractant concentration, a chemical gradient results in unbalanced forces and hence motion up the gradient. Radial polarisation of cells at an interface has been observed in experiments, and the model explains this as arising from the contractile forces exerted by the cells [22, 26, 27, 88, 91, 100]. Moreover, the model reproduces the experimental observation that the net speed of chemotaxing clusters is independent of their size. This explanation of collective chemotaxis could be

tested further by studying the shapes of cells in a chemotaxing cluster in more detail, by investigating the flow fields in the clusters, and by measuring the dependence of the chemotactic index and cluster speed on the magnitude of the active stress, which can be varied by changing the concentration of the chemoattractant.

Chapter 6

Multi-Phase Field Model

Understanding the physics of collective motion in biological systems often requires using a theory that models individual cells, rather than their coarse-grained aggregate. This is because it can be unclear how to incorporate important biological details, like cell-cell adhesion, and biological mechanisms, like contact-inhibition-of-locomotion, into continuum theories. There are many cell-based theories that model collections of individual cells, but the one used in this thesis is known as the multi-phase field model. This approach involves simulating a collection of phases, where each phase represents a unique cell. The aim is to place passive and active forces on the phases to recover realistic dynamics.

Since the multi-phase field model simulates individual cells, it is useful to understand the dynamics and biophysical properties of cells and clusters. The purpose of this chapter is to provide such details, and to introduce the theory behind the multi-phase field model.

This chapter is outlined as follows. Section 6.1 describes relevant biological mechanisms at both the single-cell and cluster level, such as the properties of a cell's cytoskeletal filaments, contact-inhibition-of-locomotion, and the forces present in certain cell monolayers. Section 6.2 describes some of the popular physical models associated with modelling cell monolayers. Section 6.3 introduces the multi-phase field model which we use in chapter 7.

6.1 Eukaryotic cell dynamics

The cytoskeleton gives a cell its mechanical properties, such as its shape and ability to resist deformations [101]. It consists of a dynamic network of interlinking protein filaments that connect the cell nucleus to the cell membrane. Filaments are composed

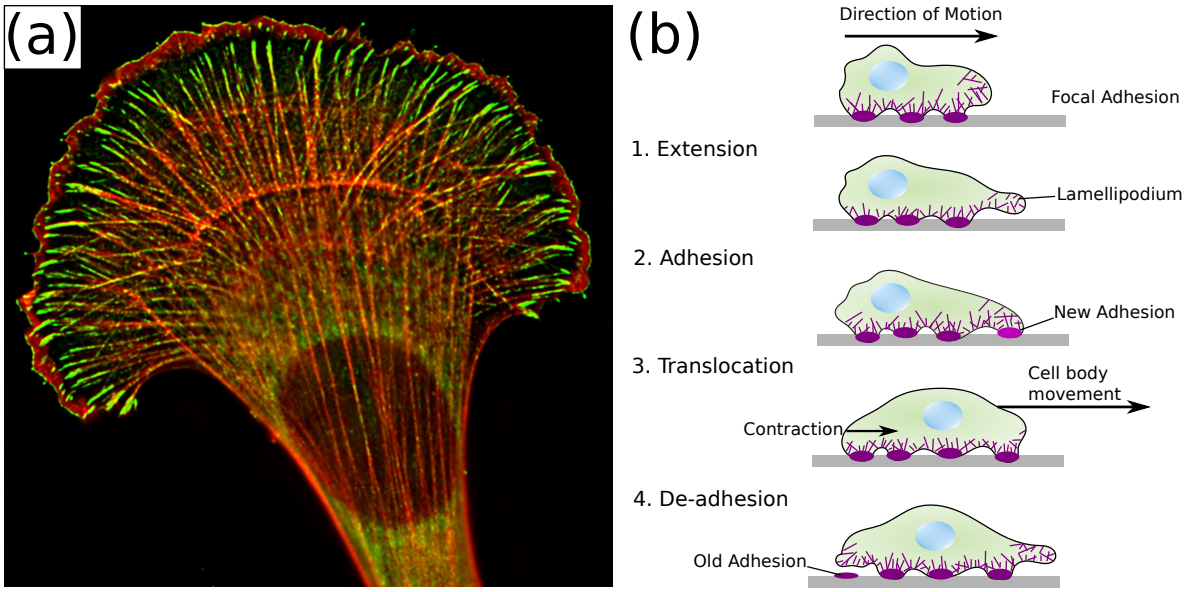


Figure 6.1: (a) The lamellipodium of a fibroblast cell with the F-Actin stained red, and VASP protein stained green [102]. (b) Schematic of the treadmilling process. First, the cell extends a protrusion in a given direction, adheres to the substrate and then contracts. This shifts the centre-of-mass towards the direction of the initial protrusion. The adhesion complex at the receding end then de-attaches and the process repeats.

of one of three main components, actin (also known as microfilaments), intermediate filaments, or microtubules. Images of the cytoskeletal network can be captured using immunofluorescence, an example of which is shown in Fig. 6.2(a) which highlights the actin filaments (red) inside a fibroblast cell. The ruffled protrusion is known as a lamellipodium.

Actin filaments and their associated molecular motors myosin are known as the actomyosin network and underlie important cell properties such as cell migration and cell shape [101]. Single-cell migration arises from a four-step process known as treadmilling [103], depicted in Fig. 6.2 (b). The cell attaches to the substrate through mechanical links, known as focal adhesions. The actin network then preferentially polymerises on one side of the cell which generates the lamellipodium. This protrusion then attaches to the surface through a new focal adhesion. The cytoskeleton contracts which moves the cell's centre-of-mass towards the direction of the lamellipodium. The focal adhesion on the receding end then detaches from the surface, and the process repeats. This allows a cell to freely migrate across an open substrate and motivates the polarisation forces

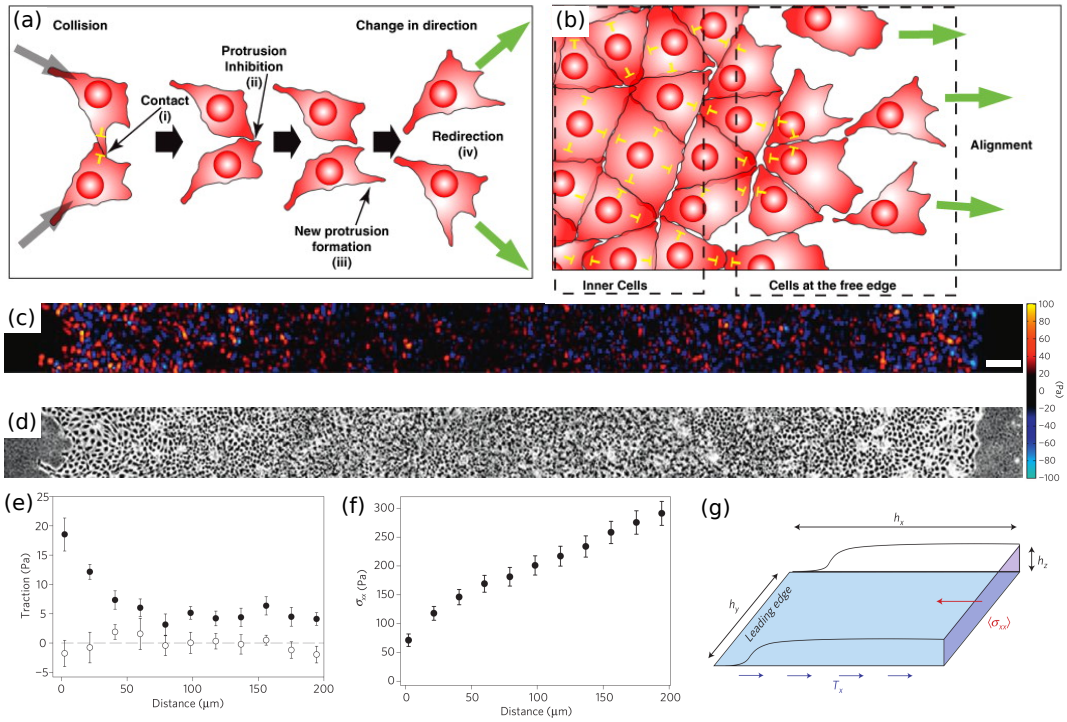


Figure 6.2: **Contact-inhibition-of-locomotion, and cell monolayer forces**. (a) CIL in isolated cells results in the collapse of cell protrusions (yellow arrows) at the location of cell-cell contact, and a change in the direction of migration (green arrows). (b) CIL in cell monolayers results in the inhibition of protrusions for cells deep in the bulk (inner cells), while cells at the free edge can lead to cell polarization, and for some systems migration away from the bulk (green arrows). Both (a) and (b) were adapted from [104]. (c) The radial component of the tractions along a diameter of the expanding cell colony (scale bar = 200μm) (d) Phase contrast image of the monolayer. (e) The average normal traction (filled circles) and the average parallel traction (open symbols). (f) The average stress within the cell sheet. Error bars indicate the standard error of the mean. (g) Schematic of the traction force and average stress $\langle \sigma_{xx} \rangle$ along the leading edge of the cluster. (c)-(g) were adapted from [105].

typically placed on cells in physical models.

An interesting biological property of freely migrating cells is that they move away from each other after they come into contact. This mechanism is known as contact-inhibition-of-locomotion [104], and it was first observed by Abercrombie and Heaysman in the 1950s when they noticed that the migration direction of fibroblast cells was af-

fected by cell-cell contact [106]. For example, when two freely migrating cells come into contact, their lamellipodia recede at the location of cell-cell contact, and re-form along a free edge. This redirection of the lamellipodia results in the cells migrating away from each other. This process is depicted in Fig. 6.2 (a). From a modelling perspective, this can be implemented by making the polarization direction of each cell orient away from the location of neighbouring cells.

Contact-inhibition-of-locomotion (CIL) can result in stable protrusion formation at the boundary of a cell monolayer. The lamellipodia of cells on the free edge are stable and orient away from the bulk. It is worth noting that the long-lived protrusions at the free edge play an important role in collective chemotaxis as they provide directional cues to the cluster [22, 27]. Deep inside the bulk, however, the cells are not able to form stable lamellipodia given they have no free edge, although cryptic protrusions have been observed between some cells [107–109]. This process is shown in Fig. 6.2 (b), where CIL is represented by the yellow inhibitory markers.

Cells at the free edge of a monolayer exert significant traction forces compared to those deep inside the bulk. In an experiment by Trepat et al. [105], the traction force of a quasi-two-dimensional Madin–Darby canine kidney epithelial cell sheet was measured at each point along the substrate, as shown in Fig. 6.2 (c). The phase-contrast image is shown in 6.2 (d). The traction force was then measured as a function of the distance to the monolayer boundary, as shown in Fig. 6.2 (e). It was found that the traction force normal to the interface is largest along the boundary of the monolayer, and weakens significantly deep inside the monolayer (although it does not go to zero). Halfway inside the sheet, the normal traction force changes sign and increases until it reaches the other free edge. The traction forces at the boundary result in a global tensile stress across the monolayer. This is quantified by measuring the average stress σ_{xx}, normal to a plane perpendicular to the substrate and parallel to the leading edge, as given in 6.2 (g).

The formation of stable protrusions along the free edge of a cell cluster is also found to play an important role in wound healing experiments of epithelial monolayers. These experiments aim to understand how cell monolayers heal when damaged, for example, if part of the cluster is artificially scratched. A nice example [110] of an experimental setup used to investigate would healing involves growing cells to confluence around a

pillar, which is then removed, leaving a hole in the cluster. These experiments allow for a cleaner study of wound healing than scratch-based experiments since they do not damage the cells at the location of the wound, which results in additional mechanisms that contribute to healing.

In [110], detaching pillars of size 20μm or larger causes the cells to form lamellipodia, and therefore crawl, in the direction of free space such that the gap area decreases linearly in time. Below 20μm, a different mechanism drives the dynamics, speculated to be driven by the balance between cell-substrate adhesion, and cortical tension. The active migration of cells at the boundary is also consistent with experiments on expanding MDCK epithelial monolayers [107]. Along the monolayer boundary, the outer cells form lamellipodia, and migrate, towards free space. They pull the inner cells along, resulting in the net expansion of the monolayer.

To understand the physical mechanisms that underlie these processes, one first needs to define a physical model. Many such models exist, and we describe some of the popular approaches in the next two sections.

6.2 Models of collective cell motion

Various physical models have been created to study the dynamics of cell monolayers [28]. One popular approach is to model cells as hard-disks, and drive their motion through polar forces. Some choices to determine the orientation of these polar forces are to make it follow a random walk, orient away from neighbouring cells (as motivated through contact-inhibition-of-locomotion), or align it in the direction of the cell motion. Recently it was shown that a hard-disk approach [28], with polarisation determined through a combination of noise and contact-inhibition-of-locomotion, gives rise to a variety of states, ranging from a crystallized state, polar liquid and even cell aggregates. The phase diagram and snapshots of each state are given in Fig. 6.3 (a). The particular state of the system is determined by the rate at which the polarisation realigns to the velocity (relative to the noise), ψ, and the strength of cell-cell adhesion $\bar{W}_c$.

Another popular class of models, known as active network models, describe a confluent cell layer as a network of polygonal cells, as depicted in Fig. 6.3 (b). The motion of the polygons is driven by placing a polarisation force on either the centre of the cells

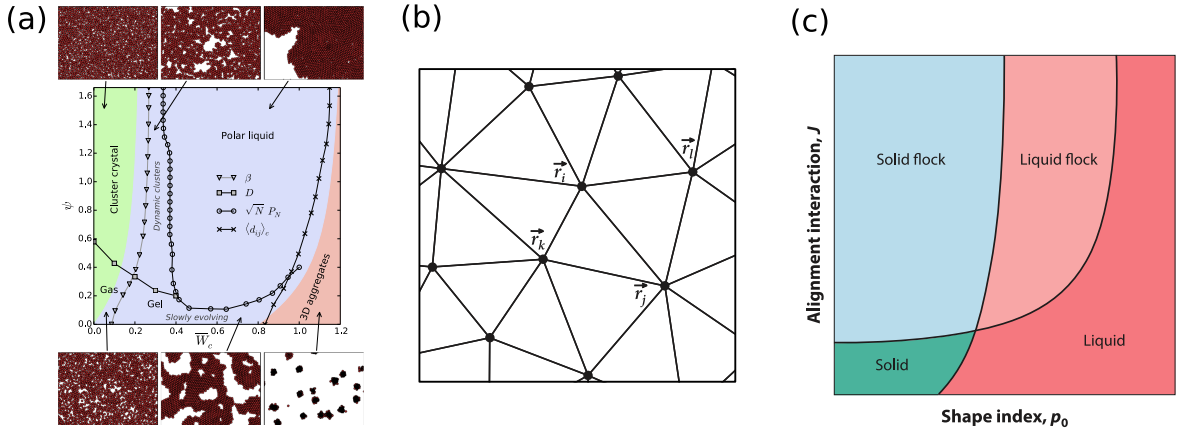


Figure 6.3: (a) Phase diagram from a hard-disk model, with snapshots of the corresponding states [28]. (b) Schematic of a vertex model with a subset of vertices denoted by r_i. (c) The phase diagram arises from a Voronoi model with polarisation aligned to the velocity. (b) and (c) are adapted from [28].

(in which case it is called a Voronoi model) or the vertices (in which case it is called a vertex model). The choice in determining the orientation of the polar forces is similar to the particle-based models described above. Voronoi models which align the polarisation to the velocity of the cell, recover a variety of phases including solid and liquid states (characterised by very-little or significant cell-cell rearrangement respectively), along with solid-flocking and fluid-flocking states (characterised by the large-scale alignment of the polarization). The particular state of the system is determined by the rate at which the polarisation aligns to the cell velocity, $J = \tau^{-1}$, and the shape index of the cell, defined to be the ratio of the cell perimeter to the cell area at equilibrium, p_0. The phase diagram for this particular model is shown in Fig. 6.3 (c).

Yet another popular class of models are known as multi-phase field models, which is an extention of the Cahn-Hillard model introduced in chapter 5 to include multiple cells. This model provides some benefits over using hard-disk and network models, and is used in the work presented in chapter 7. Before discussing it in detail, we outline some of the benefits it provides over the models discussed above.

The main benefit of the multi-phase model is that membrane of each cell is continuously deformable, unlike in hard-disk and active network models. This is important because cell deformation plays an important role in the dynamics of confluent cell layers,

for example, regulating whether the monolayer is in a liquid-like or solid-like state [111, 112].

Another benefit of the phase-field approach is that forces can be modelled in more nuanced ways, since forces act at points in hard-disk and active network models, while they act over an area in multi-phase field models. For example, a polar force can be placed on one side of the cell, allowing for a more detailed model of cell treadmilling with one side of the cell migrating, and the other trailing behind. This could be used to investigate the role of cell stiffness in single-cell migration. Further, forces could be made to depend on the local curvature or elongation of the cell membrane. For example, a contractile active force can be placed on the cells to prevent them from becoming too elongated.

In summary, the ability to model continuously deformable cells, and place complex forces on them, makes the multi-phase model a desirable choice to simulate collections of cells.

6.3 Multi-phase field model

The Cahn-Hillard model presented in section 5.2 described the phase separation of a single field into two phases, $\phi = 0$ and $\phi = 1$. This approach has also been extended to model single-cells [113–115], as well as collections of distinct cells, to investigate problems ranging from the migration of a few cells [116] to the dynamics of entire cell monolayers [117–119]. Using this approach, a collection of cells is modelled using multiple distinct fields ϕ_i, each representing a unique cell. These fields evolve according to

$$(\partial_t + \mathbf{v}_i \cdot \nabla)\phi_i = \Gamma_\phi \nabla^2 \mu_i \tag{6.1}$$

where $\mathbf{v}_i$ is the velocity of phase ϕ_i, and Γ_ϕ is a mobility, taken to be the same for all fields. The chemical potential of each phase μ_i is given by

$$\mu_i = \frac{\partial \mathcal{F}}{\partial \phi_i} - \partial_k \left(\frac{\partial \mathcal{F}}{\partial(\partial_k \phi_i)}\right). \tag{6.2}$$

The free energy $\mathcal{F}$ defines the equilibrium of the phases. We choose the total free energy to be given by $\mathcal{F} = \mathcal{F}_{\text{CH}} + \mathcal{F}_{\text{area}} + \mathcal{F}_{\text{rep.}} + \mathcal{F}_{\text{wall}} + \mathcal{F}_{\text{adh}}$ [29, 30, 120] where

$$
\begin{aligned}
\mathcal{F}_{\text{CH}} &= \sum_i \frac{\gamma}{\lambda} \int d\mathbf{x} \left\{ 4\phi_i^2(1-\phi_i)^2 + \lambda^2(\nabla\phi_i)^2 \right\}, \\
\mathcal{F}_{\text{area}} &= \sum_i \mu \left\{ 1 - \frac{1}{\pi R^2} \int d\mathbf{x}\, \phi_i^2 \right\}^2, \\
\mathcal{F}_{\text{adh}} &= \sum_i \sum_{j \neq i} \omega\lambda \int d\mathbf{x}\, \nabla\phi_i \cdot \nabla\phi_j, \\
\mathcal{F}_{\text{rep.}} &= \sum_i \sum_{j \neq i} \frac{\kappa}{\lambda} \int d\mathbf{x}\, \phi_i^2 \phi_j^2, \\
\mathcal{F}_{\text{wall}} &= \sum_i \frac{\kappa_{wall}}{\lambda} \int d\mathbf{x}\, \phi_i^2 \phi_{wall}^2.
\end{aligned}
\tag{6.3}
$$

The first term in the free energy $\mathcal{F}_{\text{CH}}$ is a Cahn-Hilliard free energy that encourages ϕ_i to take values 1, which we choose to correspond to the inside of the cell i, or 0, which denotes the region outside the cell. We choose the cell boundary to be located at $\phi = 1/2$. The boundary has width $\mathcal{O}(\lambda)$, set by the gradient term, and γ/λ is an energy scale. We account for the cell compressibility using a free energy term $\mathcal{F}_{\text{area}}$ which imposes a soft constraint, of strength μ, restricting the preferred area of each cell to πR^2. In the absence of other cell-cell interactions and active forces, this force causes cells to relax to circles. Given that this free energy contribution is summed over all cells, the cell monolayer in this model is compressible. The adhesive cell-cell interactions are given by $\mathcal{F}_{\text{adh}}$. The term $\lambda \int d\mathbf{x} \nabla\phi_i \cdot \nabla\phi_j$ measures the length of the contact line between two cells and ω/λ is an energy scale. Repulsive cell-cell interactions are determined by $\mathcal{F}_{\text{rep.}}$ which penalises overlap between cells with an energy scale κ/λ. The free energy $\mathcal{F}_{\text{wall}}$ allows us to define the boundary condition, by placing a fixed phase-field along the boundaries defined as $\phi_{wall} = e^{-2\text{d}}$ where d is the distance to the nearest wall. The repulsion between any given cell ϕ_i and the wall ϕ_{wall} is regulated by κ_{wall}. Note the λ dependence in the $\mathcal{F}_{\text{CH}}$, $\mathcal{F}_{\text{adh}}$, $\mathcal{F}_{\text{rep.}}$, and $\mathcal{F}_{\text{wall}}$ terms is choosen so that these terms scale with the cell width.

The velocity of the i'th phase $\mathbf{v}_i$ at a given point $\mathbf{x}$ is determined by the active force $\mathbf{f}_i^{\text{active}}(\mathbf{x})$ and passive force $\mathbf{f}_i^{\text{passive}}(\mathbf{x})$ [29, 30],

$$
\alpha \mathbf{v}_i(\mathbf{x}) = \mathbf{f}_i^{\text{active}}(\mathbf{x}) + \mathbf{f}_i^{\text{passive}}(\mathbf{x}), \tag{6.4}
$$

where α is a friction coefficient. Given the Reynolds number of cells are typically $\sim 10^{-4}$, we assume the dynamics are overdamped. The passive force $\mathbf{f}_i^{\text{passive}}$ accounts

for equilibrium cell properties defined by the free energy, such as the strength of cell-cell repulsion, deformability and compressibility. The passive force on the i'th cell is calculated as the integral of the local passive force density-weighted by ϕ_i

$$\mathbf{f}_i^{\text{passive}}(\mathbf{x}) = \int \mathrm{d}\mathbf{x}\ \phi_i \nabla \cdot \boldsymbol{\sigma}^p \tag{6.5}$$

where the passive stress tensor is given by

$$\boldsymbol{\sigma}^p = \sum_i \left(\frac{\delta \mathcal{F}_{CH}}{\delta \phi_i} + \frac{\delta \mathcal{F}_{area}}{\delta \phi_i} + \frac{\delta \mathcal{F}_{adh.}}{\delta \phi_i} - \frac{\delta \mathcal{F}_{rep.}}{\delta \phi_i} - \frac{\delta \mathcal{F}_{wall}}{\delta \phi_i}\right)\mathbb{I}. \tag{6.6}$$

It is worth noting that the integral in eqn. 6.5 can be transformed such that

$$\mathbf{f}_i^{\text{passive}}(\mathbf{x}) = -\int \mathrm{d}\mathbf{x}\ \boldsymbol{\sigma}^p \cdot \nabla \phi_i. \tag{6.7}$$

This expression highlights that the integral of the force exerted by the stress tensor acts normal to interface and points outwards.

Similarly, given the active stress $\boldsymbol{\sigma}^a$, one can define the active force as

$$\mathbf{f}_i^{\text{active}}(\mathbf{x}) = -\int \mathrm{d}\mathbf{x}\ \boldsymbol{\sigma}^a \cdot \nabla \phi_i. \tag{6.8}$$

Note however, that the active stress in this model is distinct from the continuum level active stress presented in section 3.6. One way to define the active stress for each cell in the phase-field model, involves defining a dipolar axis which determines the orientation of the cell's forces.

For example, one approach [29] involves aligning the dipolar axis to the elongation axis of the cell. In this work, the active stress is proportional to the magnitude of the cell elongation. The $\mathbf{Q}$-tensor in this work is given by

$$\mathbf{Q} = \sum_i \phi_i \mathbf{S}_i \tag{6.9}$$

where $\mathbf{S}_i$ is the traceless part of $-\int \mathrm{d}\mathbf{x}(\nabla\phi_i)^T(\nabla\phi_i)$. Its eigenvalues and eigenvectors measure the magnitude and orientation of the main deformation axes of the i'th cell. This active force results in a cell either pushing or pulling on its neighbouring cells, depending on their position relative to the elongation axis, as depicted in the inset of Fig. 6.4 (a). If the (extensile) activity is large enough the cells begin to deform and

form topological defects in the nematic field, as shown in Fig. 6.4 (b). Although, it should be noted that these topological defects do not form from the formation of bend or splay instabilities, like in continuum level active nematics [29]. Instead the defects form randomly throughout the monolayer, which is also the case in experiments on cell monolayers. Like continuum level active nematics, the defect density increases with activity and defects are always created in pairs.

This active stress can also be combined with polar forces to drive the cell motion [30]. The active force is the same as above, but an additional polar force is placed on the cells, as depicted in Fig. 6.4 (c) and (d). This polar force can be made to align to either the elongation axis of the cell, the cell velocity, or simply follow a random walk. In either case, the cell colony transitions from a jammed state to a liquid-like state, as the activity is increased. Additionally, for intermediate values of activity, a flocking state is observed when the polarisation is aligned to the cell velocity.

The work presented above ([29, 30]) has made significant progress in understanding how active nematic forces give rise to dynamic behaviour at the cellular level in confluent monolayers. The strength of these models is the ability to investigate the role of biological mechanisms such as contact-inhibition-of-locomotion in the collective motion of the monolayer. In the next chapter, we investigate how aligning each cell's active forces in the direction of least cell-cell contact (motivated by contact-inhibition-of-locomotion) influences the collective dynamics in both confined and unconfined clusters.

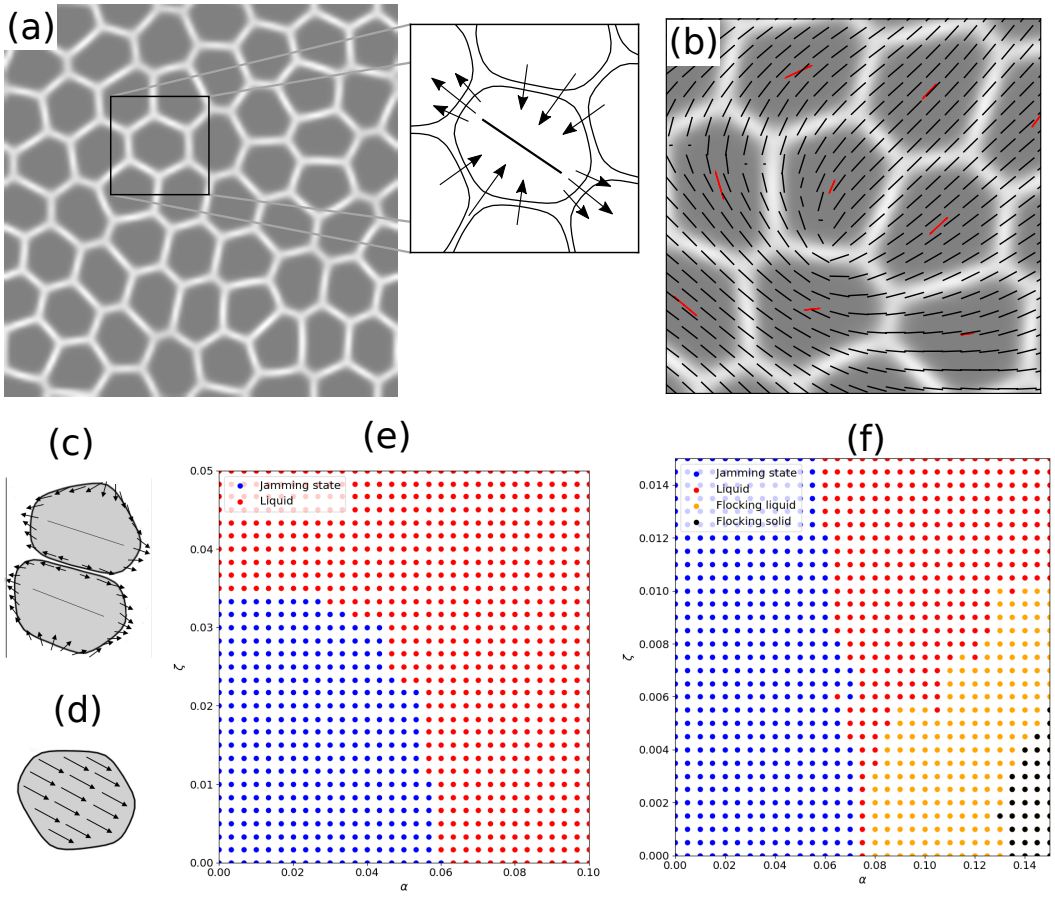


Figure 6.4: (a)-(b) are adapted from [29]. Snapshot of a monolayer of phases, with the active driving force of each cell depicted by the inset. The dipolar axis is parallel to the main deformation axis. (b) The dipolar axis field corresponding to the cell monolayer. (c)-(f) are adapted from [30]. Schematic of the (c) active forces on a cell-pair with the elongation axis given by the black line, and (d) polar force on a cell. (e) and (f) give the phase diagrams for when the polarisation is aligned to the cell elongation axis, and cell velocity respectively.

Chapter 7

Collective Motion in Active Nematic Droplets

In this chapter, we investigate the collective motion of a cell monolayer by simulating a cluster of 400 cells using a multi-phase field approach. An active nematic force drives the dynamics of each cell, and is oriented along the direction of least cell-cell overlap, which is inspired by the process of contact-inhibition-of-locomotion discussed in chapter 6. We also weight the active force by the amount of cell-cell overlap, which is motivated by the existence of cryptic lamellipodia as discussed in section 6.1.

The model recovers a wide range of interesting behaviour depending on whether the active forces are extensile or contractile. Extensile forces act to make cells circular, which in turn results in jammed hexagonal monolayers with little to no cell-cell rearrangement. In contrast, contractile forces actively compress the cells into an elongated form, forcing them to squeeze in between neighbouring cells, giving rise to significant cell-cell rearrangement.

The presence of a free edge is found to bias the direction of active forces towards the cluster's centre-of-mass for extensile forces, and away for contractile forces. This acts to compress extensile clusters, allowing them to close gaps in the bulk. Contractile clusters are found to generate holes in the bulk and form protrusions as they spread across any available space.

Finally, weighting the active stress by the amount of cell-cell overlap does not change the underlying behaviour, but only acts to effectively reduce the activity in the system. However, contractile clusters formed fewer holes in their bulk as the cells spread across the surface for particular combinations of the weighting and activity.

7.1 Model

We use the multi-phase field model outlined in section 6.3, with a collection of 400 fields ϕ_i evolving according to eqn. 6.1, under the free energy $\mathcal{F} = \mathcal{F}_{\text{CH}} + \mathcal{F}_{\text{area}} + \mathcal{F}_{\text{rep}} + \mathcal{F}_{\text{wall}} + \mathcal{F}_{\text{adh}}$. The velocity is determined by eqn. 6.4, with the passive force $\mathbf{f}_i^{\text{passive}}$ as given in eqn. 6.5. The main difference between the model used in this chapter, and the models presented in section 6.3, is that here we align the active force $\mathbf{f}^{\text{active}}$ to the direction of least cell-cell overlap. We also consider the affect of weighting the active force by the amount of cell-cell overlap.

The active force $\mathbf{f}_i^{\text{active}}$ of a cell is defined by the integral of the local active stress $\boldsymbol{\sigma}^a$, weighted by both the cells phase-field ϕ_i, and the exponential of the cells overlap with neighbouring cells,

$$\mathbf{f}_i^{\text{active}}(\mathbf{x}) = e^{-\eta \mathcal{O}_i} \int \mathrm{d}\mathbf{x}\ \phi_i \nabla \cdot \boldsymbol{\sigma}_i^a \tag{7.1}$$

where $\mathcal{O}_i = \int d\mathbf{x} {\phi_i}^2(\phi^2 - \phi_i^2)$ measures the amount of cell-cell overlap, $\phi(\mathbf{x}) = \sum_i \phi_i(\mathbf{x})$, and η regulates this weighting. In effect, this reduces the magnitude of the active forces in the bulk relative to those at a free edge. Given the exponent of the exponential must be unitless, $[\eta \mathcal{O}_i] = 1$, the parameter η must the reciprocal of an area, $[\eta] = \frac{1}{m^2}$, more precisely the area of cell-cell overlap.

This area can be seen as the product of two length scales, one corresponding to the length of the perimeter of a cell, l_p, and the other corresponding to the length of cell-cell overlap, l_{ov}. The former length scale is determined by the cell radius ($l_p \sim 2\pi R$), while the latter is regulated by the cell-cell adhesion and repulsion free energy terms, $\mathcal{F}_{rep}$ and $\mathcal{F}_{adh}$ given in eqn. 6.3. The square-root ratio of the coefficients in these terms defines the overlap length scale as $l_{ov} = \sqrt{\frac{\omega}{\kappa}}$. The scaling of the parameter η is then given by $\eta \sim \frac{1}{l_{ov}} \frac{1}{l_p}$. Given $\eta \sim \frac{1}{l_{ov}} \frac{1}{l_p}$, η corresponds to the magnitude that the active force is dampened per unit area of cell-cell overlap.
The local active stress is given by

$$\boldsymbol{\sigma}_i^a = -\zeta \sum_{k \neq i}^{N} \phi_k \mathbf{Q}_k \tag{7.2}$$

where $\mathbf{Q}_i = (\mathbf{n}_i \mathbf{n}_i - \mathbb{I}\frac{1}{2})$, and $\mathbf{n}_i = (\cos(\theta_i), \sin(\theta_i))$ defines the dipolar axis of the cell. Note that the active forces are only significant at locations of cell-cell overlap, given the

(implicit) factor of $\phi_i \nabla \phi_k$ in eqn 7.1. It is zero if there is nematic alignment between cells since the contributions to the active force from each cell cancels. Conversely, if the nematic fields are perpendicular to each other then the active forces reinforce. Overall, this term results in a force that is non-zero at locations of cell-cell overlap and is proportional to gradients in each cells nematic field. The strength of the active force is regulated by ζ, and active nematics with $\zeta > 0$ and $\zeta < 0$ are said to be extensile and contractile respectively.

To determine the orientation of each cells dipolar axis we align it to the direction of least cell-cell overlap given by

$$\boldsymbol{\mathcal{C}}_i = \int d\mathbf{x}(\phi_i)(\phi^2 - \phi_i^2)(\partial_x \phi_i, \partial_y \phi_i), \tag{7.3}$$

where θ_i evolves according to

$$\partial_t \theta_i = J_{nem} \angle(\boldsymbol{\mathcal{C}}_i^o, \mathbf{n}_i) + D_{nem} \xi. \tag{7.4}$$

ξ is Gaussian noise with unit standard deviation and magnitude D_{nem}, $\angle(\boldsymbol{\mathcal{C}}_i, \mathbf{n}_i)$ is the signed angle from $\boldsymbol{\mathcal{C}}_i$ to $\mathbf{n}_i$, chosen to lie in the interval $(-\pi, \pi)$, and J_{nem} controls the rate of alignment. The nematic symmetry allows for a choice of $\mathbf{n}_i$ or $-\mathbf{n}_i$. We choose the one that forms an acute angle with the direction of $\boldsymbol{\mathcal{C}}_i$ ($\mathbf{n}_i \cdot \boldsymbol{\mathcal{C}}_i \geq 0$).

We simulate 400 cells in boxes of size 500×500 lattice-sites (ls) for free clusters, 300×300 ls for the wound healing simulations, and 200×200 ls for confluent monolayers. Initially cells with radius $R/2$ are placed in either a solid square disc, or an annulus with a 9x9 cell wide hole, with the constraint that the distances between neighbouring centres is greater than R. The cells are then allowed to relax for 4000 time steps under passive dynamics to reach confluence. The dipolar axis of each cell is initialised such that $\theta_i = 0$ for all i. The simulations are run for $50,000$ time steps and data is collected every 500 time steps, except for the wound healing simulations which were run for $100,000$ simulation timesteps. Simulations were run for $250,000$ time steps when investigating the effect of active force inhibition. The parameter values are $\omega = 0.05$, $\lambda = 1.5$, $\gamma = 0.1$, $\kappa = 0.4$, $\kappa_{wall} = 0.4$, $R = 5$, $\mu = 6$, $\alpha = 1$, $S_i = 1.0$, $J_{nem} = 0.1$, and $D_{nem} = 0.01$. The value of ζ ranges from ± 0.06 to ± 0.16, and η is set to zero unless otherwise specified, when it takes values ranging from 1 to 10.

7.2 Confluent monolayers

A clear distinction between the behaviour of extensile and contractile cells can be seen by observing their motion in the bulk of confined confluent monolayers. Figs. 7.1(a) and (b) are snapshots comparing the two cases. It is immediately clear that the contractile cells are more elongated than the extensile ones. This is quantified in Fig. 7.1(c) with a histogram showing the distribution of cell shapes for $\mid \zeta \mid = 0.1$, where $D = \langle D_i(t) \rangle_{i,t}$ is the average cell deformation across all cells in an entire simulation. In particular, the deformation of a cell is measured by defining the deformation tensor of a cell as the traceless part of $\mathcal{D}_i = -\int \mathrm{d}\mathbf{x}\ (\nabla\phi_i)^T(\nabla\phi_i)$ [30]. The deformation of a cell at time t is then given by $D_i(t) = \sqrt{\mathcal{D}_{xx,i}(t)^2 + \mathcal{D}_{xy,i}(t)^2}$. Note that $D_i(t) = 0.5$ corresponds to isotropic cells and $D_i(t) = 3$ to cells with an aspect ratio ≈ 1.75.

The shape differences can be understood by observing how the active forces acting on a cell are correlated with the compressive forces exerted by neighbouring cells. The mechanism is illustrated schematically in the insets of Figs. 7.1 (a) and (b) for extensile and contractile cells respectively. If a cell is compressed in a given direction (green arrow), and using the definition of contact inhibition of locomotion that we consider here (eqn. (7.3)), the resulting cell-cell overlap will cause the cell's dipolar axis to be oriented along the black line in the figures. Hence the active force, shown in red, will (on average) act to oppose the deformation for extensile cells, returning them to a circular shape, whereas it increases the deformation for contractile cells, elongating them. This can also be seen in the main figures, where the direction and magnitude of the active force are shown by the black arrows and underlying colourmap.

The variation in cell shape has a significant impact on the monolayer's dynamics. In Fig. 7.1(d) we plot the rearrangement rate, the average number of times a cell in the monolayer changes its neighbours at a given simulation time step. Rearrangements increase with activity for contractile clusters, but remain close to zero for all values of the activity for extensile clusters showing that contractile cells move throughout the monolayer whereas extensile cells remain in a jammed state. This suggests that the elongated cells can move more easily. The distribution of velocities for $\mid \zeta \mid = 0.1$, shown in Fig. 7.1(e), indeed indicates that contractile cells show a significant tail of higher velocities, and the polar histogram plot in Fig. 7.1(f) indicates that the higher velocities are correlated with motion along the long axes of the cells.

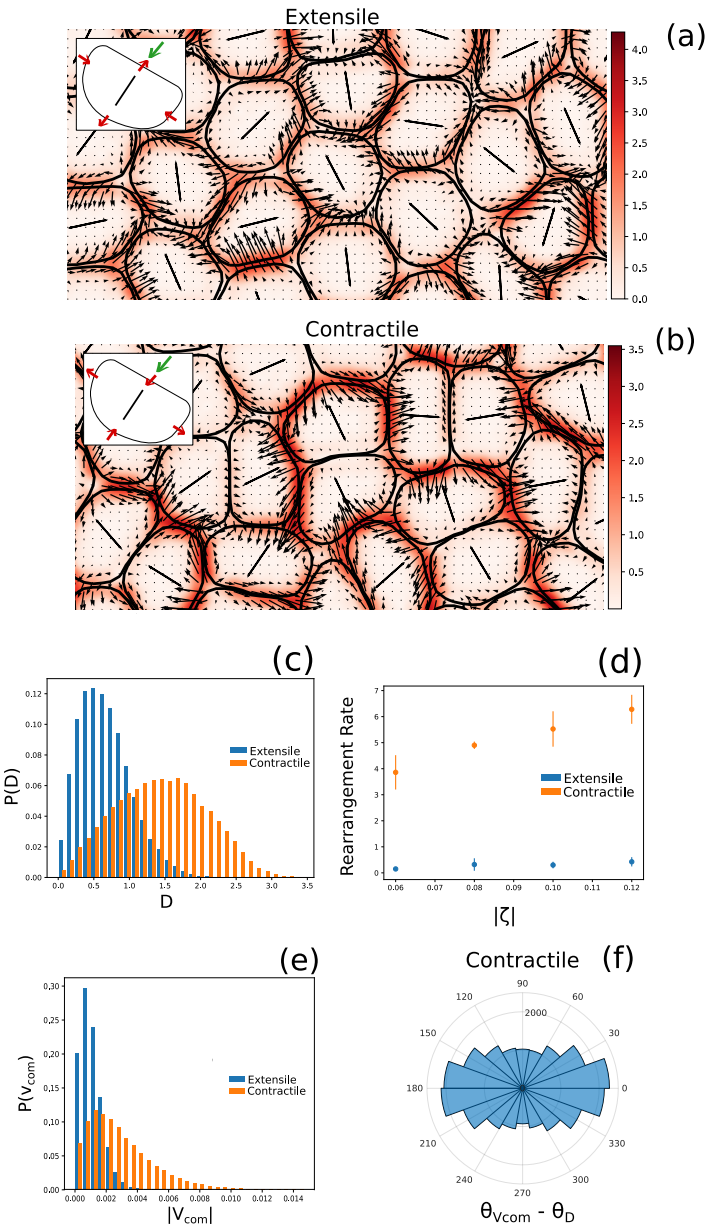


Figure 7.1: Panels (a) and (b) depict snapshots of extensile and contractile cells in the bulk of confluent cell layers respectively. The dipolar axis of each cell is depicted by a black dash, and the orientation and magnitude of the active force are given by the black arrows and underlying colourmap respectively. The inset illustrates the response of the active force, with the direction given by the red arrows, if compressed such that $\boldsymbol{\mathcal{C}}_o$ aligns along the green arrow. Panel (c) shows the distribution of cell elongations (D) in extensile and contractile cell layers. Panel (d) shows the cell-cell rearrangement rate as a function of ζ for extensile and contractile forces. Panel (e) shows the velocity distribution of the cells center of mass for these monolayers. Panel (f) shows the polar histogram of the difference between a cells elongation orientation (θ_{D}) and the direction of its motion (θ_{Vcom}).

7.3 Free Clusters

We next discuss the dynamics of cells in a colony with a free surface. Fig. 7.2 (a) and (b) compares snapshots of extensile and contractile clusters after 50,000 simulation time steps. The extensile cluster retains confluency, whereas the contractile system develops holes and protrusions and starts to break up. This can be quantified by measuring the evolution of the radius of gyration,

$$R_{Gyr}(t) = \frac{1}{N}\sum_i \sqrt{(\mathbf{x}_{com,i}(t) - \mathbf{x}_{com,cluster}(t))^2}$$

plotted in Fig. 7.2 (c) for different values of the activity. Extensile clusters are stable in shape, apart from a small initial compression. Contractile clusters, by contrast, spread out, with larger values of activity resulting in a faster increase in the radius of gyration.

The difference in behaviour is again a consequence of contact inhibition of locomotion which causes the dipolar axis of the cells at the interface to orient away from the bulk, together with the anisotropy of the forces acting on the boundary cells. This is illustrated by the snapshots in Fig. 7.2 (e) and (f) which show the dipolar axis field and active forces acting on boundary cells that are held in place by passive steric forces from a fixed wall along the edge of the simulation box.

The bias in the orientation of the active forces near the interface can be seen by calculating the polar plot of the sum of all active forces binned by the difference between the angle of the active force ($\theta_{f^{active}}$) at a given lattice-site, and the angle to the cluster's centre-of-mass from that lattice site (θ_{com}). Fig. 7.2 (d) show this (normalised) polar plot for the outer three layers (solid lines) of cells of extensile (blue) and contractile (orange) monolayers, and for the remainder of the cells respectively (dashed lines). The forces on the outer cell layers preferentially point towards the centre of the cluster for extensile cells, resulting in the cluster being under compression. For contractile driving, however, the outer layers tend to pull the cluster apart. The force anisotropy is reduced for cells in the bulk.

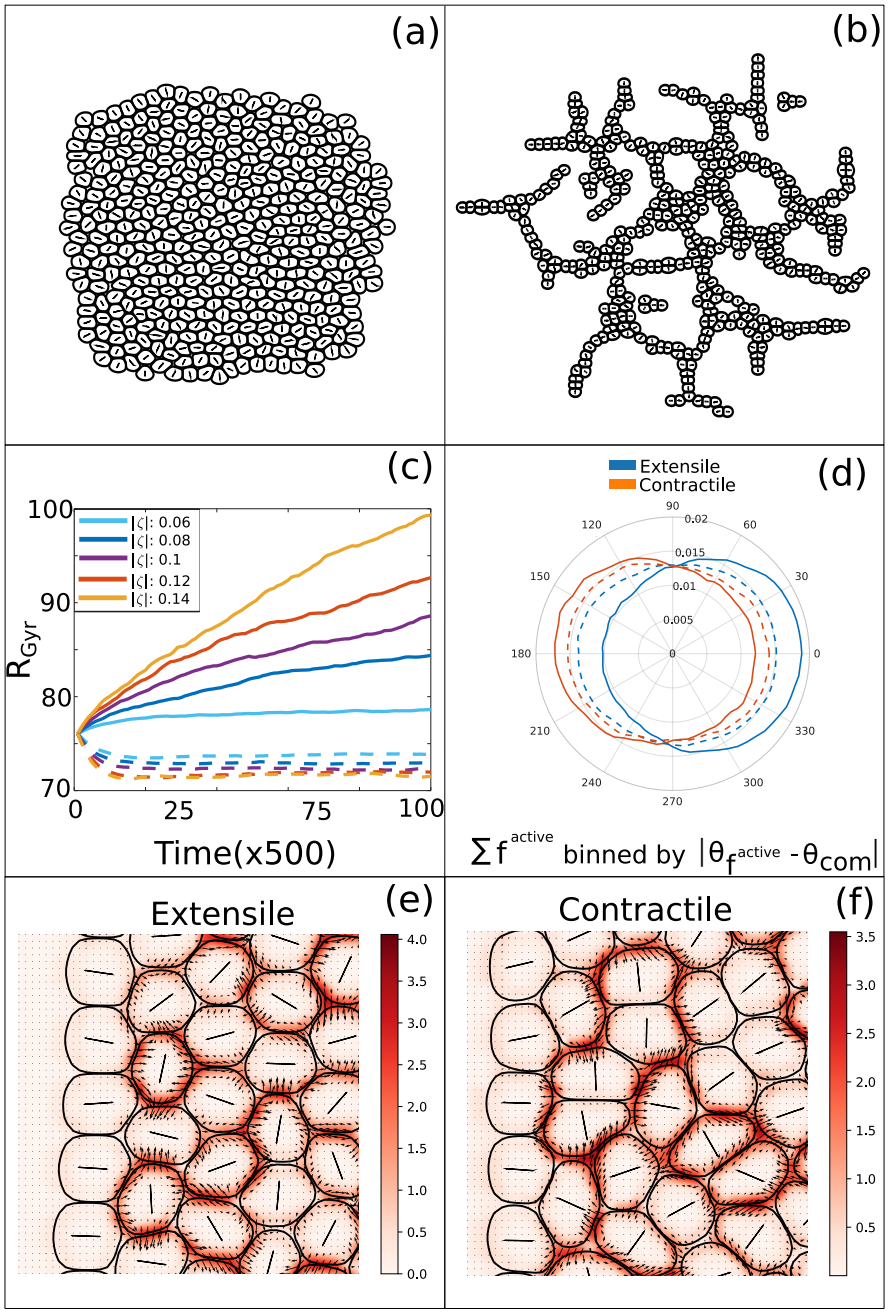


Figure 7.2: Panels (a) and (b) show a snapshot of the morphological structure of contractile and extensile clusters respectively, after 50,000 timesteps, with each cells dipolar axis orientation given by a black dash. Panel (c) is the radius of gyration as a function of simulation time, where the solid and dashed lines are for contractile and extensile clusters respectively. Panel (d) shows the (normalised) sum of active forces binned by the difference between the force's direction and the direction to the cluster's centre of mass from the location of the force. Solid lines indicate the sum was taken over the outer three layers of cells, and the dashed lines the remainder of the cells. Panels (e) and (f) show the edge of a confined confluent layer, with the dipolar axis given by the black dash, and the active forces magnitude and orientation given by the underlying colourmap and black arrows respectively.

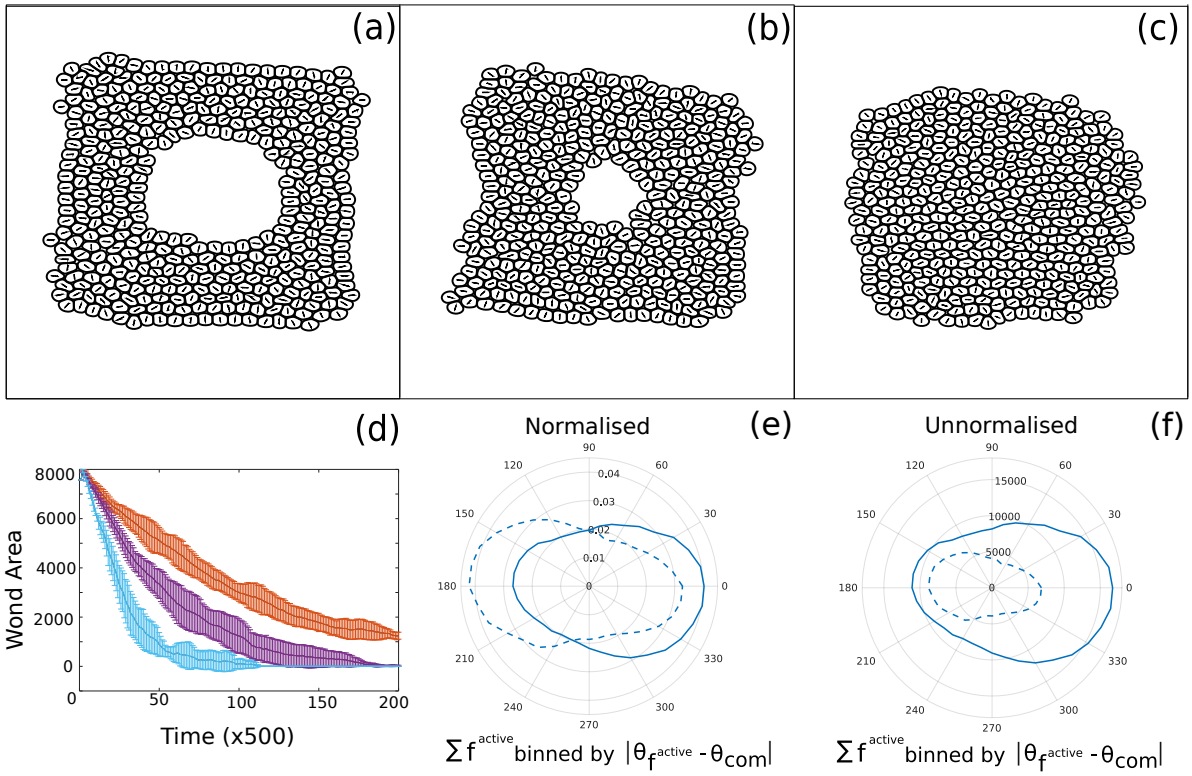


Figure 7.3: Panels (a)-(c) depict snapshots of an extensile cluster after 0 (a), 50,000 (b), and 100,000 (c) simulation timesteps. Panel (d) shows the mean area of the wound as a function of simulation time (x500), averaged across four simulations with the standard deviation shown by the error bars. Each colour represents a different activity, red for $\zeta = 0.1$ (upper), purple for $\zeta = 0.12$ (middle), and $\zeta = 0.16$ for blue (bottom). The (e) normalised and unnormalised (f) sum of active forces along the outer boundary (solid line) and inner boundary (dashed line) across an entire simulation.

7.4 Wound healing

Interestingly, despite the jammed-like state of extensile clusters, the monolayers can still undergo significant morphological changes. This is observed by displacing a 9x9 grid of cells in the centre of the cluster to the interface, as shown in Fig. 7.3 (a). This resembles wound healing experiments in epithelial monolayers [110]. Over time the cluster heals as the hole closes, as shown in Fig. 7.3 (a)-(c), which shows snapshots of the cluster's morphology as the simulation progresses. This healing is due to the active forces at the outer interface compressing the cluster. Note that while the inner interface acts to

expand the hole, since the active forces there are directed towards the bulk of cells, there are more cells at the outer interface resulting in a net compressive force. This can be seen in the polar plot of the sum of active forces, binned by the difference between the force's angle and the angle towards the cluster's centre of mass, like in Fig. 7.2 (d). The normalised and unnormalised forces are given in Fig. 7.3 (e) and (f) respectively. The healing rate was quantified by measuring the area of the hole as a function of simulation time, and is shown in Fig. 7.3 (d) for various values of activity. The area decreases faster for larger values of activity. The rate at which the area decreases appears to be roughly linear until the hole gets small, at which point the area decreases at a slower rate.

The length-scale and time-scale of simulations can be mapped to S.I. units by comparing simulations and experiments of circular wounds [110]. The cell diameter in simulations is about 10 lattice-sties (ls), whereas cells are about 20 μm, meaning 1 ls $\approx 2\mu$m. In experiments, a circular wound of area $4000\mu\text{m}^2$ closes in about 100 minutes. Comparing this to simulations, where an area of 8000 ls^2 closes in about 75,000 timesteps, allows one to map the timescale in simulations such that 750 timesteps $\approx$ 1min.

7.5 Active force inhibition

An important physical property of cell monolayers is that cells at the boundary of the cluster exert stronger traction forces than those in the bulk [105]. We incorporate this property into the model by penalising the active force as a function of cell-cell overlap, the strength of which is controlled by the parameter η. Simulations were run for four values of η that correspond to no ($\eta = 0$), light ($\eta = 1$), intermediate ($\eta = 5$), and large ($\eta = 10$) penalisations of the active force. We find that that the morphological structure of contractile clusters changes, with fewer holes in the bulk for larger values of η. This can be seen in Fig. 7.4 which shows a snapshot of contractile clusters for various values of ζ and η, at 250,000 timesteps. Interestingly, it seems possible to have clusters which form protrusions but have little to no holes (e.g. $(\zeta, \eta) = (-0.12, 5)$). We also measured the effect of η on the radius of gyration, wound healing rate and rearrangement rate. The results are shown in Fig. 7.5, which show that weighting the active force by the cell-cell overlap simply makes the system less active.

Overall, weighting the active force by the amount of cell-cell overlap seems to simply

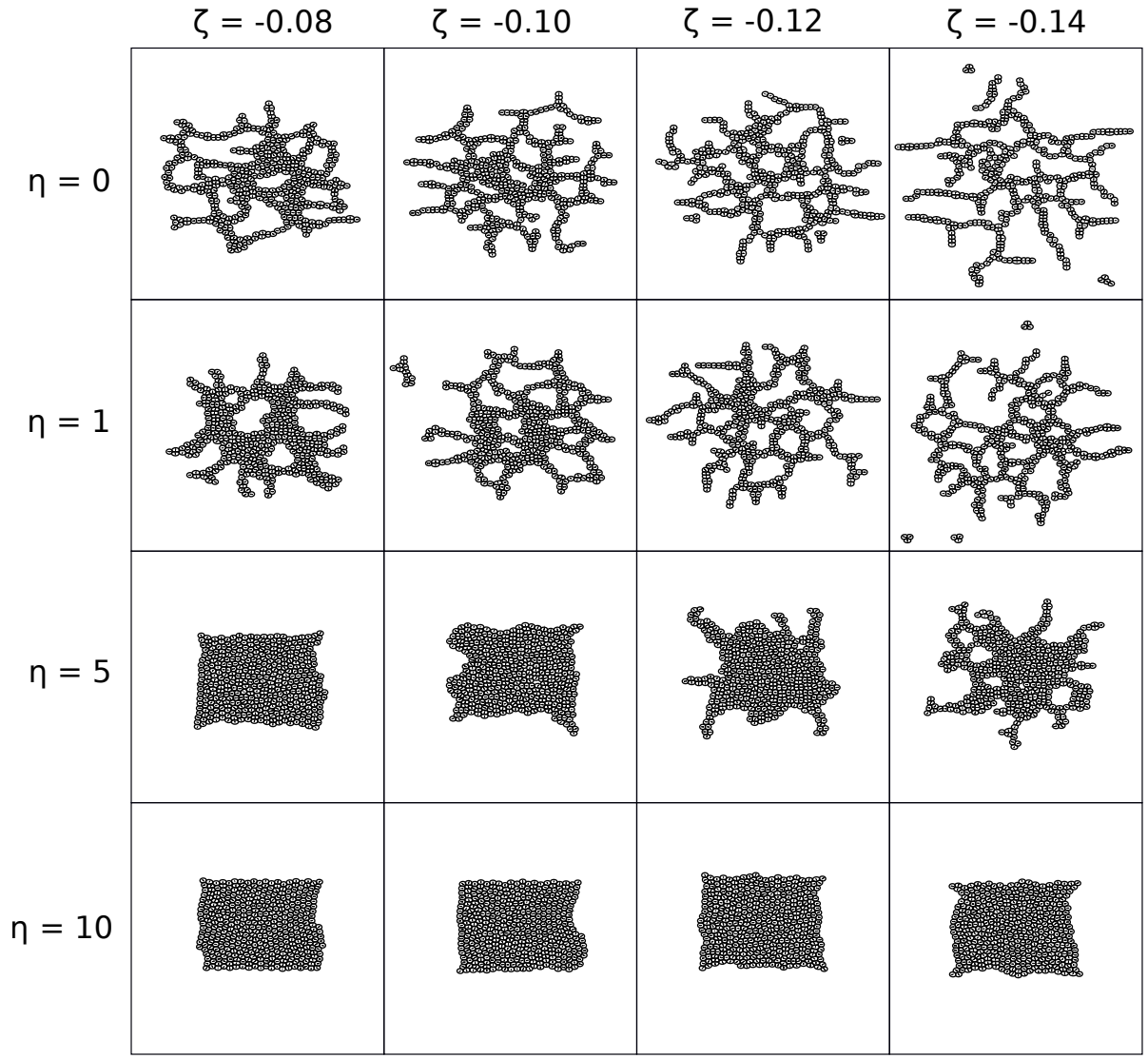


Figure 7.4: Snapshots of clusters after 250,000 timesteps for varying values of ζ and η. Note that clusters with large values of ζ and η have fewer holes across time but retain their ability to form protrusions. Clusters with smaller values of ζ and η have many more holes in the bulk, at any given timestep.

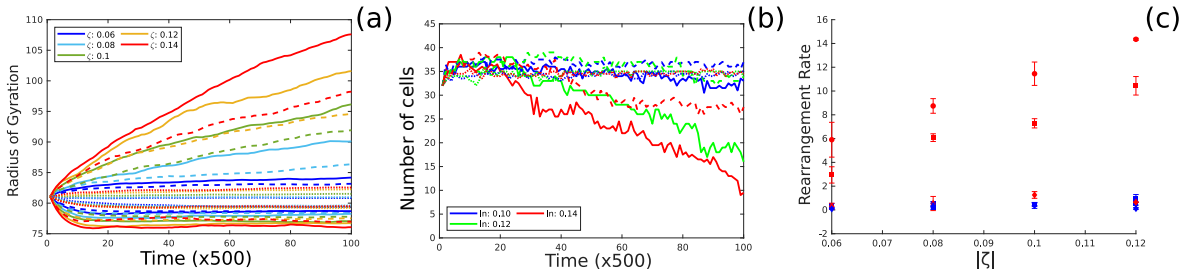


Figure 7.5: Measurements of (a) radius of gyration and (b) number cells in the inner ring of an annulus, as a function of time for the different values of activity shown in the legend, and η. Solid lines are for $\eta = 0$, dashed lines for $\eta = 1$ and dotted lines for $\eta = 10$. (c) shows the rearrangement rate as a function of $|\zeta|$ for multiple values of η. Discs are for $\eta = 0$, Squares for $\eta = 1$ and diamonds for $\eta = 10$. Values for $\eta = 5$ aren't shown for clarity.

decrease the amount of activity in the system, except for reducing the number of holes in contractile clusters while still allowing them to spread.

7.6 Conclusion

This work presents how large-scale morphological dynamics of cell clusters can arise from an active multi-phase field framework. We find that extensile forces result in a jammed-like state where there is a little-to-no cell-cell rearrangement. The interplay between contact-inhibition-of-locomotion and the active forces result in circular cells. Despite the absence of cell-cell rearrangement, extensile clusters can still heal wounds present in a cluster, due to contact-inhibition-of-locomotion directing forces towards the bulk. Contractile forces result in a fluid-like state with significant cell-cell rearrangement. These forces result in cell compression and elongation, which squeeze cells to move in the direction of elongation. At the tissue level, contractile clusters spread out and form mesh-like networks one or two cells wide. By weighting the active force by the amount of cell-cell overlap we find that contractile clusters form fewer protrusions and holes. This weighting also has the effect of dampening the increase in the radius of gyration, wound healing rate, and cell-cell rearrangement rate.

A vast range of interesting dynamics arises from this interplay between active nematic forces and contact-inhibition-of-locomotion. However, a popular choice to driving the dynamics is through a polarisation force, and it would be interesting to bridge these two approaches by placing a combination of polarisation forces, active nematic forces, and contact-inhibition-of-locomotion on the cells.

Chapter 8

Conclusion and outlook

Section 8.1 summarises the main results from the novel work presented in this thesis, while Section 8.2 provides an outlook for future research.

8.1 Summary of conclusions

In Chapter 4, we show that the characteristic length scale of strongly confined active nematics is not the active length scale, but rather the instability length scale. The dynamics are found to be independent of activity, and strongly depend on the channel width.

We also show the importance of topological defects in controlling active nematic flows in confinement. The weak anchoring of the nematic field at the boundary, in combination with the free-slip boundary conditions, allow topological defects to form at the walls. The $-\frac{1}{2}$ defects remain close to the walls at a distance set by the anchoring penetration length, due to a lack of self-propulsion and elastic forces. The $+\frac{1}{2}$ defects self-propel perpendicular to the wall if the channel is wide enough.

For very narrow channels the active fluid exhibits a shear-flow that generates bend instabilities perpendicular to the walls. These instabilities grow and result in the creation of topological defect pairs that immediately annihilate with themselves. The system returns to the shear-flow state and the process repeats.

Widening the channel results in the separation of the $\pm\frac{1}{2}$ defect pairs, with the $+\frac{1}{2}$ defects propelling away from the wall. The state is characterised by pairs of defects along the channel and an array of vortices. However, this state is transient, as the $+\frac{1}{2}$ defects quickly annihilate with the $-\frac{1}{2}$ defects at the opposite wall. Again, the system enters a shear-flow state, and the process repeats.

Further widening the channel allows the $+\frac{1}{2}$ defects to escape from the walls without annihilating with the $-\frac{1}{2}$ defects at the opposite side. The active fluid exhibits a

dancing disclination state with dual-populations of $+\frac{1}{2}$ defects moving along sinusoidal trajectories in opposite directions. Finally, widening the channel further until multiple defects can fit between the channel walls results in active turbulence.

In Chapter 5, we created a model to describe how collective chemotaxis may arise within an active nematic framework. Continuum simulations were used to describe a cell cluster as an active nematic droplet. To model experimental setups, a chemical field diffused from a source along the top side of the channel and could freely diffuse out the bottom side. The chemical field was also depleted by the droplet. The active nematic was coupled to the chemical field by weighting the active stress linearly in the chemical concentration.

We found that this simple coupling was enough to give rise to the net motion of the droplet in the direction of the chemical field. The active anchoring at the boundary of the cluster made the nematic field align parallel or perpendicular to the interface for extensile and contractile clusters respectively. On average, this directed the flows generated inside the bulk radially. The asymmetry in the chemical field then translated to an asymmetry in the magnitude of the (average) radial flows generated inside the droplet. The stronger radial flows on the side closest to the chemical source resulted in the net motion of the cluster towards that chemical source. This results in a motion akin to collective chemotaxis.

This model system allowed us to investigate the influence of cluster size and activity on the efficiency of collective chemotaxis in active nematic droplets. Increasing the activity resulted in larger cluster velocities, without affecting how well the cluster migrates, as measured through the chemotactic index. Further, we found that larger clusters were able to migrate much more effectively than smaller clusters, while the velocity of each cluster was found to be independent of its size. Additionally, the smaller clusters were found to undergo periods of rotation, due to the periodic creation and annihilation of two $+\frac{1}{2}$ defects in the bulk, which generate a single large vortex within the cluster.

In Chapter 7, we investigated how active nematic forces can be used to drive collective motion in cell monolayers, at the cellular level. To do this, we used a multi-phase field model to simulate a collection of 400 cells, with each cell modelled by an individual phase. The cells exerted a nematic force on their neighbours, with the force directed towards the location of least cell-cell contact. We considered both confluent monolayers

in a closed box, and unconfined clusters free to expand into the surrounding space.

In confinement, the dynamics of confluent monolayers depended heavily on whether the nematic forces were extensile or contractile. Contractile forces were found to result in elongated cells that had significant cell-cell rearrangement. Any passive compression of a cell by its neighbours was further exacerbated by the active force. This resulted in cells being squeezed out of their current position and moving preferentially in the direction of their elongation. Extensile forces were found to result in circular cells that had little-to-no cell-cell rearrangement. In contrast to contractile cells, any passive compression of an extensile cell is compensated by the extensile active forces. This acts to keep the cells circular and in consequence, in a jammed state.

The morphological structures of the cell clusters were also investigated. This was achieved by allowing the clusters to freely expand into their surroundings. As in confluence, the dynamics of contractile and extensile clusters were distinct. Contractile clusters were found to expand into mesh-like structures, with the mesh one or two cells wide. This process was aided by the fluid-like motion of the cluster and the bias of the boundary cells nematic forces to be directed away from the bulk. Extensile clusters formed a solid circular shape, due to the compressive nature of the active forces at the interface, which was preferentially aligned towards the bulk. Despite the seemingly passive nature of the extensile clusters, they were able to undergo significant structural changes, reflected by their ability to close artificial wounds in the bulk. The ability relies on the compressive nature of the outer interface.

Finally, we also considered how weighting the active forces by the magnitude of cell-cell overlap influenced the dynamics. We found that the weighting largely made the system more passive, except that contractile clusters that were free to expand made fewer holes in their bulk.

8.2 Outlook

There are many points at which the work presented in this thesis could be expanded.

For example, the work on collective chemotaxis discussed in 5 could be extended to incorporate a more realistic environment. Experimental and theoretical studies typically focus on clusters migrating on a substrate. However, in vivo, the environment is much richer and more dynamic, consisting of a complex mixture of cell types and extracellular

matrix. In embryogenesis, cell clusters must migrate through, and detect chemical signals that, travel through surrounding tissues. This leads to questions such as how does the dynamical nature of the surrounding environment affect the ability of a cluster to collectively migrate, and how robust are the known mechanisms of collective chemotaxis in such an environment.

Within the continuum level active nematic approach, one could extend the work presented in 5 by modelling the space surrounding the active droplet as a distinct cell colony, or active nematic fluid. This may help understand how the collective chemotaxis of a cluster is affected when migrating through another set of cells. Further, the active motion of the second fluid may interfere with the migrating cluster's ability to sense the chemical field, thereby affecting its ability to chemotax. It would be interesting to observe the limits at which collective chemotaxis breaks down in such a system. It may be the case that a temporal gradient sensing mechanism offers better trade-offs than a direct local measurement of the chemical field.

At the cellular level, a multi-phase field model could be used to better understand the ability of a cluster to undergo collective chemotaxis through a monolayer of distinct cells. A nice property of the phase-field model is that different populations of cells can be simulated, each with a unique set of physical properties. For example, each cell population could have different magnitudes of cell stiffness and cell-cell adhesion. Further, the cellular interactions between species could also be tuned, allowing for an even more detailed study. As with the continuum approach, the motion of the non-migrating cells could advect or consume the diffusing chemical, thereby affecting the ability of the migrating cluster to detect the chemical.

An important line of research that would provide valuable insights into the movement of active matter involves bridging the gap between continuum level active nematics and the active nematic multi-phase field model. For example, the orientation of the director field at the continuum level reorients due to the flow of the particles, and there is currently no clear analogue of this at the cellular level. One approach might be to align the nematic field to the average orientation of the cells to generate a cellular analogue of the tumbling parameter. This also seems necessary for active anchoring to arise in the cellular framework since this mechanism relies on the director field realigning in the flow-field.

Appendices

Appendix A

Implementation of the Models

To better understand the dynamics of active nematic liquid crystals we solve the Beris-Edward and Cahn-Hillard equations numerically. The Navier-stokes equations are solved numerically using a Lattice Boltzmann method with a BKG collision operator [121]. This is solved in the weakly compressible limit, where the density ρ is allowed to fluctuate around $\rho = 1$. The Beris-Edward (eqn. 2.13) and Cahn-Hillard (eqn. 5.4) equations are solved using a finite difference approach put forward by Marenduzzo [47]. This section provides details on how these equations were numerically solved to obtain the results in this thesis.

A.1 The Lattice Boltzmann Method

The Lattice-Boltzmann [121] method involves discretising space, time and velocity to numerically solve the Navier-Stokes equations. The spatial discretisation is performed by defining a square grid in two-dimensional space where each lattice-site is connected to itself and its eight surrounding neighbours. This two-dimensional square grid where each lattice point has nine connections is denoted D2Q9, and can be seen in Fig A.1 (a). The arrows represent the discretised velocity vector that connects the lattice sites, which are given by $\mathbf{c}_i = (0,0), (\pm 1, 0), (0, \pm 1)$ and $(\pm 1, \pm 1)$. Time is discretised so that the parameter t evolves in fixed increments of Δt.

The LB method represents particles by a particle distribution function $f_i(\mathbf{x}, t)$, which is defined at each lattice-site $\mathbf{x}$, timestep t and by the direction 'i' it moves along $\mathbf{c}_i$. The macroscopic variables can be recovered through the moments of f_i. For example by summing up all the distributions components at a give lattice site, one recovers the local density at that lattice site,

$$\rho(\mathbf{x}, t) = \sum_i f_i(\mathbf{x}, t) \tag{A.1}$$

The local velocity can be obtained from

$$\rho\mathbf{u}(\mathbf{x},t) = \sum_i \mathbf{c}_i f_i(\mathbf{x},t). \tag{A.2}$$

The particle distribution evolves according to the Boltzmann equation

$$f_i(\mathbf{x}+\mathbf{c}_i\Delta t, t+\Delta t) = f_i(\mathbf{x},t) + \Omega_i(\mathbf{x},t) \tag{A.3}$$

where $\Omega_i(\mathbf{x},t)$ is a collision-operator. This operator models collisions by redistributing the particles amoung the populations f_i at each lattice-site. There are many valid choices for Ω_i but the simplest, and the one we use here, is the Bhatnagar-Gross-Krook (BGK) operator,

$$\Omega_i(f) = -\frac{f_i - f_i^{eq}}{\tau}\Delta t + B_i \tag{A.4}$$

where B_i accounts for the body forces which arise from the stresses and the friction. Including the stresses in the body force results in a first-order accuracy, which is sufficient for the work presented in this thesis since the error terms are very small. The population of particles relax towards the equilibrium distribution f^{eq} on a time scale determined by τ. The equilibrium distribution has same moments as f_i,

$$\sum_i f_i^{eq}(\mathbf{x},t) = \sum_i f_i(\mathbf{x},t) = \rho(\mathbf{x},t) \tag{A.5}$$

$$\sum_i \mathbf{c}_i f_i^{eq}(\mathbf{x},t) = \sum_i \mathbf{c}_i f_i(\mathbf{x},t) = \rho\mathbf{u}(\mathbf{x},t), \tag{A.6}$$

The zeroth and first moments of f^{eq} ensure that the mass and momentum are conserved.

It is insightful to think of the Boltzman equation updating over two distinct steps, the *collision* and *streaming* steps. In the collision step, the particle distributions at each lattice site are updated so that they relax towards their equilibrium state,

$$f_i^*(\mathbf{x},t) = f_i(\mathbf{x},t) - \frac{f_i(\mathbf{x},t) - f_i^{eq}(\mathbf{x},t)}{\tau}\Delta t \tag{A.7}$$

where f_i^* represents the local distribution after this update. The next step, streaming, is where the particle distributions are redistributed among the lattice sites, such that

$$f_i(\mathbf{x}+\mathbf{c}_i\Delta t, t+\Delta t) = f_i^*(\mathbf{x},t) \tag{A.8}$$

which is depicted in Fig A.1 (b)-(c). This shows the particle distribution streaming from a central node to the neighbouring sites (black arrows), and the neighbouring distributions streaming to the central node (grey arrows).

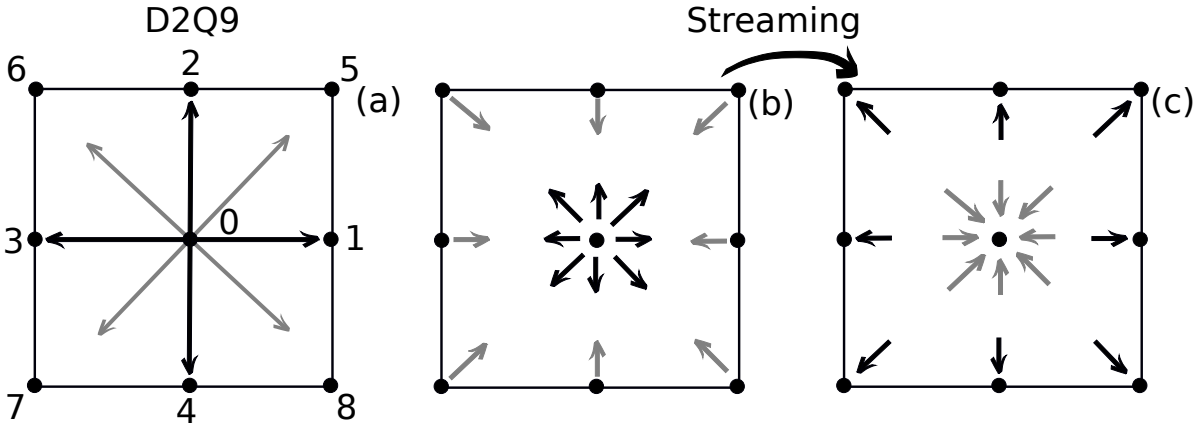


Figure A.1: (a) Depiction of the D2Q9 lattice. (b)-(c) depiction of the streaming step when updating the population distribution.

The Navier-Stokes equations (eqn. 2.16 and eqn. 2.17) with the additional stresses (eqn. 2.18 and eqn. 3.4) can be derived using the Lattice-Boltzmann equation (A.3), BKG operator (eqn. A.4) and moments of f^{eq} (eqn. A.5 and eqn. A.6) by performing Chapman-Eskog analysis [LB]. This involves Taylor expanding the Boltzmann equation (eqn. A.3), grouping the various terms by the order of their error, and performing some algebra.

A.2 Finite Difference Method

The Beris-Edwards equation (eqn. 2.13) and Cahn-Hillard equation (eqn. 5.4) are solved using a simple finite difference scheme. In this approach, one specifies the relevant quantities at time t, and then calculates the value of each field ϕ at a future time step '$t + \Delta t$'. For example, the concentration field at the next time step is given by

$$\phi(t + \Delta t) = \phi(t) + \Delta t(\Gamma_\phi \nabla^2 \mu - \nabla \cdot (\mathbf{u}\phi)), \tag{A.9}$$

and each component of the $\mathbf{Q}$ tensor is given by

$$Q_{ij}(t + \Delta t) = Q_{ij}(t) + \Delta t(S_{ij} + \Gamma H_{ij} - (\mathbf{u} \cdot \nabla)Q_{ij}). \tag{A.10}$$

Note that the symmetry and tracelessness of the $\mathbf{Q}$-tensor means that we only have to solve for a subset of the components, namely five for a three dimensional $\mathbf{Q}$-tensor and

two for a two-dimensional $\mathbf{Q}$-tensor. As with the lattice boltzmann method the time increment is set to unity, $\Delta t = 1$.

Bibliography

[1]T. Vicsek, A. Czirók, E. Ben-Jacob, I. Cohen, and O. Shochet, "Novel type of phase transition in a system of self-driven particles", Phys. Rev. Lett. **75**, 1226–1229 (1995).

[2]C. W. Reynolds, "Flocks, herds and schools: a distributed behavioral model", SIGGRAPH Comput. Graph. **21**, 25–34 (1987).

[3]J. Toner and Y. Tu, "Long-range order in a two-dimensional dynamical xy model: how birds fly together", Phys. Rev. Lett. **75**, 4326–4329 (1995).

[4]J. Toner and Y. Tu, "Flocks, herds, and schools: a quantitative theory of flocking", Phys. Rev. E **58**, 4828–4858 (1998).

[5]M. C. Marchetti, J. F. Joanny, S. Ramaswamy, T. B. Liverpool, J. Prost, M. Rao, and R. A. Simha, "Hydrodynamics of soft active matter", Rev. Mod. Phys. **85**, 1143–1189 (2013).

[6]R. A. Simha and S. Ramaswamy, "Hydrodynamic fluctuations and instabilities in ordered suspensions of self-propelled particles", Phys. Rev. Lett. **89**, 058101 (2002).

[7]D. Volfson, S. Cookson, F. Hasty, and L. S. Tsimring, "Biomechanical ordering of dense cell populations", Proc. Nat. Aca. Sci. **105**, 15346–15351 (2008).

[8]H. Li, X. Shi, M. Huang, X. Chen, M. Xiao, C. Liu, H. Chaté, and H. P. Zhang, "Data-driven quantitative modeling of bacterial active nematics", Proc. Nat. Aca. Sci. **116**, 777–785 (2019).

[9]G. Duclos, C. Erlenkämper, J. Joanny, and P. Silberzan, "Topological defects in confined populations of spindle-shaped cells", Nat. Phys. **13**, 58–62 (2017).

[10]T. B. Saw, A. Doostmohammadi, V. Nier, L. Kocgozlu, S. Thampi, Y. Toyama, P. Marcq, C. Lim, J. M. Yeomans, and B. Ladoux, "Topological defects in epithelia govern cell death and extrusion", Nature **544**, 212–216 (2017).

[11]K. Kawaguchi, R. Kageyama, and M. Sano, "Topological defects control collective dynamics in neural progenitor cell cultures", Nature **545**, 327 (2017).

[12]A. Doostmohammadi, S. P. Thampi, and J. M. Yeomans, "Defect-mediated morphologies in growing cell colonies", Phys. Rev. Lett. **117**, 048102 (2016).

[13]K. Copenhagen, R. Alert, N. S. Wingreen, and J. W. Shaevitz, "Topological defects promote layer formation in myxococcus xanthus colonies", Nat. Phys. **17**, 211–215 (2021).

[14]A. Livshits, L. Shani-Zerbib, Y. M.-Sacks, E. Braun, and K. Keren, "Structural inheritance of the actin cytoskeletal organization determines the body axis in regenerating hydra", Cell Reports **18**, 1410–1421 (2017).

[15]Y. -Sacks, L. Garion, L. Shani-Zerbib, A. Livshits, E. Braun, and K. Keren, "Topological defects in the nematic order of actin fibers as organization centers of hydra morphogenesis", bioRxiv (2020).

[16]N. Kumar, R. Zhang, J. J. de Pablo, and M. L. Gardel, "Tunable structure and dynamics of active liquid crystals", Sci. Adv. **4** (2018).

[17]R. Zhang, N. Kumar, J. L. Ross, M. L. Gardel, and J. J. de Pablo, "Interplay of structure, elasticity, and dynamics in actin-based nematic materials", Proc. Nat. Aca. Sci. **115**, E124–E133 (2018).

[18]F. C. Keber, E. Loiseau, T. Sanchez, S. J. DeCamp, L. Giomi, M. J. Bowick, M. C. Marchetti, Z. Dogic, and A. R. Bausch, "Topology and dynamics of active nematic vesicles", Science **345**, 1135–1139 (2014).

[19]P. Guillamat, J. Ignés-Mullol, and F. Sagués, "Control of active liquid crystals with a magnetic field", Proc. Nat. Aca. Sci. **113**, 5498–5502 (2016).

[20]T. N. Shendruk, A. Doostmohammadi, K. Thijssen, and J. M. Yeomans, "Dancing disclinations in confined active nematics", Soft Matter **13**, 3853–3862 (2017).

[21]G. H. Wadhams and J. P. Armitage, "Making sense of it all: bacterial chemotaxis", Nat. Rev. Mol. Cell Bio. **5**, 1024–1037 (2004).

[22]G. Malet-Engra, W. Yu, A. Oldani, J. Rey-Barroso, N. S. Gov, G. Scita, and L. Dupré, "Collective cell motility promotes chemotactic prowess and resistance to chemorepulsion", Cur. Bio. **25**, 242–250 (2015).

[23]B. A. Camley, "Collective gradient sensing and chemotaxis: modeling and recent developments", Jour. of Phys. Cond. Mat. **30**, 223001 (2018).

[24]A. Shellard, A. Szabó, X. Trepat, and R. Mayor, "Supracellular contraction at the rear of neural crest cell groups drives collective chemotaxis", Science **362**, 339–343 (2018).

[25]B. A. Camley, J. Zimmermann, H. Levine, and W. Rappel, "Emergent collective chemotaxis without single-cell gradient sensing", Phys. Rev. Let. **116**, 098101–098101 (2016).

[26]A. Shamloo, "Cell-cell interactions mediate cytoskeleton organization and collective endothelial cell chemotaxis", Cytoskeleton **71**, 501–512 (2014).

[27]T. Theveneau, L. Marchant, S. Kuriyama, M. Gull, B. Moepps, M. Parsons, and R. Mayor, "Collective chemotaxis requires contact-dependent cell polarity", Dev. Cell **19**, 39–53 (2010).

[28]R. Alert and X. Trepat, "Physical models of collective cell migration", Ann. Rev. Cond. Matt. Phys. **11**, 77–101 (2020).

[29]R. Mueller, J. M. Yeomans, and A. Doostmohammadi, "Emergence of active nematic behavior in monolayers of isotropic cells", Phys. rev. lett. **122**, 048004 (2019).

[30]G. Zhang, R. Mueller, A. Doostmohammadi, and J. M. Yeomans, "Active intercellular forces in collective cell motility", Jour. Roy. Soc. Int. **17**, 20200312 (2020).

[31]P. G. de Gennes and J. Prost, *The physics of liquid crystals* (Oxford University Press, 1995).

[32]L. D. Landau and D. Ter-Haar, *Collected papers of L.D. Landau* (Pergamon, Oxford, 1965).

[33]L. Longa and W. Tomczyk, "Twist–bend nematic phase from the landau–de gennes perspective", Jour. Phys. Chem. C **124**, 22761–22775 (2020).

[34]R. L. C. Vink, "Crossover from a kosterlitz-thouless phase transition to a discontinuous phase transition in two-dimensional liquid crystals", Phys. Rev. E **90**, 062132 (2014).

[35]K. Schiele and S. Trimper, "On the elastic constants of a nematic liquid crystal", Phys. Stat. Sol. **118**, 267–274 (1983).

[36]A. Doostmohammadi, J. Ignés-Mullol, J. M. Yeomans, and F. Sagués, "Active nematics", Nat. Comm. **9**, 3246 (2018).

[37]M. Nobili and G. Durand, "Disorientation-induced disordering at a nematic-liquid-crystal–solid interface", Phys. Rev. A **46**, R6174–R6177 (1992).

[38]J. P. F. Lagerwall, *Three facets of modern liquid crystal science*, 2010.

[39]J. L. Ericksen, "Inequalities in liquid crystal theory", The Physics of Fluids **9**, 1205–1207 (1966).

[40]J. L. Ericksen, "Anisotropic fluids", Arch. Rat. Mech. Anal. **4**, 231 (1959).

[41]F. M. Leslie, "Some constitutive equations for liquid crystals", Arch. Rat. Mech. Anal. **28**, 265–283 (1968).

[42]F. M. Leslie, "Some constitutive equations for anisotropic fluids", Quart. Jour. Mech. and App. Math. **19**, 357–370 (1966).

[43]O. Parodi, "Stress tensor for a nematic liquid crystal", J. Phys. France **31**, 581–584 (1970).

[44]A. N. Beris and B. J. Edwards, *Thermodynamics of flowing systems: with internal microstructure* (Oxford University Press, 1994).

[45]B. J. Edwards, A. N. Beris, and M. Grmela, "Generalized constitutive equation for polymeric liquid crystals part 1. model formulation using the hamiltonian (poisson bracket) formulation", Jour. Non-Newt. Fluid Mech. **35**, 51–72 (1990).

[46]G. Duclos, C. Blanch-Mercader, V. Yashunsky, G. Salbreux, J. F. Joanny, J. Prost, and P. Silberzan, "Spontaneous shear flow in confined cellular nematics", Nat. Phys. **14**, 728–732 (2018).

[47]D. Marenduzzo, E. Orlandini, M. E. Cates, and J. M. Yeomans, "Steady-state hydrodynamic instabilities of active liquid crystals: hybrid lattice boltzmann simulations", Phys. Rev. E **76**, 031921 (2007).

[48]J. Hardoüin, R. Hughes, A. Doostmohammadi, J. Laurent, T. Lopez-Leon, J. M. Yeomans, J. Ignés-Mullol, and F. Sagués, "Reconfigurable flows and defect landscape of confined active nematics", Comm. Phys. **2**, 121 (2019).

[49]E. J. Hemingway, P. Mishra, M. C. Marchetti, and S. M. Fielding, "Correlation lengths in hydrodynamic models of active nematics", Soft Matter **12**, 7943 (2016).

[50]S. Ramaswamy and M. Rao, "Active-filament hydrodynamics: instabilities, boundary conditions and rheology", New Jour. Phys. **9**, 423–423 (2007).

[51]L. Giomi, M. J. Bowick, P. Mishra, R. Sknepnek, and M. Cristina Marchetti, "Defect dynamics in active nematics", Philos. Trans. A: Math. Phys. Eng. Sci. **372**, 20130365 (2014).

[52]H. H. Wensink, J. Dunkel, S. Heidenreich, K. Drescher, R. E. Goldstein, H. Löwen, and J. M. Yeomans, "Meso-scale turbulence in living fluids", PNAS **109**, 14308–14313 (2012).

[53]S. P. Thampi, R. Golestanian, and J. M. Yeomans, "Velocity correlations in an active nematic", Phys. Rev. Lett. **111**, 118101 (2013).

[54]S. P. Thampi, A. Doostmohammadi, R. Golestanian, and J. M. Yeomans, "Intrinsic free energy in active nematics", EPL (Europhysics Letters) **112**, 28004 (2015).

[55]M. L. Blow, S. P. Thampi, and J. M. Yeomans, "Biphasic, lyotropic, active nematics", Phys. Rev. Lett. **113**, 248303 (2014).

[56]A. Doostmohammadi, M. F. Adamer, S. P. Thampi, and J. M. Yeomans, "Stabilization of active matter by flow-vortex lattices and defect ordering", Nat. Comm. **7** (2016).

[57]H. Wioland, F. G. Woodhouse, J. Dunkel, J. O. Kessler, and R. E. Goldstein, "Confinement stabilizes a bacterial suspension into a spiral vortex", Phys. Rev. Lett. **110**, 268102 (2013).

[58]E. Lushi, H. Wioland, and R. E. Goldstein, "Fluid flows created by swimming bacteria drive self-organization in confined suspensions", PNAS **111**, 9733 (2014).

[59]H. Wioland, F. G. Woodhouse, J. Dunkel, and R. E. Goldstein, "Ferromagnetic and antiferromagnetic order in bacterial vortex lattices", Nat. Phys. **12**, 341–345 (2016).

[60]H. Wioland, E. Lushi, and R. E. Goldstein, "Directed collective motion of bacteria under channel confinement", New J. Phys. **18**, 075002 (2016).

[61]M. Deforet, V. Hakim, H. Yevick, G. Duclos, and P. Silberzan, "Emergence of collective modes and tri-dimensional structures from epithelial confinement", Nat. Comm. **5**, 3747 (2014).

[62]W. Xi, S. Sonam, T. Beng Saw, B. Ladoux, and C. Teck Lim, "Emergent patterns of collective cell migration under tubular confinement", Nat. Comm. **8**, 1517 (2017).

[63]G. Duclos, S. Garcia, H. G. Yevick, and P. Silberzan, "Perfect nematic order in confined monolayers of spindle-shaped cells", Soft Matter **10**, 2346–2353 (2014).

[64]P. Guillamat, J. Ignés-Mullol, and F. Sagués, "Taming active turbulence with patterned soft interfaces", Nat. Comm. **8** (2017).

[65]P. Guillamat, J. Ignés-Mullol, and F. Sagués, "Control of active nematics with passive liquid crystals", Mol. Crys. Liq. Crys. **646**, 226–234 (2017).

[66]A. Opathalage, M. M. Norton, M. P. Juniper, B. Langeslay, S. A. Aghvami, S. Fraden, and Z. Dogic, "Self-organized dynamics and the transition to turbulence of confined active nematics", Proc. Nat. Aca. Sci. **116**, 4788–4797 (2019).

[67]K. Suzuki, M. Miyazaki, J. Takagi, T. Itabashi, and S. Ishiwata, "Spatial confinement of active microtubule networks induces large-scale rotational cytoplasmic flow", PNAS **114**, 2922–2927 (2017).

[68]P. Guillamat, Ž. Kos, J. Hardoüin, J. Ignés-Mullol, M. Ravnik, and F. Sagués, "Active nematic emulsions", Sci. Adv. **4**, eaao1470 (2018).

[69]P. W. Ellis, D. J. G. Pearce, Y.-W. Chang, G. Goldsztein, L. Giomi, and A. Fernández-Nieves, "Curvature-induced defect unbinding and dynamics in active nematic toroids", Nat. Phys. **14**, 85–90 (2018).

[70]K. T. Wu, J. B. Hishamunda, D. T. N. Chen, S. J. DeCamp, Y. W. Chang, A. Fernández-Nieves, S. Fraden, and Z. Dogic, "Transition from turbulent to coherent flows in confined three-dimensional active fluids", Science **355**, 6331 (2017).

[71]G. Melaugh, J. Hutchison, K. N. Kragh, Y. Irie, A. Roberts, T. Bjarnsholt, S. P. Diggle, V. D. Gordon, and R. J. A., "Shaping the growth behaviour of biofilms initiated from bacterial aggregates", PloS one **11**, e0149683 (2016).

[72]D. P. Lloyd and R. J. Allen, "Competition for space during bacterial colonization of a surface", Jour. Roy. Soc. Int. **12**, 20150608 (2015).

[73]P. Guillamat, J. Ignés-Mullol, S. Shankar, M. C. Marchetti, and F. Sagués, "Probing the shear viscosity of an active nematic film", Phys. Rev. E **94**, 060602 (2016).

[74]B. Loring, H. Karimabadi, and V. Rortershteyn, *A screen space gpgpu surface lic algorithm for distributed memory data parallel sort last rendering infrastructures*, tech. rep. (Lawrence Berkeley National Lab.(LBNL), Berkeley, CA (United States), 2014).

[75]L. Giomi, "Geometry and topology of turbulence in active nematics", Phys. Rev. X **5**, 031003 (2015).

[76]H. Chaté, F. Ginelli, and R. Montagne, "Simple model for active nematics: quasi-long-range order and giant fluctuations", Phys. Rev. Lett. **96**, 180602 (2006).

[77]F. Ginelli, F. Peruani, m. Bär, and H. Chaté, "Large-scale collective properties of self-propelled rods", Phys. Rev. Lett. **104**, 184502 (2010).

[78]R. Voituriez, J. F. Joanny, and J. Prost, "Spontaneous flow transition in active polar gels", Europhys. Lett. **70**, 404–410 (2005).

[79]L. M. Pismen, "Dynamics of defects in an active nematic layer", Phys. Rev. E **88**, 050502 (2013).

[80]L. Giomi and A. DeSimone, "Spontaneous division and motility in active nematic droplets", Phys. Rev. Lett. **112**, 147802 (2014).

[81]C. Denniston, "Disclination dynamics in nematic liquid crystals", Phys. Rev. B **54**, 6272 (1996).

[82]M. M. Norton, A. Baskaran, A. Opathalage, B. Langeslay, S. Fraden, A. Baskaran, and M. F. Hagan, "Insensitivity of active nematic liquid crystal dynamics to topological constraints", Phys. Rev. E **97**, 012702 (2018).

[83]T. Gao and Z. Li, "Self-driven droplet powered by active nematics", Phys. Rev. Lett. **119**, 108002 (2017).

[84]S. J. DeCamp, G. S. Redner, A. Baskaran, M. F. Hagan, and Z. Dogic, "Orientational order of motile defects in active nematics", Nat. Matter. **14**, 1110–1115 (2015).

[85]A. J. Vromans and L. Giomi, "Orientational properties of nematic disclinations", Soft Matter **12**, 6490–6495 (2016).

[86]P. Srivastava, P. Mishra, and M. C. Marchetti, "Negative stiffness and modulated states in active nematics", Soft Matter **12**, 8214–8225 (2016).

[87]R. Hughes and J. M. Yeomans, "Collective chemotaxis of active nematic droplets", Phys. Rev. E **102**, 020601 (2020).

[88]R. Mayor and S. Etienne-Manneville, "The front and rear of collective cell migration", Nat. Rev. Mol. Cell Bio. **17**, 97 (2016).

[89]A. Shellard and R. Mayor, "Supracellular migration – beyond collective cell migration", Jour. of Cell Sci. **132** (2019).

[90]A. Gopinathan and N. S. Gov, "Cell cluster migration: connecting experiments with physical models", Sem. in Cell and Dev. Bio. **93**, 77–86 (2019).

[91]E. Camand, F. Peglion, N. Osmani, M. Sanson, and S. Etienne-Manneville, "N-cadherin expression level modulates integrin-mediated polarity and strongly impacts on the speed and directionality of glial cell migration", Jour. of Cell Sci. **125**, 844–857 (2012).

[92]P. Friedl, J. Locker, E. Sahai, and J. E. Segall, "Classifying collective cancer cell invasion", Nat. Cell Bio. **14**, 777 (2012).

[93]P. Van Liedekerke, M. M. Palm, N. Jagiella, and D. Drasdo, "Simulating tissue mechanics with agent-based models: concepts, perspectives and some novel results", Comp. Par. Mech. **2**, 401–444 (2015).

[94]B. A. Camley, J. Zimmermann, H. Levine, and W. J. Rappel, "Collective signal processing in cluster chemotaxis: roles of adaptation, amplification, and co-attraction in collective guidance", PLoS Comput. Biol. **12**, e1005008 (2016).

[95]B. A. Camley and W. J. Rappel, "Physical models of collective cell motility: from cell to tissue", Journal of Phys. D: App. Phys. **50**, 113002 (2017).

[96]J. Prost, F. Jülicher, and J.-F. Joanny, "Active gel physics", Nat. Phys. **11**, 111–117 (2015).

[97]J. W. Cahn and J. E. Hilliard, "Free energy of a nonuniform system. i. interfacial free energy", J. Chem. Phys. **28**, 258–267 (1958).

[98]J. Shen, X. Yang, and Q. Wang, "Mass and volume conservation in phase field models for binary fluids", Comm. Comp. Phys. **13**, 1045–1065 (2013).

[99]S. P. Thampi, R. Golestanian, and J. M. Yeomans, "Vorticity, defects and correlations in active turbulence", Phil. Trans. Series A, Math., Phys., and Eng. Sci. **372**, 20130366 (2014).

[100]O. Ilina and P. Friedl, "Mechanisms of collective cell migration at a glance", Jour. of Cell Sci. **122**, 3203–3208 (2009).

[101]F. Huber, J. Schnauß, S. Rönicke, P. Rauch, K. Müller, C. Fütterer, and J. Käs, "Emergent complexity of the cytoskeleton: from single filaments to tissue", eng, Adv. phys. **62**, 1–112 (2013).

[102]J. E. Bear and F. B. Gertler, "Ena/vasp: towards resolving a pointed controversy at the barbed end", Jour. of Cell Sci. **122**, 1947–1953 (2009).

[103]A. Wegner, "Head to tail polymerization of actin", Jour. of Molec. Bio. **108**, 139–150 (1976).

[104]R. Mayor and C. Carmona-Fontaine, "Keeping in touch with contact inhibition of locomotion", Tren. in Cell Bio. **20**, 319–328 (2010).

[105]X. Trepat, R. Wasserman M, T. E. Angelini, E. Millet, D. A. Weitz, J. P. Butler, and J. J. Fredberg, "Physical forces during collective cell migration", Nat. Phys. **5**, 426 (2009).

[106]M. Abercrombie and J. E. Heaysman, "Observations on the social behaviour of cells in tissue culture: i. speed of movement of chick heart fibroblasts in relation to their mutual contacts", Exp. Cell Res. **5**, 111–131 (1953).

[107]M. Poujade, E. Grasland-Mongrain, A. Hertzog, J. Jouanneau, P. Chavrier, B. Ladoux, A. Buguin, and P. Silberzan, "Collective migration of an epithelial monolayer in response to a model wound", Proc. Nat. Aca. Sci. **104**, 15988–15993 (2007).

[108]R. Farooqui and G. Fenteany, "Multiple rows of cells behind an epithelial wound edge extend cryptic lamellipodia to collectively drive cell-sheet movement", Jour. of Cell Sci. **118**, 51–63 (2005).

[109]A. Vasilyev, Y. Liu, S. Mudumana, S. Mangos, P. Lam, A. Majumdar, J. Zhao, K.-L. P., I. Kondrychyn, V. Korzh, and I. A. Drummond, "Collective cell migration drives morphogenesis of the kidney nephron", PLOS Biology **7**, 1–14 (2009).

[110]E. Anon, X. Serra-Picamal, P. Hersen, N. C. Gauthier, M. P. Sheetz, X. Trepat, and B. Ladoux, "Cell crawling mediates collective cell migration to close undamaged epithelial gaps", Proc. Nat. Aca. Sci. **109**, 10891–10896 (2012).

[111]B. Palmieri, Y. Bresler, D. Wirtz, and M. Grant, "Multiple scale model for cell migration in monolayers: elastic mismatch between cells enhances motility", Sci. Rep. **5**, 11745 (2015).

[112]B. Loewe, M. Chiang, D. Marenduzzo, and M. C. Marchetti, "Solid-liquid transition of deformable and overlapping active particles", Phys. Rev. Lett. **125**, 038003 (2020).

[113]J. Löber, F. Ziebert, and I. S. Aranson, "Modeling crawling cell movement on soft engineered substrates", Soft Matter **10**, 1365–1373 (2014).

[114]F. Ziebert, S. Swaminathan, and I. S. Aranson, "Model for self-polarization and motility of keratocyte fragments", Jour. Roy. Soc. Int. **9**, 1084–1092 (2011).

[115]F. Ziebert and I. S. Aranson, "Effects of adhesion dynamics and substrate compliance on the shape and motility of crawling cells", PLoS one **8**, e64511 (2013).

[116]S. Najem and M. Grant, "Phase-field model for collective cell migration", Phys. Rev. E **93**, 052405 (2016).

[117]M. Basan, J. Elgeti, E. Hannezo, W. J. Rappel, and H. Levine, "Alignment of cellular motility forces with tissue flow as a mechanism for efficient wound healing", Proc. Nat. Aca. Sci. **110**, 2452–2459 (2013).

[118]B. Palmieri, Y. Bresler, D. Wirtz, and M. Grant, "Multiple scale model for cell migration in monolayers: elastic mismatch between cells enhances motility", Sci. Rep. **5**, 11745 (2015).

[119]N. Sepúlveda, L. Petitjean, O. Cochet, E. Grasland-Mongrain, P. Silberzan, and V. Hakim, "Collective cell motion in an epithelial sheet can be quantitatively described by a stochastic interacting particle model", PLoS Comp. Bio. **9**, e1002944 (2013).

[120]G. Peyret, R. Mueller, J. d'Alessandro, S. Begnaud, P. Marcq, R. Mège, J. M. Yeomans, A. Doostmohammadi, and B. Ladoux, "Sustained oscillations of epithelial cell sheets", Biophys. Jour. **117**, 464–478 (2019).

[121]T. Krüger, H. Kusumaatmaja, A. Kuzmin, O. Shardt, G. Silva, and E. M. Viggen, *The lattice boltzmann method* (Springer, Cham, 2016).

[122]T. Sanchez, D. T. N. Chen, S. J. DeCamp, M. Heymann, and Z. Dogic, "Spontaneous motion in hierarchically assembled active matter", Nature **491**, 431–434 (2012).

[123]S. Ramaswamy, R. A. Simha, and J. Toner, "Active nematics on a substrate: giant number fluctuations and long-time tails", Europhys. Lett. **62**, 196 (2003).